

SLAC - 339
UC - 28
(A)

**RF PROPERTIES OF PERIODIC ACCELERATING
STRUCTURES FOR LINEAR COLLIDERS***

J. W. WANG

Stanford Linear Accelerator Center

Stanford University

Stanford, California, 94309

July 1989

Prepared for the Department of Energy
under contract number DE-AC03-76SF00515

Printed in the United States of America. Available from the National
Technical Information Service, U.S. Department of Commerce, 5285
Port Royal Road, Springfield, Virginia 22161. Price: Printed Copy
A08, Microfiche A01.

*Ph.D. Dissertation

ABSTRACT

RF PROPERTIES OF PERIODIC ACCELERATING STRUCTURES FOR LINEAR COLLIDERS

J. W. Wang

Stanford University, 1989

With the advent of the SLAC electron-positron linear collider (SLC) in the 100 GeV center-of-mass energy range, research and development work on even higher energy machines of this type has started in several laboratories in the United States, Europe, the Soviet Union and Japan. These linear colliders appear to provide the only promising approach to studying e^+e^- physics at center-of-mass energies approaching 1 TeV.

This thesis concerns itself with the study of radio frequency properties of periodic accelerating structures for linear colliders and their interaction with bunched beams. The topics that have been investigated are:

- Experimental measurements of the energy loss of single bunches to longitudinal modes in two types of structures, using an equivalent signal on a coaxial wire to simulate the beam.
- A method of cancelling the energy spread created within a single bunch by longitudinal wakefields, through appropriate shaping of the longitudinal charge distribution of the bunch.
- Derivation of the complete transient beam-loading equation for a train of bunches passing through a constant-gradient accelerator section, with application to the calculation and minimization of multi-bunch energy spread.
- Detailed study of field emission and radio frequency breakdown in disk-loaded structures at S-, C- and X-band frequencies under extremely high-gradient conditions, with special attention to thermal effects, radiation, sparking, emission of gases, surface damage through explosive emission and its possible control through RF-gas processing.

ACKNOWLEDGEMENTS

My heartfelt gratitude must first go to my advisor, Professor G. A. Loew, for taking me as his student, for his countless hours of help and advice, and for his continuous encouragement and guidance throughout my years at SLAC. I have been very fortunate to have had the opportunity to benefit from his extensive knowledge and broad experience in the field of accelerator physics, and to be stimulated by his great enthusiasm for science.

I extend my warm thanks to Professor R. H. Miller who can provide surprisingly lucid explanations to complex problems, and who was on my reading committee; to Professor P. B. Wilson who always stops his work to answer my questions; to my Professor in China, Naichuan Liu, who first encouraged me to study accelerator physics.

Over the past several years during our RF breakdown studies at SLAC, I have been assisted by many people in various phases of the work. J. Zamzow helped with all the high-power waveguide installations, the vacuum system, and the gas exposure tests. H. Deruyter gave his assistance in many of the RF cold tests. P. Corredoura set up the VAX-785 computer interface system to digitize and record the breakdown pulses. H. Hoag led the mechanical design and construction of the recent 11.42 GHz traveling-wave section. E. Hoyt helped with many useful discussions regarding surface damage, gas exposures, and provided the scanning electron microscope pictures. V. Nguyen-Tuong, while visiting SLAC, was the prime mover in the early tests involving argon processing. R. Ecken and G. Aske were helpful in improving the operation of the test stand and C. Griffin managed to "squeeze" 47 MW out of an old 36 MW XK-5 klystron. R. McCall, T. Jenkins, R. Nelson, D. Busick, S. Carlson, D. Walz and N. Ipe helped with the radiation and beam energy calculations and measurements, and Professor K. L. Brown with beam transport calculations. I appreciate very useful overall discussions with E. Garwin, R. Kirby, A. Schwettman and J. Halbritter.

I benefited from collaborating with E. Tanabe of Varian Associates Inc. in the planning and testing of the C- and X-band half-cavities performed at Varian. Also at Varian, valuable assistance was given by L. Nelson and F. Gordon.

A special acknowledgement is due Dr. Renzo Parodi from the I.N.F.N., Genova, Italy, who took a personal interest in calculating and plotting field-emitted electron trajectories with his NEWTRAJ computer program, of which one example appears in this thesis.

Excellent support was received from the SLAC shops, in particular from D. Fuller, J. Pope, D. Wright, C. Rago, R. Pickup, W. Jacopi, O. Millican and D. Sartain.

I wish to thank J. N. Weaver, J. Styles and D. F. Wang who were extremely helpful in the energy loss measurements.

Finally, I would like to thank my reading committee member, Professor M. Chodorow, and oral examination committee member, Professor H. Wiedemann, for their helpful comments.

I am indebted to all the above individuals as well as to B.-J. Ferandin, K. Johnston and the SLAC Publications Department for preparing this dissertation.

Last, but not least, I wish to thank my family: my brother and sister-in-law for their loving support of my education in China, and to my wife for her patience and understanding.

TABLE OF CONTENTS

	Page
ABSTRACT	ii
ACKNOWLEDGEMENTS	iii
TABLE OF CONTENTS	v
LIST OF TABLES	viii
LIST OF FIGURES	ix
LIST OF SYMBOLS	xiii
1. INTRODUCTION	1
1.1 Very High Energy Colliders	1
1.2 Linac Related RF Properties	3
1.3 Interaction Between the Beam and Accelerating Structure	9
1.4 High Accelerating Gradient and Related Problems	10
2. ENERGY LOST TO LONGITUDINAL MODES BY SINGLE ELECTRON BUNCHES TRAVERSING PERIODIC STRUCTURES	12
2.1 Motivation	12
2.2 Loss Parameter	12
2.3 Calculation and Measurement of the Loss Parameter	15
2.4 Measurement Set-up	19
2.5 Measurements and Results	21
2.6 Conclusions	27

3.	MINIMIZING THE ENERGY SPREAD WITHIN A SINGLE BUNCH BY SHAPING ITS CHARGE DISTRIBUTION	28
3.1	Motivation	28
3.2	Optimizing the Bunch Shape	28
3.3	Discussion	36
3.4	Tolerances	38
3.5	Conclusions	39
4.	THE TRANSIENT BEAM LOADING PROBLEM IN CONSTANT-GRADIENT LINEAR ACCELERATORS	40
4.1	General Solution of the Transient Beam Loading Problem for the Constant-Gradient Structure	40
4.2	Beam Injection Exactly After One Filling Time	45
4.3	Early Beam Injection for Multibunch Operation	46
4.4	Solutions in Terms of Multibunch Parameters	50
5.	RF BREAKDOWN STUDIES IN ROOM TEMPERATURE ELECTRON LINAC STRUCTURES	52
5.1	Motivation	52
5.2	Accelerating Structures Tested and Maximum Gradients Reached	53
5.3	Structure Design, Experimental Set-ups, and Tests Performed	61
5.3.1	S-band Disk-loaded Waveguide Structure	61
5.3.2	S-band π -mode Accelerator Structure	81
5.3.3	C-band and X-band Standing-Wave Structure	86

5.3.4	11.424 GHz High Gradient Accelerator	90
5.3.5	Chemical Cleaning and Baking	90
5.4	Field Emission and Fowler-Nordheim Plots	93
5.4.1	DC Field Electron Emission From Ideal Metal Surface	93
5.4.2	Enhanced Field Emission (EFE)	96
5.4.3	Enhanced Field Emission Models	97
5.4.4	Field Electron Emission for Alternating Field	104
5.5	Vacuum Breakdown Phenomena and Some Breakdown Models	106
5.5.1	The Kilpatrick Criterion and Its Derivation	106
5.5.2	Some Vacuum Breakdown Models	110
5.6	Observations of Field Emission, RF Processing and RF Breakdown	115
5.7	Confrontation of Results with Existing Models	126
5.8	Remaining Problems and Conclusions	130

LIST OF TABLES

		Page
Table 2.1	Results of measurements for disk-loaded structures.	24
Table 2.2	Results of measurements for alternating-spoke structure.	26
Table 3.1	Calculated energy spectra (all cases for 5×10^{10} particles).	36
Table 3.2	Truncated gaussian bunch ($\theta_{total} = 15^\circ$, $\sigma = 9^\circ$, $5 \times 10^{10} e$).	38
Table 3.2	Truncated gaussian bunch ($\theta_{total} = 15^\circ$, $\sigma = 9^\circ$, $\theta_0 = 15.5^\circ$).	39
Table 5.1	Fields calculated for normalizing condition $ \int_0^L E_z(z) \exp\{j(\omega z/c)\} dz /L = 1 \text{ MV/m}$.	58
Table 5.2	Experimentally obtained breakdown-limited gradients.	59
Table 5.3	Predicted limiting gradient for future colliders at specific frequencies.	61
Table 5.4	Procedure for chemical cleaning.	93

LIST OF FIGURES

		Page
Fig. 2.1	Comparison of charged particle bunch traversing an empty structure and current pulse propagating along a center conductor in the structure.	16
Fig. 2.2	Measurement layout.	20
Fig. 2.3	Accelerating structures tested: a) Disk-loaded structure, b) Alternating-spoke structure.	22
Fig. 2.4	Successive current pulses recorded by X-Y plotter.	23
Fig. 2.5	Total loss parameter per period, as a function of σ_z , as obtained from computer calculation, SLAC linac beam loading measurements and bench tests normalized to 2856 MHz.	25
Fig. 3.1	Longitudinal wake function per cell as a function of phase angle for SLAC constant-gradient structure.	30
Fig. 3.2	Definitions of phase angles showing position of bunch with respect to accelerating wave. The charge distribution is $f(\theta')$ and the maximum energy gain is V_0 .	32
Fig. 3.3	Bunch shape, <i>i.e.</i> , particle distribution as a function of phase angle which leads to negligible spectrum width, for various values of θ_0 . The point marked "T" indicates where the integrated charge in the bunch reaches $5 \times 10^{10} e$.	34
Fig. 3.4	Particle energy along bunches of Fig. 3.3 as a function of phase angle.	35
Fig. 3.5	Energy spectra for the examples of Table 3.1 with $5 \times 10^{10} e$ (left-hand scale) and for the Gaussian bunch with $5 \times 10^8 e$ (right-hand scale).	37
Fig. 4.1.	Transient beam loading shown schematically in arbitrary units for injection before $t = t_F$ and at $t = t_F$.	47
Fig. 5.1	Collection of S-band (seven-cavity, $2\pi/3$ -mode), C-band and X-band cavities used in tests.	54
Fig. 5.2	S-band (seven-cavity, $2\pi/3$ -mode) structure, complete with water cooling system.	55

		Page
Fig. 5.3	S-band (two-cavity, π -mode) structure, complete with water cooling system.	57
Fig. 5.4	Peak breakdown surface fields measured as a function of frequency.	60
Fig. 5.5	Traveling waves and standing waves in the SLAC structure with their respective field amplitudes in arbitrary units. Note that E_z is taken on-axis and E_r and H_ϕ are off-axis.	64
Fig. 5.6	Experimental set-up used for S-band (seven-cavity, $2\pi/3$ -mode) structure.	67
Fig. 5.7	Cross-section of coupler cavity showing extra brazed-in matching iris to obtain critical coupling.	68
Fig. 5.8	The microwave measurement set-ups for matching, tuning and bead-pulling.	70
Fig. 5.9	Power reflected by bead as a function of axial position (in arbitrary units). This power, if it were measured with a perfect square-law crystal, would be proportional to $ E_z ^4$ because the reflection coefficient of the bead is proportional to $ E_z ^2$ and the reflected power scales as the square of the reflection coefficient.	71
Fig. 5.10	Block diagram of RF system for S-band test.	73
Fig. 5.11	Overall view of experimental set-up for S-band test.	74
Fig. 5.12	Temperatures for the test points shown in Fig. 5.6, and resonant frequency, both as a function of average power dissipated in accelerator section.	76
Fig. 5.13	Field emitted current transmitted through downstream window (right-hand side in Fig. 6) to Faraday cup, as a function of peak input power.	78
Fig. 5.14	(a) Layout of window, spectrometer magnet and slit; (b), (c) and (d) electron trajectories (continuous lines) and γ -rays (dotted lines) for various initial electron energies and magnetic fields.	79

		Page
Fig. 5.15	Uncorrected (dashed lines) and corrected (continuous lines) electron energy spectra for various values of peak input power into S-band seven-cavity structure.	80
Fig. 5.16	Field emitted electron trajectories plotted for S-band ($2\pi/3$) structure by means of computer program NEWTRAJ [courtesy of R. Parodi (Ref. 33)].	82
Fig. 5.17	Average x-ray dosage distribution around S-band (seven-cavity, $2\pi/3$ -mode) accelerator section (300 MV/m surface field, 2.5 μ sec, 120 pps).	83
Fig. 5.18	Exploded view of continuous array of klystron beamlets and π -mode accelerator cavities directly connected to them. [from Loew (Ref. 28)].	84
Fig. 5.19	Cutaway view of S-band π -mode section.	85
Fig. 5.20	Experimental set-up used for S-band (two-cavity, π -mode) structure, showing details of vacuum system.	87
Fig. 5.21	C-band tester for high-gradient experiments.	89
Fig. 5.22	Experimental set-up used for X-band cavity.	91
Fig. 5.23	11.424 High gradient accelerator and set-up for microwave measurements.	92
Fig. 5.24	Potential energy diagram showing the modified electric field potential barrier.	94
Fig. 5.25	Field enhancement factor β associated with various idealized microprotrusion geometries [from Rohrbach (Ref. 40)].	99
Fig. 5.26	A schematic representation of the emission regime showing the conducting channels in the insulating inclusion and the associated microscopic field enhancement [From Latham (Ref. 46)].	100
Fig. 5.27	A band-diagram of a "on" state of an electron and photon emitting composite microregime [from Latham (Ref. 37)].	101
Fig. 5.28	W plotted against E , the cathode gradient. For DC, W corresponds to the applied voltage; for RF, W is a function of frequency and gap [from Kilpatrick (Ref. 7)].	107

		Page
Fig. 5.29	Graph for ion transit-time correction. For plane parallel fields, $V^* = (g/\lambda)^2 M_0 c^2 / \pi q$. For computing the maximum cathode ion energy, where $\nabla \cdot E$ is not ≈ 0 , the calculation of W or V^* is without reference [from Kilpatrick (Ref. 7)].	108
Fig. 5.30	An idealized field-emitting microprotrusion.	112
Fig. 5.31	Development of surface erosion in the case of breakdown initiated by Explosive Electron Emission.	114
Fig. 5.32	Residual gas analyzer displays during RF processing of S-band, two-cavity structure, a) before breakdown, and b) immediately after breakdown.	117
Fig. 5.33	Forward and reflected RF wave shapes: a) normal, b) during breakdown.	118
Fig. 5.34	Breakdown "event" recorded at four radial probes in full-field cavity (A), two radial probes in half-field cavity (B), and one upstream probe. The forward RF pulse provides a time reference.	119
Fig. 5.35	Typical RF processing schedule for S-band, seven-cavity structure.	121
Fig. 5.36	Fowler-Nordheim plots for S-band and C-band structures.	123
Fig. 5.37	Scanning electron microscope pictures of S-band cavity nose cone showing RF breakdown damage (note four successive degrees of magnification).	124
Fig. 5.38	RF Fowler-Nordheim plots for S-band (seven-cavity, $2\pi/3$ -mode) structure as a function of time. Curve (4) was recorded shortly after argon scrubbing and pumpdown.	125

LIST OF SYMBOLS

The symbols are listed in order of first use and the corresponding section number is given in parentheses.

Chapter 1

E_a	Average accelerating field on axis (1.2)
E_p	Peak field on surface of accelerating structure (1.2)
w	Energy stored per unit length (1.2)
ω	Angular frequency of RF generator (1.2)
r	Shunt impedance per unit length (1.2)
Q	Factor of merit of an RF cavity (1.2)
v_g	Group velocity (1.2)
t_F	Filling time (1.2)
ℓ	Length of an accelerator section (1.2)
P	RF power (1.2)
P_{in}	RF power into a section (1.2)
P_{out}	RF power out of a section (1.2)
τ	Attenuation factor of a section (1.2)
α	Attenuation constant (1.2)
Q_L	Loaded Q (1.2)
Q_0	Unloaded Q (1.2)
β	Coupling coefficient of a section to network (1.2)
P_{dis}	Power dissipated in a section (1.2)
s	Elastance per unit length (1.2)
k_0	Energy loss parameter for fundamental mode (1.2)
V	Energy gain of a charged particle (1.2)
W	Energy stored in entire section (1.2)
η	Structure efficiency (1.2)
P_{norm}	Normalized peak power (1.2)
t_P	Length of RF pulse (1.2)

Chapter 2

V_n	Beam-induced voltage for n^{th} mode (2.2)
V_{ne}	Effective voltage seen by a point charge (2.2)
k_n	Energy loss parameter of a cavity for n^{th} mode (2.2)
W_n	Energy left behind by a particle (2.2)
ΔU	Energy loss of a particle (2.2)
P_n	Power dissipated in a cavity (2.2)
R_n	Shunt impedance of a cavity for n^{th} mode (2.2)
ω_n	Angular frequency of n^{th} mode (2.2)
Q_n	Factor of merit of a cavity for n^{th} mode (2.2)
τ	Time following a point charge (2.2)
$I(t)$	Current distribution of a bunch (2.2)
$V_b(t)$	Beam-induced potential within a bunch (2.2)
ΔU_{tot}	Total energy loss of a bunch (2.2)
K_{tot}	Total energy loss parameter of a cavity (2.2)
B	Beam loading enhancement factor (2.2)
σ	Standard deviation of a Gaussian bunch (2.3)
R	Characteristic resistance of a transmission line (2.3)
$i_0(t)$	Original current pulse (2.3)
$i_m(t)$	Modified current pulse after a discontinuity (2.3)
$i_f(t)$	Induced forward current pulse due to a discontinuity (2.3)
$i_r(t)$	Induced backward current pulse due to a discontinuity (2.3)
U_1, U_2	Total energy contained in pulses (2.3)
t_r	Rise time (2.3)
σ'_m	Measured standard deviation of a pulse (2.3)

Chapter 3

θ_1	Phase angle with respect to RF crest (3.2)
V_-	Energy gain (3.2)

L	Length of entire accelerator (3.2)
E_0	Accelerating gradient for particles at RF crest (3.2)
$w(\tau)$	Longitudinal wake function per cell (3.2)
W_L	Longitudinal wake function for entire accelerator (3.2)
θ_0	Phase angle of bunch head (3.2)
$f(\theta)$	Charge distribution of a bunch (3.2)
E_{max}	Maximum energy (3.2)
E_{min}	Minimum energy (3.2)
\bar{E}	Average energy (3.2)
σ_E	Fractional standard deviation (3.2)
d	Length of a single cavity (3.2)

Chapter 4

E	Electric field on axis (4.1)
i	Beam current (4.1)
t_z	Time needed for propagation of RF power from 0 to z (4.1)
E_0	Amplitude of electric field at $z = 0$ (4.1)
t_i	Time when beam is injected (4.1)
N	Number of equally spaced bunches in a bunch train (4.1)
t_b	Time span of a bunch train (4.1)
i_0	Average current within a bunch train (4.1)
ΔV_b	Transient beam loading (4.2)
k	Energy loss parameter per unit length for fundamental mode (4.2)
V_0	Energy of first bunch (4.3)
δV	Energy deviation from V_0 (4.3)
t_{max}	Time difference of head bunch and bunch having maximum energy sag (4.3)
δV_{max}	Maximum energy sag within a bunch train (4.3)
ΔS	Distance between equally spaced bunches (4.4)

Chapter 5

r_{sw}	SW shunt impedance per unit length (5.2)
r_{TW}	TW shunt impedance per unit length (5.2)
E_s	Peak surface electric field (5.2)
f	RF frequency (5.2)
a	Beam hole radius (5.2)
P_D	Power dissipated (5.2)
\bar{E}_{acc}	Average accelerating field (5.2)
$ E_{z,SW} _{max}$	Maximum axial SW electric field (5.2)
$ E_{s,SW} _{max}$	Maximum surface SW electric field (5.2)
$E_{z,TW}$	Axial TW electric field (5.2)
β_0	Propagation constant of fundamental space harmonic (5.3.1)
β_n	Propagation constant of n_{th} space harmonic (5.3.1)
a_n	Amplitude of n^{th} space harmonic (5.3.1)
$E_{z,SW}$	Axial SW electric field (5.3.1)
$ E_{s,TW} _{max}$	Maximum surface TW electric field (5.3.1)
T	RF time period (5.3.1)
Γ	Standing wave ratio (5.3.1)
ρ	Reflection coefficient (5.3.1)
\bar{P}_{for}	Average forward power for a critically coupled cavity (5.3.1)
\bar{P}_{ref}	Average reflected power for a critically coupled cavity (5.3.1)
T_P	Length of an RF pulse (5.3.1)
T_C	Cavity time constant (5.3.1)
$V(x)$	Potential energy of a one-dimensional potential barrier (5.4.1)
W_a	Potential energy of an electron inside metal (5.4.1)
P_x, P_y, P_z	Momenta of an electron (5.4.1)
h	Planck's constant (5.4.1)
k	Boltzmann's constant (5.4.1)
ζ	Fermi energy (5.4.1)

W_x	Electron energy (5.4.1)
$N(W_x)$	Electron Supply function (5.4.1)
$D(W_x)$	Electron transmission coefficient (5.4.1)
j_F	Field emission current density (5.4.1)
ϕ	Work function (5.4.1)
β	Field enhancement factor (5.4.2)
E_m	Maximum microscopic electric field on surface (5.4.2)
A_e	Effective emitting area (5.4.2)
I_F	Field emission current (5.4.2)
E_0	Amplitude of macroscopic electric field (5.4.4)
\bar{I}_f	Average field emission current in RF field (5.4.4)
m_0	Mass of atomic hydrogen (5.5.1)
g	Gap width of parallel plate electrodes (5.5.1)
$\rho(T)$	Electrical resistivity (5.5.2)
K	Thermal conductivity (5.5.2)
T_r, T_b	Temperature at top and base of an emitter (5.5.2)
β_1	Geometric enhancement factor (5.7)
β_2	Dielectric enhancement factor (5.7)
β_{eff}	Effective enhancement factor (5.7)
Δd	Width of dielectric layer (5.7)
T_e	Enhanced electron temperature (5.7)
χ	Electron affinity of an insulator (5.7)
ϵ	Relative dielectric constant (5.7)
M	Mass density (5.7)
C	Heat capacity (5.7)
\bar{j}	Average field emission current density (5.7)

Chapter 1.

INTRODUCTION

1.1. VERY HIGH ENERGY COLLIDERS

The goal of elementary particle physics is to explore the ultimate secrets of matter and energy. Except for cosmic rays, only new colliders with ever higher center-of-mass energy can provide the experimental research conditions needed to explore the frontiers of high energy physics. First let us briefly answer a few basic questions, which will explain why we dedicate ourselves to develop the technology of electron-positron linear colliders with conventional accelerating structures.

- Proton-proton or electron-positron collider ?

Compared with a proton-proton collider, the electron-positron collider is superior in at least two respects:

- (a) The signal-to-background ratio at the constituent energies is much higher. Data analysis is easier.
- (b) There are no “partons” to share the momentum of the primary electron and positron. Therefore the collision energy is used more effectively.

- Circular or linear collider ?

The machines to give electron-positron collisions fall into two basic categories: colliding beam storage rings and linear colliders.

The technology for the storage rings is well understood. In conventional practice, the mean radius of a storage ring is chosen to be proportional to the square of the energy of the colliding beams to reduce the rapid increase of synchrotron radiation loss and thus to minimize the combined construction and operating costs. Even so, the cost of building a fixed luminosity storage ring scales as the square of the energy of its colliding beams.

The high energy linear collider is more cost effective because the synchrotron radiation losses are negligible. On the other hand, this new generation of colliders poses many challenges to accelerator designers. In order to yield high and stable luminosity, the extremely dense beams must have very low emittance and small energy spread, and a highly efficient accelerating system with accurate controls and diagnostics is required.

- Conventional or exotic acceleration ?

In the conventional process of RF acceleration, charged particles gain energy from electromagnetic fields which are generated by the motion of other charged particles in an RF source. There are a number of more exotic accelerating schemes such as laser and plasma acceleration, inverse free electron laser acceleration, wake field acceleration, and others. Some of these may reach accelerating gradients higher than the conventional RF method. However, due to the poor overall efficiency of power transfer and difficulties with beam phasing and control, no realistic breakthrough for these schemes has been made until now. In the relatively near future, the technically mature room-temperature RF-driven linac is still the best hope to realize a collider in the several hundred GeV center-of-mass energy range.

- Traveling-wave (TW) or Standing-wave (SW) accelerator structure ?

There is no simple answer to this controversy. From the point of view of structure efficiency and normalized power requirement, these structures are almost equivalent when one properly chooses the attenuation parameter for a TW structure or the coupling coefficient for a SW structure. The fabrication cost per unit length of a SW structure is at least 20% higher than a TW structure, but it does not require an output load to absorb the left-over power. As a high Q resonant structure, the SW accelerator reflects a large fraction of the incident RF power back to the power source during the filling time, and therefore, a high power isolator or a 3db hybrid are needed to absorb the reflected power. Many other factors also affect the choice between TW and SW structures, such

as the type of accelerating structure itself, beam loading, the simplicity and cost of RF and control systems, available RF power sources, etc. In the case of the linear collider powered by a super-high RF power source and pulse compression device, the TW structure is probably preferable.

This thesis concerns itself with the study of radio frequency properties of periodic accelerating structures for linear colliders and their interaction with bunched beams. The topics that have been investigated are:

- Experimental measurements of the energy loss of single bunches to longitudinal modes in two types of structures, using an equivalent signal on a coaxial wire to simulate the beam.
- A method of cancelling the energy spread created within a single bunch by longitudinal wakefields, through appropriate shaping of the longitudinal charge distribution of the bunch.
- Derivation of the complete transient beam-loading equation for a train of bunches passing through a constant-gradient accelerator section, with application to the calculation and minimization of multi-bunch energy spread.
- Detailed study of field emission and radio frequency breakdown in disk-loaded structures at S-, C- and X-band frequencies under extremely high-gradient conditions, with special attention to thermal effects, radiation, sparking, emission of gases, surface damage through explosive emission and its possible control through RF-gas processing.

1.2. LINAC RELATED RF PROPERTIES

Future e^+e^- linear colliders will require accelerating structures with a new set of properties. The requirements are summarized below:

- (a) High accelerating field gradient E_a to minimize machine length. This implies structures with a low ratio of peak-to-accelerating electric field E_p/E_a to minimize dark currents and the risk of electrical breakdown.

- (b) High ratio E_a^2/w where w is the energy stored in the structure per unit length. This ratio, which is equal to $\omega r/Q$ for the fundamental mode of the structure, is a measure of the efficiency with which the available microwave energy is used.
- (c) High group velocity v_g to reduce the filling time t_F , where $t_F = \ell/v_g$ for each section of length ℓ .
- (d) Low content of transverse and higher-order longitudinal modes that can be excited by the bunches traversing the structure. The longitudinal modes cause beam loading and energy spectrum widening while the transverse modes cause emittance growth.

Some of the principal parameters in linear accelerator theory which will be used frequently in the following chapters are listed below.¹

1. The shunt impedance per unit length r which measures the accelerating quality of a structure is defined as

$$r = - \frac{E_a^2}{dP/dz} \quad , \quad (1.1)$$

where E_a is the synchronous accelerating field amplitude and dP/dz is the RF power dissipated per unit length.

2. The factor of merit Q which measures the quality of an RF cavity as a resonator is defined as

$$Q = \frac{\omega w}{dP/dz} \quad , \quad (1.2)$$

where w is the RF energy stored per unit length and ω is the angular frequency.

3. The group velocity v_g which is the speed of RF energy flow along the accelerator is given by

$$v_g = \frac{P}{w} = \frac{\omega P}{Q dP/dz} \quad (1.3)$$

4. The attenuation factor τ of a constant-impedance or constant-gradient traveling-wave section is defined by the following expression:

$$\frac{P_{out}}{P_{in}} = e^{-2\tau} \quad (1.4)$$

For a constant-impedance section where the attenuation is uniform,

$$\tau = \frac{\omega \ell}{2v_g Q} = \alpha \ell \quad (1.5)$$

where ℓ is the length of the section and α is the attenuation constant in nepers per unit length.

For a constant-gradient section, the attenuation constant α is a function of z ($\alpha = \alpha(z) = \omega/2v_g(z)Q$) and we have the following expression:

$$dP/dz = -2\alpha(z)P = const = \frac{P_{in}(1 - e^{-2\tau})}{\ell} \quad (1.6)$$

We can derive other useful expressions from the above parameters, as show below.

5. The filling time t_F , which is required to fill a traveling-wave section of either constant impedance or constant gradient, is given by

$$t_F = \frac{2Q}{\omega} \tau \quad (1.7)$$

For a standing-wave section, the filling time is defined as the time needed to build up the field to $(1 - \frac{1}{e}) = 0.632$ times the steady-state field:

$$t_F = \frac{2Q_L}{\omega} = \frac{2Q_0}{(1 + \beta)\omega} \quad (1.8)$$

— where Q_0 is the unloaded Q , $Q_L = Q_0/(1 + \beta)$ is the loaded Q and β is the coupling coefficient of the section to the input microwave network.

6. The elastance is a convenient parameter, which is defined as

$$s = \frac{E_a^2}{w} = \omega \frac{r}{Q} = 4k_0 \quad (1.9)$$

where k_0 is the loss parameter for the fundamental mode. The elastance scales with the square of the frequency.

Now, let us list some relations dealing with RF energy and power. For a traveling-wave section with constant impedance, the following expressions hold:

1. The energy gain V of a charged particle is given by

$$V = (2\tau)^{\frac{1}{2}} [(1 - e^{-\tau})/\tau] (P_{in} r \ell)^{\frac{1}{2}} \quad (1.10)$$

2. The RF energy supplied in the time period t_F can be derived from (1.10) and other earlier expressions:

$$P_{in} t_F = \left(\frac{\tau}{1 - e^{-\tau}} \right)^2 \frac{V^2}{\omega \frac{r}{Q} \ell} \quad (1.11)$$

3. The energy W stored in the entire section at the end of the filling time can be expressed as

$$W = \frac{Q}{\omega} \int_0^{\ell} \frac{dP}{dz} dz = P_{in} \frac{Q}{\omega} (1 - e^{-2\tau}) \quad (1.12)$$

4. The structure efficiency η is defined as the ratio of the stored energy to the energy supplied by the source:

$$\eta = \frac{W}{P_{in} t_F} = \frac{1 - e^{-2\tau}}{2\tau} \quad (1.13)$$

5. The normalized peak power per unit length is defined as

$$P_{norm} = \frac{P_{in}/\ell}{E_a^2/r} = \frac{1}{1 - e^{-2\tau}} \quad (1.14)$$

where $E_a = V/\ell$ is the average gradient for the section.

For a traveling-wave section with constant gradient, we have the following expressions:

1. The energy gain V of a charged particle is given by

$$V = (1 - e^{-2\tau})^{\frac{1}{2}} (P_{in} r \ell)^{\frac{1}{2}} = (P_{dis} r \ell)^{\frac{1}{2}} \quad , \quad (1.15)$$

where $P_{dis} = P_{in} - P_{out} = (1 - e^{-2\tau})^{\frac{1}{2}} P_{in}$ is the power dissipated in the section.

2. The RF energy supplied in the time period t_F can be derived from (1.15) and other earlier expressions:

$$P_{in} t_F = \left(\frac{2\tau}{1 - e^{-2\tau}} \right) \frac{V^2}{\omega \frac{r}{Q} \ell} \quad . \quad (1.16)$$

3. The energy W stored in the entire section at the end of the filling time can be expressed as

$$W = \int_0^{\ell} \frac{P}{v_g} dz = P_{in} \frac{Q}{\omega} (1 - e^{-2\tau}) \quad . \quad (1.17)$$

4. The structure efficiency η is the ratio of the stored energy to the energy supplied by the source

$$\eta = \frac{W}{P_{in} t_F} = \frac{1 - e^{-2\tau}}{2\tau} \quad . \quad (1.18)$$

5. The normalized peak power per unit length is

$$P_{norm} = \frac{P_{in}/\ell}{E_a^2/r} = \frac{P_{in}/\ell}{dP/dz} = \frac{1}{1 - e^{-2\tau}} \quad , \quad (1.19)$$

— where r changes slowly along the structure and can usually be regarded as a constant.

It is interesting to note that the final expressions for W , η and P_{norm} for constant-impedance and constant-gradient structures are identical.

For a standing-wave section, we have the following expressions:

1. The energy gain of a charged particle is given by

$$V = (1 - e^{-t/t_F}) \frac{2\beta^{\frac{1}{2}}}{1 + \beta} (P_{in} r \ell)^{\frac{1}{2}} = (1 - e^{-t/t_F}) (P_{dis} r \ell)^{\frac{1}{2}} , \quad (1.20)$$

where β is the coupling coefficient of the structure.

2. The RF energy supplied to obtain an energy gain V at the end of a pulse length t_p can be minimized when $t_p = 1.257t_F$ and can be expressed as

$$P_{in} t_p = 1.257 \frac{2Q_0 P_{in}}{(1 + \beta)\omega} = 1.228 \left(1 + \frac{1}{\beta}\right) \frac{V^2}{\omega \frac{r}{Q} \ell} . \quad (1.21)$$

3. The energy W stored in the entire section at the end of the RF pulse can be expressed as

$$W = \frac{Q E_a^2}{\omega r} \ell = \frac{V^2}{\omega \frac{r}{Q} \ell} . \quad (1.22)$$

4. The structure efficiency η is given by

$$\eta = \frac{W}{P_{in} t_p} = \frac{1}{1.228} \left(\frac{1}{1 + \frac{1}{\beta}}\right) . \quad (1.23)$$

5. The normalized peak power per unit length is given by

$$P_{norm} = \frac{P_{in}/\ell}{E_a^2/r} = \frac{Q}{\eta \omega t_p} = \frac{1 + \beta}{2.514\eta} = 0.49 \frac{(1 + \beta)^2}{\beta} . \quad (1.24)$$

1.3. INTERACTION BETWEEN THE BEAM AND ACCELERATING STRUCTURE

The interaction between a bunched beam and the accelerating structure constitutes one of the important issues in the design of a linear collider. Charged particles in a bunch leave behind them wake fields of two types: longitudinal and transverse. The first cause energy loss, the second cause emittance growth. For a practical design, these interactions set an upper limit on the number of charged particles in a bunch and the number of bunches in a multibunch train.

The wake field effects can be analyzed in the short range and the long range.

1. Short range effect

In the short range, bunches lose energy to high order longitudinal modes when they traverse the accelerating structure. The energy losses can be calculated using computer programs such as KN7C, URMEL and TBCI

or they can be obtained experimentally. A bench measurement method for the energy loss of single bunches and experimental results for a few periodic accelerating structures are presented in Chapter 2.²

The longitudinal wake produces an energy spread within the bunch. By placing the bunch ahead of the crest of the RF wave and by properly shaping its longitudinal charge distribution, a possible method to completely cure this energy spread is given in Chapter 3.³

In the short range, the transverse wake fields deflect all particles behind the head of a bunch away from the axis of the accelerating structure. This effect can be controlled by keeping each bunch as closely as possible to the axis and by using a very tightly focused quadrupole lattice. Also, the so-called BNS damping technique⁴ can be used to cause the tail of each bunch to have a lower energy and thus be submitted to stronger focusing.

2. Long range effect

In the long range, the longitudinal wake field causes energy spread in a multibunch train. Chapter 4 starts with a general transient beam loading solution. Then, cases for bunch train injection both before and after filling-up of a section are analyzed. Finally, the best energy compensation condition, the maximum energy deviation and the time when the maximum energy deviation occurs are derived for the multibunch operating mode. Another cure is to use an accelerating structure with radial slots which can damp higher-order longitudinal modes without seriously affecting the fundamental accelerating mode.⁵

In the long range, the transverse wake fields cause multibunch blow-up. This problem can be alleviated by adjusting the frequency of the transverse dipole mode so that the bunches are located at the zero crossings of the wake field and by using a damped accelerating structure as mentioned above.

1.4. HIGH ACCELERATING GRADIENT AND RELATED PROBLEMS

The operating gradient of the accelerator structure determines the length of the linear collider. Even though we know that the required peak RF power increases as the square of the gradient, the optimum machine length for a given energy cannot be determined at this time because we have no definitive knowledge of the availability and cost of RF sources. However, for some design examples, gradients as high as 200 MV/m are required at RF frequencies of 11.424 GHz or 17.136 GHz. Are these accelerating gradients reachable? What other phenomena will accompany this extremely high field condition inside the accelerating structure? In this thesis, Chapter 5 deals with the broad aspects of high RF gradients and breakdown studies at SLAC.

Several accelerating sections were designed, manufactured and tested at high gradient.⁶ S-band experiments were done on a seven-cavity disk-loaded ($2\pi/3$ -mode) structure and a two-cavity nose-cone-shaped (π -mode) structure, powered

by a klystron operated up to 47 MW. C-band and X-band tests, done in collaboration with Varian, used nose-cone-shaped half-cavity structures powered by ~ 1 MW magnetrons. One X-band test was started in collaboration with LLNL but has not yet been completed. The experimental results, obtained at pulse lengths between 1.5 and 4 μs , indicate that similarly to the Kilpatrick criterion,⁷ the breakdown gradient varies roughly as the square-root of the RF frequency but that the thresholds are roughly seven times higher. Intensive studies were carried out of both pre-breakdown and breakdown phenomena, during and after RF processing. The physical mechanisms of enhanced field emission and RF breakdown are discussed to try to explain the experimental results.

Chapter 2.

ENERGY LOST TO LONGITUDINAL MODES BY SINGLE ELECTRON BUNCHES TRAVERSING PERIODIC STRUCTURES

2.1. MOTIVATION

In the design of linear colliders, it is important to know and minimize the loss of beam energy due to the excitation of higher-order modes in the accelerator structure by single bunches of electrons or positrons. This loss is not only detrimental in itself but also gives rise to energy spectrum widening and transverse emittance growth. The energy loss can be calculated for simple structures with cylindrical symmetry such as the disk-loaded waveguide by using programs like KN7C, URMEL and TBCI. For more complicated structures such as the square-cross-section Jungle Gym or the cylindrical waveguide with alternating spokes or slotted disks, the three-dimensional code MAFIA can calculate the loss parameters approximately. To verify these calculations, the longitudinal and transverse wake fields can be excited and measured with an electron beam,^{8,9} but these measurements require that a long length of accelerating structure be available. Alternatively, a simple bench test to measure the longitudinal higher-order mode content of structures was performed at SLAC.^{10,11} In this measurement a Gaussian bunch was simulated by a current pulse of the same shape transmitted through the structure on a co-axial center conductor. A conceptual method to measure the transverse modes has also been proposed¹² but has not been tried experimentally.

2.2. LOSS PARAMETER

When a single charged particle or a bunch of particles traverse a cavity at the speed of light, they produce electromagnetic fields inside the cavity and induce

charges and currents in the cavity walls. These induced charges and currents create wake fields inside the cavity, which can decelerate and transversely deflect the beam.

The fundamental theorem of beam loading¹³ states that if a point charge at the speed of light traverses an initially empty cavity, the energy loss ΔU_n to a given mode n is equal to one-half of its own beam-induced voltage in this mode, V_n , times its electric charge q . This means that the effective voltage V_{ne} seen by the charge is only one-half of the charge-induced voltage V_n , i.e. $V_{ne} = V_n/2$. The voltage is obviously proportional to the charge of the driving particle, i.e.

$$V_{ne} = k_n q \quad , \quad (2.1)$$

or

$$V_n = 2k_n q \quad , \quad (2.2)$$

where the factor k_n is called the loss parameter.

By energy conservation, after a particle traverses a cavity, the energy W_n left behind is equal to the energy ΔU_n which it has lost:

$$W_n = \Delta U_n = V_{ne} q = k_n q^2 \quad . \quad (2.3)$$

For a resonant cavity, the shunt impedance for the n^{th} mode is defined as $R_n = V_n^2/P_n$, where P_n is the power dissipated in the cavity. The factor of merit Q for the n^{th} mode is defined as $Q_n = \omega_n W_n/P_n$, where ω_n is the angular frequency of the n^{th} mode. The ratio R_n/Q_n is a very basic parameter for a cavity and it can be expressed as

$$\frac{R_n}{Q_n} = \frac{V_n^2}{\omega_n W_n} \quad , \quad (2.4)$$

This ratio depends only on the geometric configuration of the cavity and it scales as ω .

By substituting V_n and W_n from (2.2) and (2.3) into (2.4), one obtains

$$k_n = \frac{\omega_n}{4} \left(\frac{R_n}{Q_n} \right) . \quad (2.5)$$

For a delta-function point unit charge passing through a single component of a beam line or an initially empty cavity, the longitudinal wake can be defined as the potential experienced by a test charge along the same path at time τ behind the unit charge. If we assume that there are no overlapping modes, we can superimpose all the potentials resulting from the individual modes. The longitudinal wake potential for a resonant cavity can then be expressed as

$$\begin{aligned} w(\tau) &= 0 & \tau < 0 \\ w(\tau) &= 2 \sum_{n=0}^{\infty} k_n \cos \omega_n \tau & \tau \geq 0 \end{aligned} . \quad (2.6)$$

Any moving bunch of charged particles can be described by a current distribution $I(t)$ or $I(z)$. From the definition of the wake potential, the potential V_b at some position corresponding to time t due to the cavity-particle interaction can be expressed as

$$V_b(t) = \int_{-\infty}^t w(t - \tau) I(\tau) d\tau = \int_0^{\infty} w(\tau) I(t - \tau) d\tau . \quad (2.7)$$

On the basis of causality, only the particles before t make a contribution to $V_b(t)$. The total energy loss of the bunch can be calculated by performing the following integration:

$$\Delta U_{tot} = \int_{-\infty}^{\infty} V_b(t) I(t) dt . \quad (2.8)$$

The total loss parameter K_{tot} is defined by the following relation:

$$\Delta U_{tot} = K_{tot} q^2 , \quad (2.9)$$

where q is the total charge of the bunch.

The total loss parameter can be expressed as

$$K_{tot} = \frac{1}{q^2} \int_{-\infty}^{\infty} V_b(t) I(t) dt \quad . \quad (2.10)$$

The energy loss parameter for all modes is equal to the summation of the energy loss parameters to the fundamental mode and all the higher modes. It also can be written as

$$K_{tot} = k_0 + \sum_{n=1}^{\infty} k_n \equiv B k_0 \quad (2.11)$$

where B is called the beam loading enhancement factor.¹⁴

For the case of a Gaussian bunch, the total loss parameter is the summation of the loss parameters for each mode with its frequency-dependent factor as shown:

$$K_{tot} = \sum_{n=0}^{\infty} k_n e^{-\omega_n^2 \sigma^2} \quad (2.12)$$

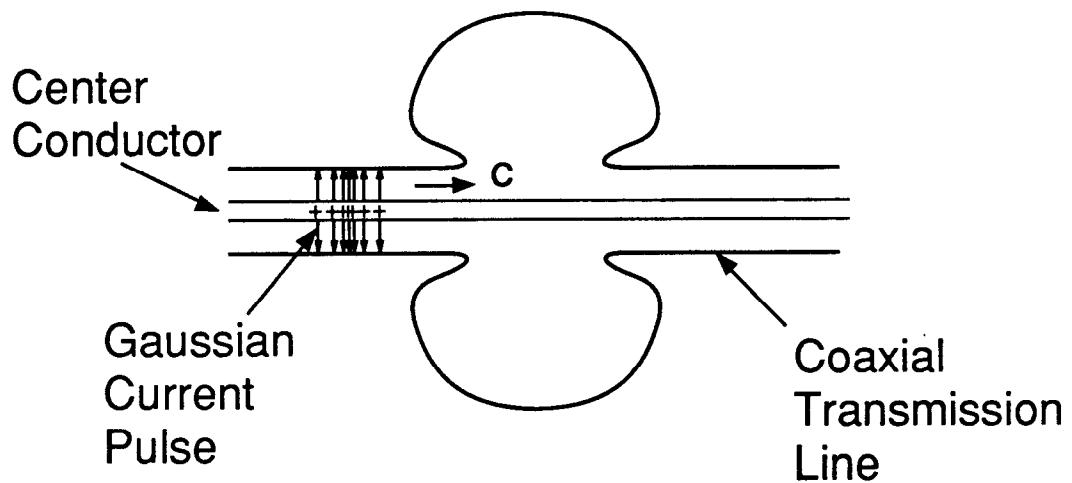
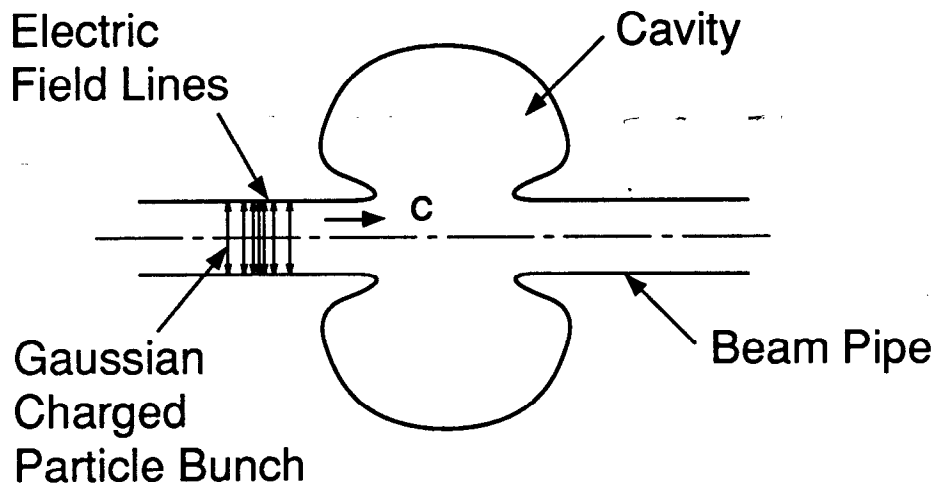
where σ is the standard deviation of the Gaussian bunch.

2.3. CALCULATION AND MEASUREMENT OF THE LOSS PARAMETER

For a resonant cavity the computer programs mentioned earlier are available to calculate the ratios R_n/Q_n and the resonant frequencies ω_n . From (2.5) and (2.11) we have

$$K_{tot} = \sum_{n=0}^{\infty} \left(\frac{\omega_n}{4}\right) \left(\frac{R_n}{Q_n}\right) e^{-\omega_n^2 \sigma^2} \quad . \quad (2.13)$$

To analyze more complicated structures, M. Sands and J. Rees proposed a method to measure the energy loss to parasitic modes by a pulse comparison technique.¹⁵ This method was used extensively for the optimization of the storage ring PEP vacuum chamber components. The electron bunch was simulated by a current pulse of the same shape transmitted on an axial wire stretched through the structure as shown in Fig. 2.1.



2-89

6110A8

Fig. 2.1. Comparison of charged particle bunch traversing an empty structure and current pulse propagating along a center conductor in the structure.

A short pulse of current introduced on the left end of the center conductor can travel along the center conductor with the speed of light. If the current pulse shape is Gaussian, the instantaneous Gaussian charge density distribution along the conductor can simulate the charge density of a traveling Gaussian bunch. Because the walls have sufficiently low resistivity, the wake fields inside the short and smooth pipes can be neglected.

When a charged particle bunch or a current pulse passes through the cavity, the induced current and charges on the walls change, and wake fields are generated. For the case of a particle bunch, the longitudinal wake fields change the energy of the particles in the bunch but do not disturb the distribution of the ultra-relativistic particles significantly. The energy change of each particle is obtained from the integral of the wake potentials created by all the particles ahead of it in the bunch. The total energy change of the bunch is the sum of the energy changes of all the particles in the bunch. In the case of the current pulse on the center conductor, the wake fields field induces a secondary current on the center conductor which in turn modifies the resultant current pulse.

Let us now discuss the effect of the center conductor. First, the resonant frequency and field distribution change very little if the diameter of the center conductor is sufficiently small compared with the dimensions of the structure. Second, the electromagnetic energy left in the structure decays quite differently after the passage of the particle bunch as compared to the current pulse. In the case of the particle bunch traversing an empty cavity, all the modes oscillate and their energies are eventually transformed into heat in the walls. In the case of the current pulse traveling along the center conductor, the energy is coupled into the center conductor, travels along it and ultimately is dissipated in the terminations at the two ends. It should be noticed that the current pulse is very short compared to the relaxation time of the residual fields in the presence of the center conductor, even considering the enormous reduction of the quality factor Q due to the existence of the center conductor. The energy removed from the current pulse is therefore still similar to the energy removed from the particle

bunch.

Now let us show that if we can measure the energy loss for the current pulse, we can derive the energy loss for the bunch traversing the same structure. When a current pulse $i_0(t)$ travels along a coaxial transmission line with characteristic resistance R , the energy contained in the pulse is

$$U_1 = R \int i_0^2(t) dt \quad . \quad (2.14)$$

If we replace the smooth pipe by a cavity, the modified current pulse, $i_m(t) = i_0(t) - i_f(t)$, travels forward and the reflected current pulse $i_r(t)$ travels backward. The total energy becomes

$$U_2 = R \int [i_0(t) - i_f(t)]^2 dt + R \int i_r^2(t) dt \quad . \quad (2.15)$$

From energy conservation, $U_2 = U_1$, and

$$2R \int i_f(t) i_0(t) dt = R \int [i_f^2(t) + i_r^2(t)] dt \quad . \quad (2.16)$$

The left-hand side of Eq. (2.16) is the energy “lost” from the initial pulse, and the right-hand side is the energy “deposited” in the cavity, and subsequently released to the coaxial line. The above discussion also holds true for the charged particle bunch. The only change is that in the time interval Δt , the charge Δq that flows equals $i(t)dt$. Thus, the total energy loss can be expressed as

$$\Delta U_{tot} = 2R \int i_f(t) i_0(t) dt = K_{tot} q^2 \quad , \quad (2.17)$$

where q is the total charge in the bunch.

By taking the average of the reference and modified current pulses, one gets an expression which can be used in the experiments:

$$K_{tot} = \frac{2R}{q^2} \int [i_0(t) - i_m(t)] \left[\frac{i_0(t) + i_m(t)}{2} \right] dt \quad , \quad (2.18)$$

where

$$q = \frac{1}{2} \int [i_0(t) + i_m(t)] dt \quad . \quad (2.19)$$

2.4. MEASUREMENT SET-UP

The measurement set-up is illustrated in Fig. 2.2. In order to minimize internal reflections, conical tapers and extended cylinders are provided on each side of the test piece to connect it to 50Ω coaxial transmission lines. The Gaussian pulse generator on the left consists of a tunnel diode step-generator and a tee-junction with a shorted stub (available in several lengths) by means of which a short pulse of desired duration is produced. A low-pass filter is used to make the pulse Gaussian. On the right a sampling head and oscilloscope are connected to an X-Y recorder which plots the transmitted pulses. In order to minimize jitters and drifts, all active components are thermally stabilized by means of water cooling.

One of the most important features of these tests has to do with the σ_z of interest in future colliders. If one assumes an S-band structure like at SLAC (2856 MHz), then $\sigma_z = 1$ mm or $\sigma_t = 3.33$ ps. Unfortunately, the best available step generator has a rise time t_r with a lower limit of 20 ps, leading to a Gaussian pulse with a σ_t of at least 28 ps. For this reason, it was necessary to scale all the dimensions of the test piece from S-band by an enlargement factor s . If we use primed parameters for the scaled model, we can get the following relation from (2.13):

$$K_{tot} = K'_{tot} \frac{\sum_{n=0}^{\infty} (\frac{\omega_n}{4}) (\frac{R_n}{Q_n}) e^{-\omega_n^2 \sigma^2}}{\sum_{n=0}^{\infty} (\frac{\omega'_n}{4}) (\frac{R'_n}{Q'_n}) e^{-\omega_n'^2 \sigma'^2}} \quad , \quad (2.20)$$

where the ratio (R_n/Q_n) does not change if we scale our structure in all dimensions. If we scale σ inversely with ω so as to keep

$$\omega_n \sigma = \omega'_n \sigma' \quad , \quad (2.21)$$

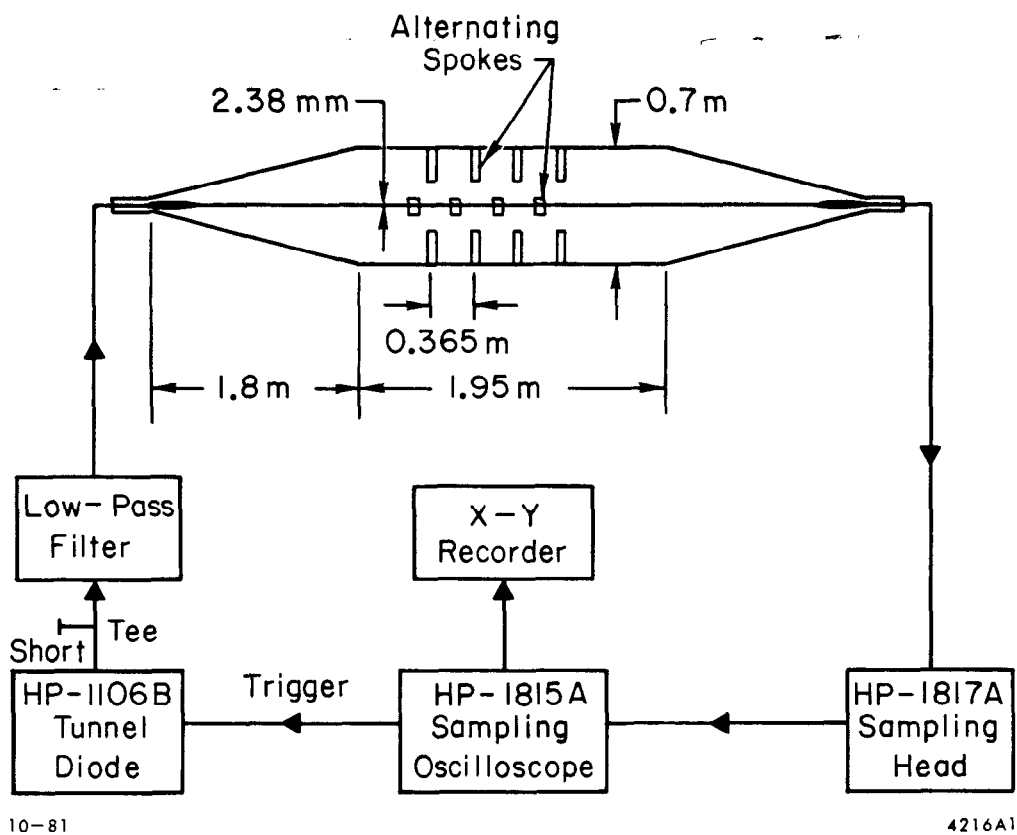


Fig. 2.2. Measurement layout.

the measured K'_{tot} scales directly with frequency and is simply lower than K_{tot} by the factor s . In the experiments, scaling factors of 8.5 for the SLAC structure measurement and 10.4 for the alternating-spoke structure measurement were adopted. This resulted in a test cell with an I.D. of 70.8 cm and a periodic length of about 30 cm. Although somewhat cumbersome, the structure was not too costly to build from aluminum sheet and extruded parts.

In addition to the scaling problem, it was necessary to correct the pulse widening due to the finite rise time t_r of the sampling head and oscilloscope ($t_r = 38$ ps). This correction from the measured σ'_m to σ' was effected by using the following relation:

$$\sigma' = (\sigma_m'^2 - \sigma_r^2)^{1/2} \quad , \quad (2.22)$$

where $\sigma_r = 0.39t_r$ and σ'_m is the measured standard deviation.

2.5. MEASUREMENTS AND RESULTS

The measurements were made in two steps. In the first step, the test piece was simply a hollow pipe of inner diameter proportional to that of the accelerator structure (commonly called $2b$, see Fig. 2.3). The current pulse transmitted through the system to the recorder was $i_0(t)$.

In the second step, the internal periodic elements of the structure were added one by one (the total length was kept constant), and the transmitted pulses $i_m(t)$, which were modified by the successive additions of obstacles, were recorded by using an X-Y recorder. Fig. 2.4 shows the successive pulses $i_1(t)$, $i_2(t)$, $i_3(t)$, $i_4(t)$ and $i_5(t)$ corresponding to the successive additions of the obstacles.

The curves obtained from the X-Y recorder were digitized by means of a graphic-to-digital converter. By using the digitized data as a program input, the computer performed the integration of Eq. 2.18. The difference between the loss parameters calculated from two successive curves is the loss parameter of a cell. For all structures measured here, it was found that the results converged in a

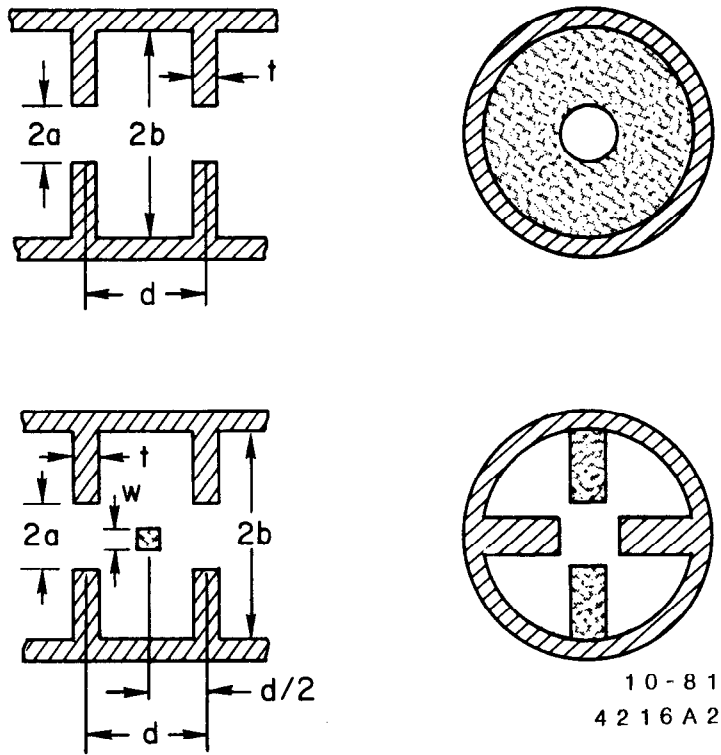
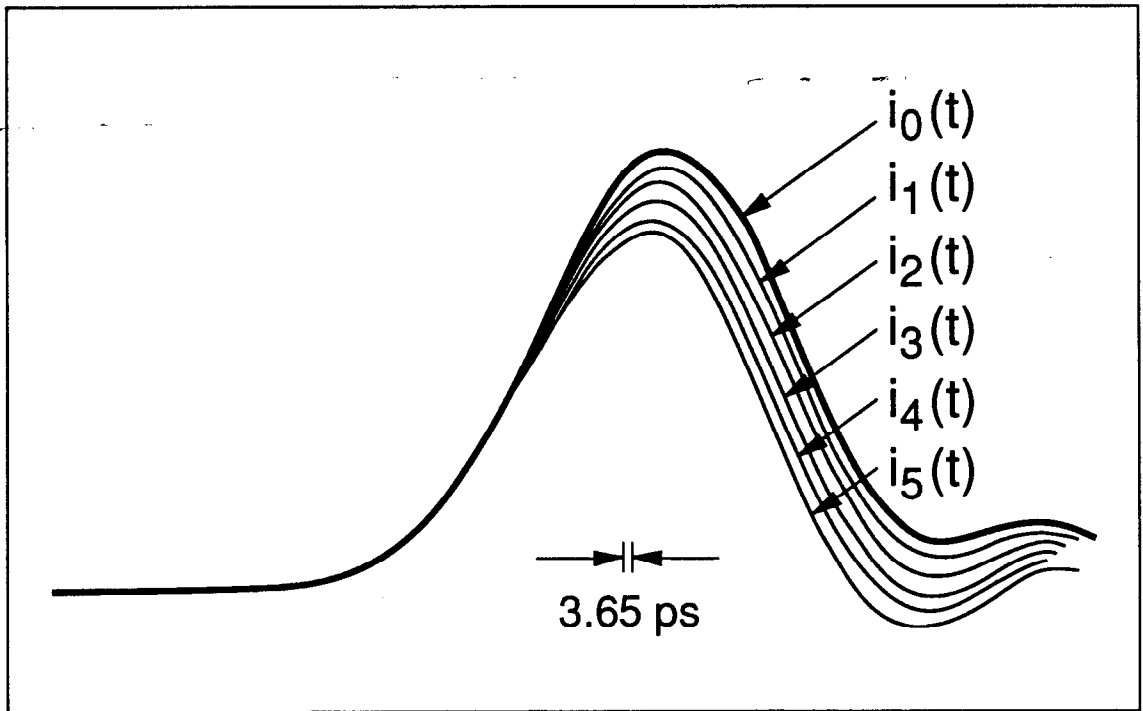


Fig. 2.3. Accelerating structures tested: a) Disk-loaded structure, b) Alternating-spoke structure.



2-89

6110A9

Fig. 2.4. Successive current pulses recorded by X-Y plotter.

satisfactory manner after three or four periods, and an average loss parameter per cell was obtained.

Measurements were performed for two types of structures. The first was the disk-loaded waveguide ($2\pi/3$ mode) used at SLAC. This measurement was made for two (scaled) values of the dimension $2a$ (see Fig. 2.3a) corresponding to the 45th (average) cavity of the constant-gradient structure ($2a = 2.325$ cm) and the largest cavity ($2a = 2.622$ cm). The change in the corresponding $2b$ (8.265 cm to 8.346 cm or about 1%) was neglected. The measurement for each structure was made for four different values of σ as shown in Table I.

Table 2.1. Results of Measurements for Disk-Loaded Structures

σ (mm)		Scaled Loss per Period, K (V/pc)		α
Measured	Scaled to 2856 MHz	$2a = 2.325$ cm $v_g/c = 0.0130$	$2a = 2.622$ cm $v_g/c = 0.0204$	$(K \propto a^{-\alpha})$
8.5	1.00	2.82	2.30	1.69
10.1	1.19	2.65	2.22	1.47
12.4	1.46	2.48	2.03	1.66
15.6	1.84	2.22	1.77	1.88

For each pulse length, five data points were obtained from differences between the cases for no disk, one, two, three, four and five disks cumulatively added in succession, and an average K was calculated. The results are given in Table 2.1 and plotted in Fig. 2.5. It is interesting to note that the microwave measurement for the “average” (45th cavity) iris agrees very well with the single-bunch measurement described in Ref. 8 when normalized to a Gaussian distribution with a $\sigma = 1$ mm. Both measurements give values of K that are $\sim 35\%$ higher than the theoretically calculated curve, also shown in Fig. 2.5. This discrepancy is identical to that originally mentioned in Ref. 8. The resulting values of B with $\sigma_z = 1$ mm are 4.24 for $2a = 2.325$ cm and 3.79 for $2a = 2.622$ cm. In the last column of Table 2.1, notice that the factor α , calculated for each σ , assumes that K varies as $a^{-\alpha}$. The average of all four values is $\alpha = 1.68$, identical to the

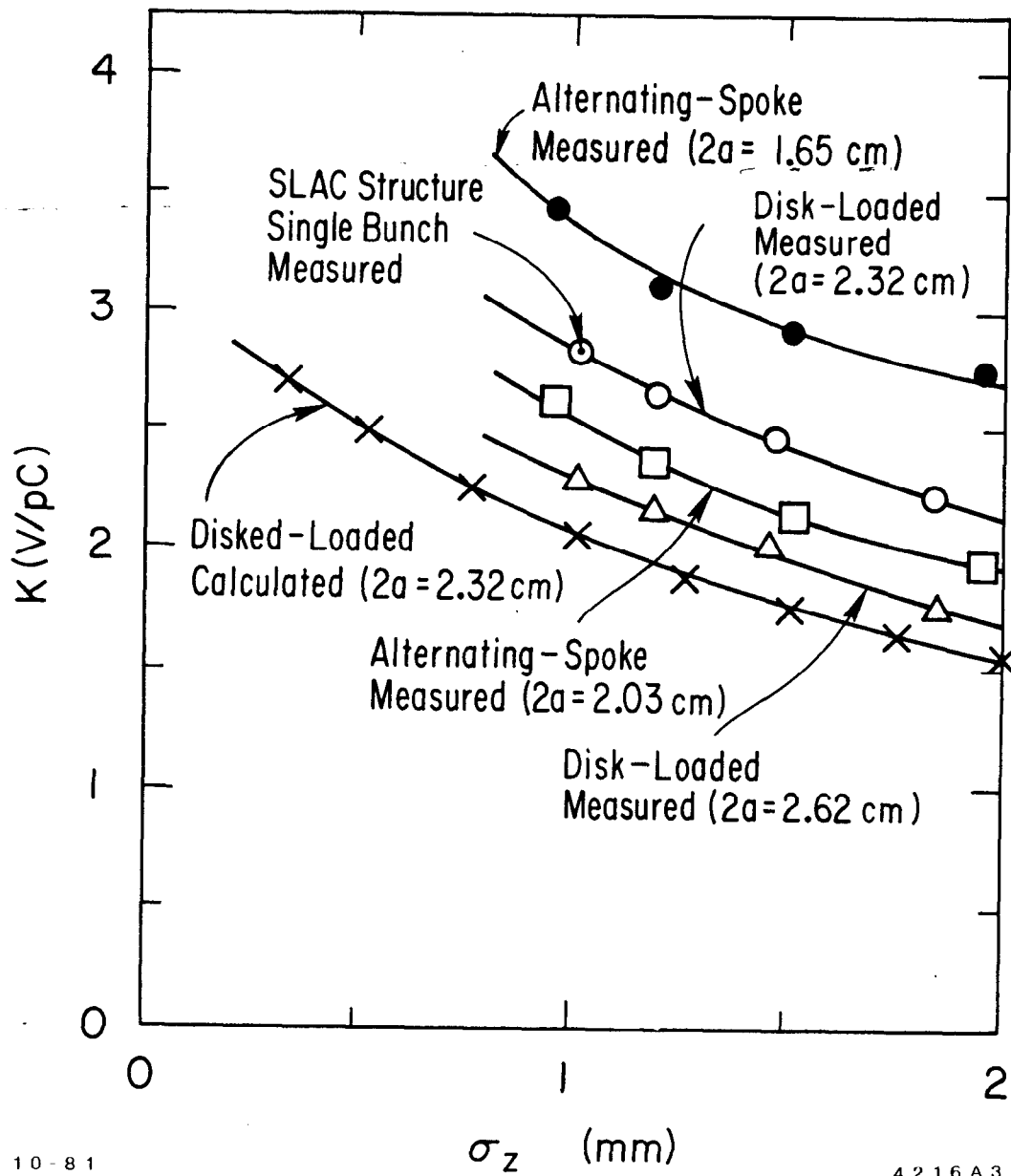


Fig. 2.5. Total loss parameter per period, as a function of σ_z , as obtained from computer calculation, SLAC linac beam loading measurements and bench tests normalized to 2856 MHz.

theoretically predicted value.¹⁶ This result is reassuring because even if the microwave measurements should suffer from a systematic error, the relation between measurements for different values of $2a$ seems to be consistent with theory.

The second set of measurements was made for the alternating-spoke structure shown in Fig. 2.3b. This structure, which is similar to the Jungle Gym, consists of a pair of radial bars which protrude into the circular guide, alternating by 90° . A complete period consists of two pairs of bars and is $\lambda_0/3$ in length ($2\pi/3$ mode): the phase shift from bar to adjacent bar is $\pi/3$. This structure was selected because of its openness, relatively high r_0/Q_0 (~ 4000 ohms/m at 2856 MHz) and high group velocity ($v_g/c \sim 0.150$)¹⁷. The results are shown in Table 2.2 for two different values of $2a$, as defined in Fig. 2.3b.

The results are also plotted in Fig. 2.5. It is seen that the lowest value of K is found for the example with $2a = 2.032$ cm. For $\sigma = 1$ mm and $2a = 2.032$ cm, $B = 3.83$. In the scaled-up version, the spokes had a rectangular cross-section. A further improvement in K is expected for the π -mode, *i.e.*, two pairs of spokes per half-wavelength.

Table 2.2. Results of Measurements for Alternating-Spoke Structure

σ (mm)		Scaled Loss per Period $K(\text{V/pC})$	
Measured	Scaled to 2856 MHz	$2a = 1.651$ cm	$2a = 2.032$ cm
10.1	0.97	3.43	2.63
12.4	1.19	3.12	2.37
15.6	1.50	2.93	2.15
20.3	1.95	2.78	1.95

2.6. CONCLUSIONS

The measurements presented here indicate that a microwave bench test on a scaled structure can predict, at least comparatively from structure to structure, the total energy lost per period to all the longitudinal modes by a Gaussian bunch of total charge q . Since the method requires only inexpensive models, it can be used to check fairly quickly the results of theoretical calculations.

Chapter 3.

MINIMIZING THE ENERGY SPREAD WITHIN A SINGLE BUNCH BY SHAPING ITS CHARGE DISTRIBUTION

3.1. MOTIVATION

As we discussed earlier, when electron or positron bunches pass through the periodic structure of a linear accelerator, they leave behind them energy in the form of wake fields. For a linear collider, the energy spread introduced within the bunches by this beam loading effect must be minimized because it limits the degree to which the particles can be focused to a small spot because of chromatic effects in the final focus system. For example, for the SLC, the maximum allowable energy spread is less than $\pm 0.5\%$.

It has been known for some time that partial compensation of the longitudinal wake field effects can be obtained for any bunch by placing it, on average, ahead of the accelerating crest (in space), thereby letting the positive rising sinusoidal field offset the negative beam loading field.¹⁸ The work presented in this chapter shows that it is possible to obtain complete compensation, i.e., to reduce the energy spread essentially to zero by properly shaping the longitudinal charge distribution of the bunch and by placing it at the correct position on the wave.

3.2. OPTIMIZING THE BUNCH SHAPE

The energy gained by a single particle riding at an angle θ_1 with respect to the crest of a traveling wave of accelerating gradient E_0 over a length L is

$$V = E_0 L \cos \theta_1 . \quad (3.1)$$

In the case of a bunch consisting of many particles, this energy is modified by the presence of the wake fields left by particles ahead of θ_1 . As an example, we

will use the SLAC constant-gradient structure although the technique should be applicable to any structure for which the longitudinal wake potential is known.

For a point unit charge passing through a single cavity, the longitudinal wake can be calculated from (2.5) and (2.6). For the SLAC disk-loaded constant-gradient accelerator structure, the dimensions of cavity No. 45 were chosen to calculate the wake field. The calculation was composed of two steps. First, the frequencies ω_n and the loss parameters k_n of 416 lower modes were computed by the program KN7C. For a linear collider at S-band in which the bunch length σ_z is about 1 mm, all modes with frequency up to 3×10^{11} Hz should be counted. Thus, the above mode summation method met a practical difficulty in calculation accuracy. Fortunately the statistical properties of the higher modes can be accurately represented by the so-called optical resonator model.¹⁹ Therefore, the second step was to add the contribution of an analytical term, as shown:

$$\begin{aligned}
 w(\tau) &= 0 & \tau < 0 \\
 w(\tau) &= 2 \sum_{n=0}^m k_n \cos \omega_n \tau + 2 \int_{\omega_n}^{\infty} \frac{A_m \cos \omega \tau}{\omega^{3/2}} d\omega & \tau \geq 0
 \end{aligned} \tag{3.2}$$

where

$$k_n = \frac{\omega_n}{4} \left(\frac{R_n}{Q_n} \right) , \tag{3.3}$$

and A_m is a constant determined by fitting $\Delta k = A_m \Delta \omega / \omega^{3/2}$ for the parameters near ω_m when m is large enough to use this model.

Fig. 3.1 shows the longitudinal wake per cell for the average SLAC disk-loaded structure as defined above. For convenience the wake is plotted as a function of the phase angle behind the driving charge, where

$$\theta = 360 \times 2856 \times 10^6 \times \tau \quad (\text{degrees}) . \tag{3.4}$$

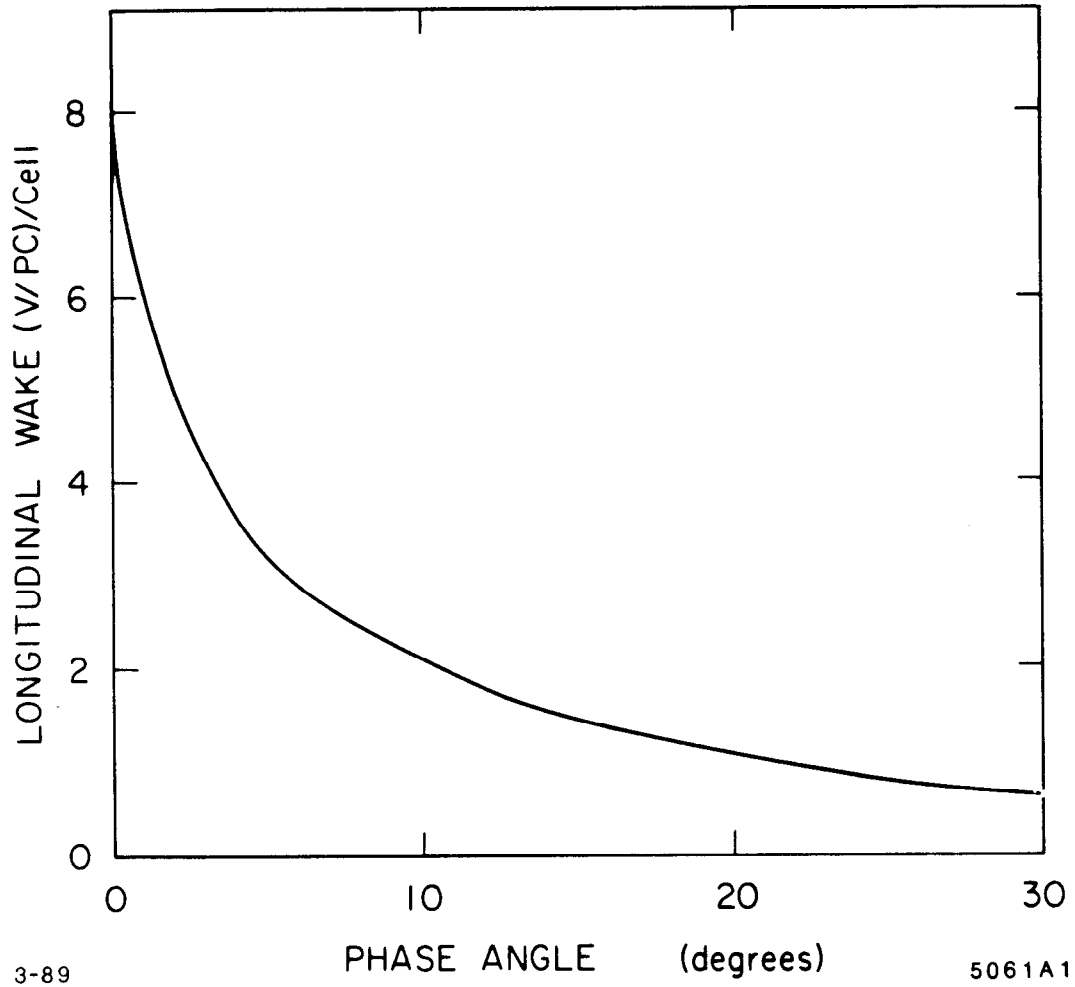


Fig. 3.1. Longitudinal wake function per cell as a function of phase angle for SLAC constant-gradient structure.

At the cost of an error estimated to be on the order of 5%, we can neglect the fact that the actual cavities differ in iris diameter from this average cavity by about $\pm 15\%$. We can then obtain the function W_L for the entire accelerator by simply multiplying $w(\theta)$ by N , the total number of cavities. With the definitions of phase angles and a bunch charge distribution $f(\theta')$ illustrated in Fig. 3.2, the energy gain of a particle riding at an angle θ_1 becomes:

$$V(\theta_1) = V_0 \cos \theta_1 - \int_0^{(\theta_0 - \theta_1)} f(\theta') W_L(\theta_0 - \theta_1 - \theta') d\theta' \quad , \quad (3.5)$$

where $V_0 = E_0 L$, θ_0 is the position of the head of the bunch with respect to the RF peak and θ' , the coordinate within the bunch, is made to vary from 0 (the head of the bunch) to $\theta_0 - \theta_1$ (the position where we want to know the net energy).

In order to reduce the energy spread within the bunch to zero, we must make $V(\theta_1)$ independent of θ_1 . This requires that

$$\frac{\partial V(\theta_1)}{\partial \theta_1} = 0 \quad . \quad (3.6)$$

By taking the partial derivative of Eq. (3.5) with respect to θ_1 and setting it to zero, we get:

$$\begin{aligned} -V_0 \sin \theta_1 - \int_0^{(\theta_0 - \theta_1)} f(\theta') \frac{\partial W_L}{\partial \theta_1}(\theta_0 - \theta_1 - \theta') \\ d\theta' + f(\theta_0 - \theta_1) W_L(0) = 0 \quad , \end{aligned}$$

or

$$f(\theta_0 - \theta_1) = \frac{V_0}{W_L(0)} \sin \theta_1 + \int_0^{(\theta_0 - \theta_1)} \frac{f(\theta') \frac{\partial W_L}{\partial \theta_1}(\theta_0 - \theta_1 - \theta')}{W_L(0)} d\theta' \quad . \quad (3.7)$$

Letting $\theta_0 - \theta_1 = x$ where $x \geq \theta'$, Eq. (3.7) becomes:

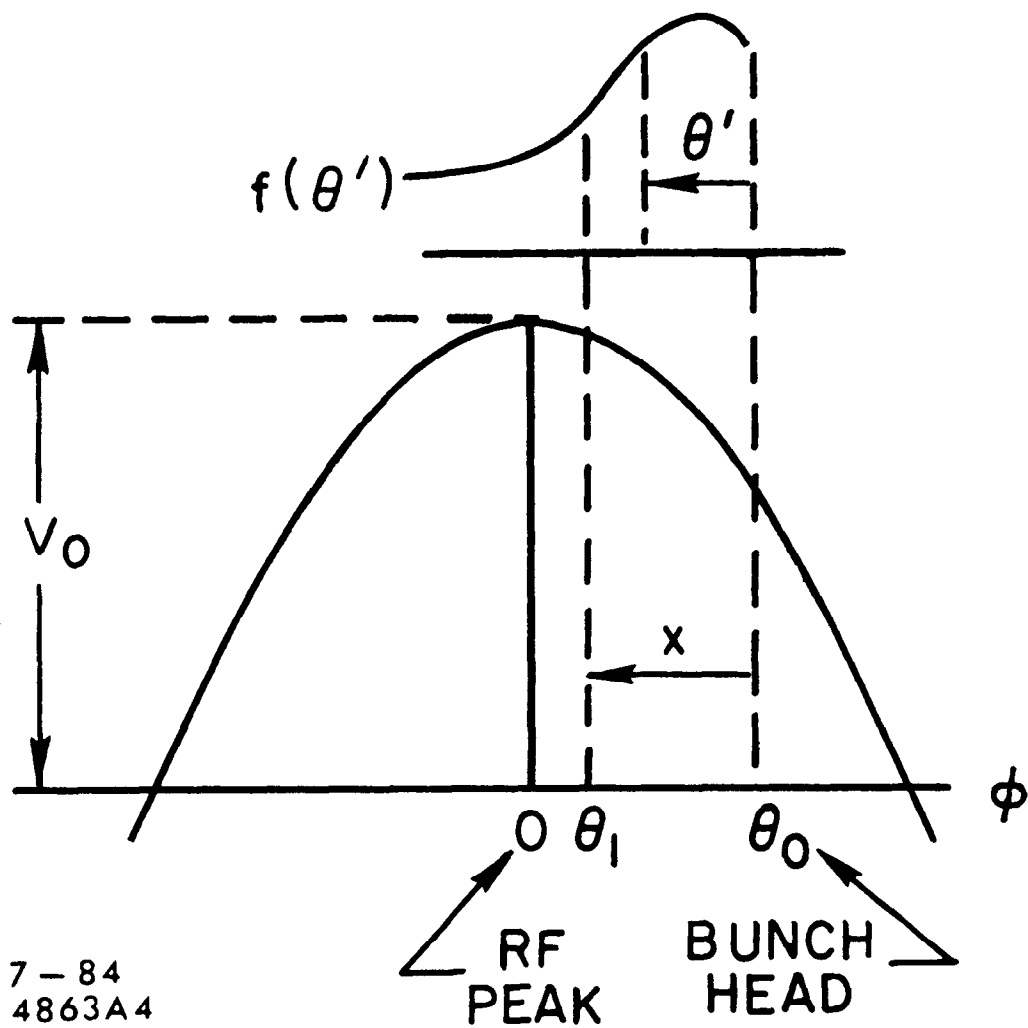


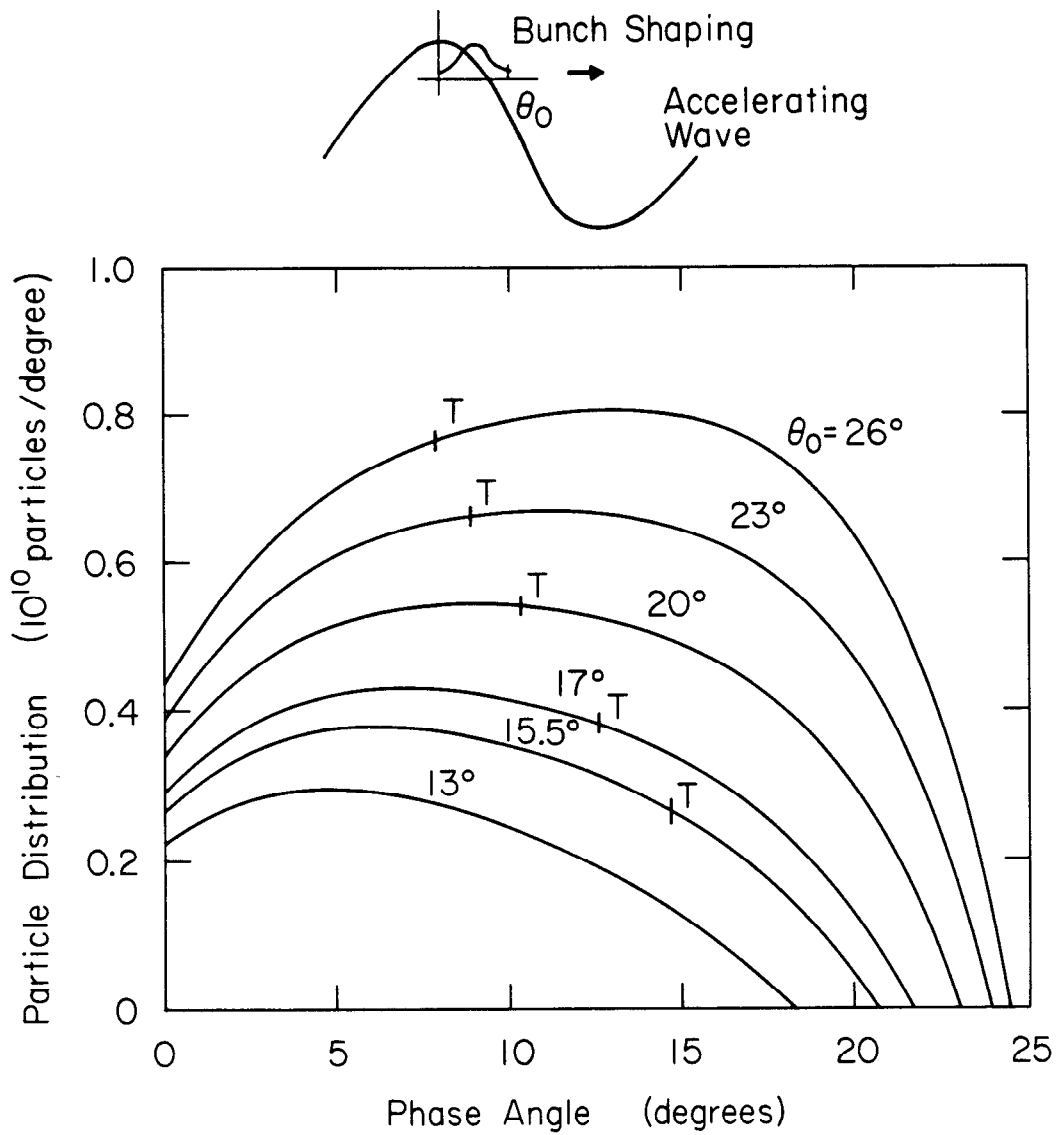
Fig. 3.2. Definitions of phase angles showing position of bunch with respect to accelerating wave. The charge distribution is $f(\theta')$ and the maximum energy gain is V_0 .

$$f(x) = \frac{V_0}{W_L(0)} \sin(\theta_0 - x) - \int_0^x \frac{\frac{\partial W_L}{\partial x}(x - \theta') f(\theta')}{W_L(0)} d\theta' \quad (3.8)$$

which is a Volterra integral equation of the second kind. This equation can be solved digitally through a multi-step method using Day's starting procedure in conjunction with Simpson's rule and the three-eighth rule.²⁰ The wake function can be fitted with a polynomial so as to be represented by an analytical expression.

Figures 3.3 and 3.4 give results for several examples. These examples were all worked out for a no-load energy V_0 of 54.75 GeV, an accelerator length L of 960 sections, each with 86 cavities (i.e., $L = 2890$ m, $N = 82,560$ cavities) and a bunch of integrated charge $5 \times 10^{10} e$. The value of V_0 was chosen so as to yield a final beam energy just over 50 GeV. Figure 3.3 shows six different bunch shapes with the corresponding θ_0 's (positions of the head with respect to the wave) required to give essentially zero energy spread. The head of the bunch is on the left (zero-abscissa) and the tail defined as the point where an integrated charge of $5 \times 10^{10} e$ is reached, is at the abscissa corresponding to the letter "T" on each curve. An interesting aspect of these curves is that if the bunches are extended beyond the "T" points as shown, the energy spread continues to be zero even though the charge in the extended bunch is greater than $5 \times 10^{10} e$. The end points on the individual curves give the limits of how far one can go. The curve for $\theta_0 = 13^\circ$ has no T because the integral under it does not quite reach 5×10^{10} particles: its charge is $3.96 \times 10^{10} e$. Figure 3.4 gives the respective energies of the bunches of Fig. 3.3 (except for the $\theta_0 = 13^\circ$ case) as a function of angular position.

Table 3.1 gives a summary of the average energies (\bar{E}) and spectral qualities $[(E_{max} - E_{min})/\bar{E}]$ and the fractional standard deviation σ_E/\bar{E} for the cases shown in Figs. 3.3 and 3.4. The sixth example, shown also for $\theta_0 = 15.5^\circ$, is that of a truncated Gaussian fitted to the shape of the "ideal" $\theta_0 = 15.5^\circ$ case. It has a σ of 9° but is truncated at $\pm 7.5^\circ$. These results all compare extremely



OPTIMUM BUNCH SHAPES
FOR $\Delta E/E \rightarrow 0$

3-86

5061A3

Fig. 3.3. Bunch shape, i.e. particle distribution as a function of phase angle which leads to negligible spectrum width, for various values of θ_0 . The point marked "T" indicates where the integrated charge in the bunch reaches $5 \times 10^{10} e$.

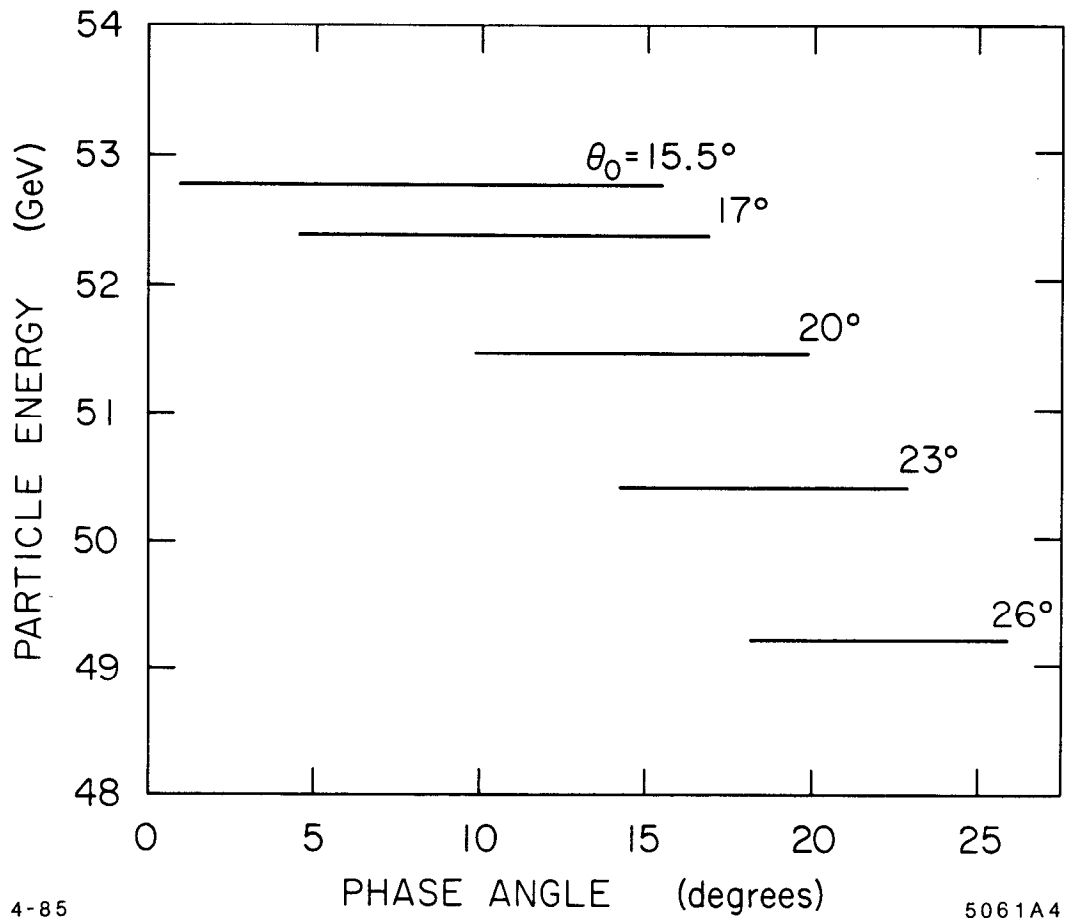


Fig. 3.4. Particle energy along bunches of Fig. 3.3 as a function of phase angle.

favorably with the energy spread σ_E/\bar{E} of 0.35% which one obtains for a Gaussian bunch of $5 \times 10^{10} e$ with a length 6σ , a σ of 4° and a θ_0 of 20° (the seventh example in Table 3.1), or for that matter, for the same bunch with charge reduced to $5 \times 10^8 e$. The energy spectra for all the above cases are illustrated in Fig. 3.5. Note that the examples of Table 3.1 are so narrow in energy that they can only be represented by a line.

Table 3.1. Calculated energy spectra
(all cases for 5×10^{10} particles).

θ_0 (degrees)	\bar{E} (GeV)	$(E_{max} - E_{min})/\bar{E}$ (%)	σ_E/\bar{E} (%)
26	49.210	0.008	0.003
23	50.399	0.009	0.003
20	51.450	0.010	0.003
17	52.360	0.014	0.004
15.5	52.755	0.010	0.004
Truncated Gaussian 15.5	52.809	0.14)	0.038
Gaussian (6σ) 20	52.795	3.500	0.352

3.3. DISCUSSION

If we rewrite Eq. (3.8) in terms of the gradient E_0 instead of the total energy V_0 , it becomes:

$$f(x) = \frac{E_0 d}{w(0)} \sin(\theta_0 - x) - \int_0^x \frac{\frac{\partial w}{\partial x}(x - \theta')}{w(0)} f(\theta') d\theta' \quad , \quad (3.9)$$

where d is the length of a single cavity. We see that for a structure with a given $w(\theta)$, once the gradient E_0 and the angular position θ_0 of the head are chosen,

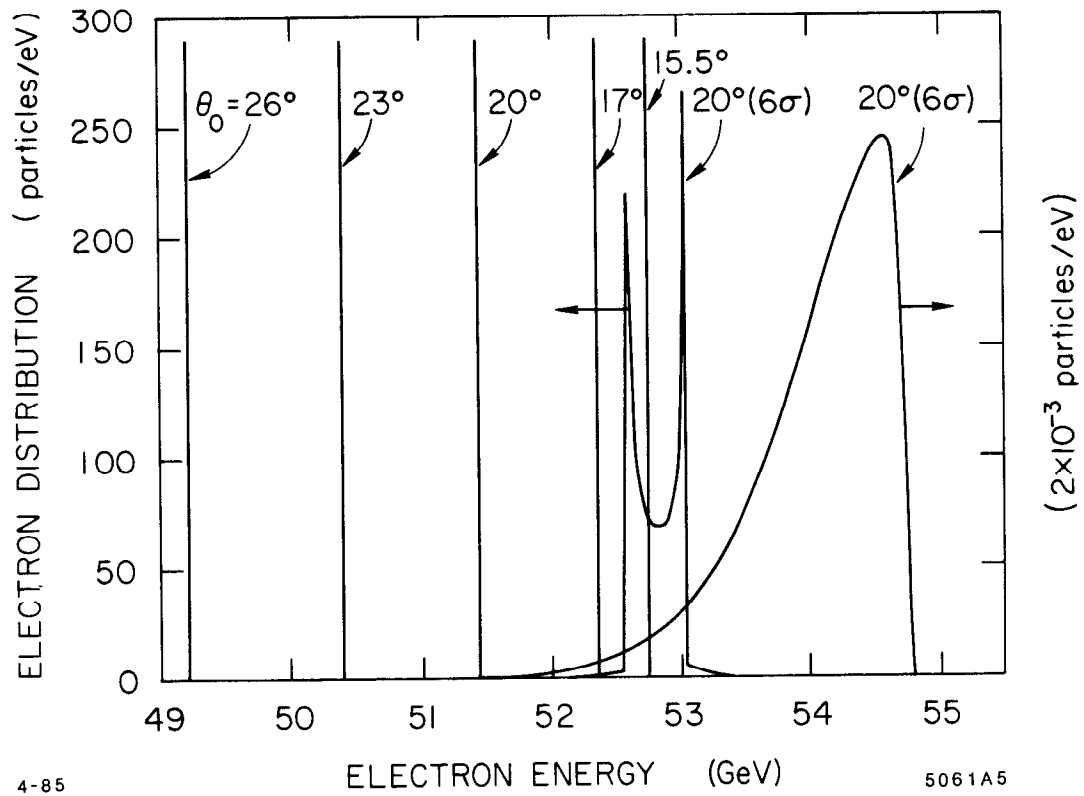


Fig. 3.5. Energy spectra for the examples of Table 3.1 with $5 \times 10^{10} e$ (left-hand scale) and for the Gaussian bunch with $5 \times 10^8 e$ (right-hand scale).

the shape is fixed by Eq. (3.9) and is independent of the total energy V_0 and length L . For a given gradient E_0 , $f(\theta)$ starts at a higher value as θ_0 is made larger since

$$f(0) = \frac{E_0 d}{w(0)} \sin \theta_0 \quad (3.10)$$

as shown in Fig. 3.3. Clearly, the more charge one wants, the higher gradient one needs, or the farther ahead of crest one must place the head.

3.4. TOLERANCES

To get a feeling for allowable tolerances, it is interesting to calculate the effect of changes in injection angle (θ_0) or bunch charge on \bar{E} and σ_E/\bar{E} , assuming constant bunch shape. Table 3.2 shows the effect of varying θ_0 while keeping the total charge of the bunch equal to $5 \times 10^{10} e$ in the case of the truncated Gaussian bunch discussed earlier.

Table 3.2. Truncated Gaussian bunch.

$$(\theta_{total} = 15^\circ, \quad \sigma = 9^\circ, \quad 5 \times 10^{10} e)$$

θ_0 (degrees)	\bar{E} (GeV)	$(E_{max} - E_{min})/\bar{E}$ (%)	σ_E/\bar{E} (%)
11.5	53.210	1.78	0.51
12.5	53.135	1.31	0.38
13.5	53.043	0.84	0.26
14.5	52.934	0.38	0.13
15.5	52.809	0.14	0.038
16.5	52.668	0.55	0.14
17.5	52.510	1.02	0.26
18.5	52.335	1.50	0.39
19.5	52.145	1.90	0.52

Table 3.3 shows the effect of changing the bunch charge while keeping its shape and θ_0 constant. The variations of σ_E/\bar{E} in both tables are close to hyperbolic.

Table 3.3. Truncated Gaussian bunch.

$$(\theta_{total} = 15^\circ, \quad \sigma = 9^\circ, \quad \theta_0 = 15.5^\circ)$$

Bunch Charge ($\times 10^{10} e$)	\bar{E} (GeV)	$(E_{max} - E_{min})/\bar{E}$ (%)	σ_E/\bar{E} (%)
3.0	53.314	1.52	0.43
3.5	53.187	1.12	0.33
4.0	53.061	0.81	0.23
4.5	52.935	0.45	0.12
5.0	52.809	0.14	0.038
5.5	52.683	0.27	0.10
6.0	52.557	0.64	0.21
6.5	52.431	1.00	0.31
7.0	52.305	1.36	0.42

3.5. CONCLUSIONS

We have shown that it is theoretically possible to find bunch shapes for the SLC which yield 5×10^{10} or more particles within negligible energy spread at the end of the linear accelerator. As it turns out, these shapes depend only on the linac energy gradient and the angle at which the head of the bunch is placed with respect to the accelerating wave, and are independent of the total energy or length of the accelerator. Excursions away from this angle in parts of the linac, designed to cause BNS damping of the transverse wake field effect, are of course permissible as long as overall "phase closure" to preserve the desired average θ_0 is accomplished. Some of these theoretical bunch shapes are not too different from shapes that ought to be realizable from injectors or damping rings. How to realize them exactly is not the subject of this work.

CHAPTER 4

THE TRANSIENT BEAM LOADING PROBLEM IN CONSTANT-GRADIENT LINEAR ACCELERATORS

Beam loading is defined as the energy reduction of charged particles due to their interaction with an accelerating structure. In Chapters 2 and 3, we used the summation of the wake fields produced by the particles to treat the problem of energy loss and energy spread for single bunches. In this chapter we will treat the multibunch beam loading problem by using the energy conservation law. We will start with the solution of the transient beam loading problem for a constant-gradient traveling-wave accelerator structure (SLAC-type structure). Then, the solution will be used to analyze the case of a bunch train which is injected into an accelerator section either before or after the section is filled entirely with energy. Finally, we will extend the results to discuss the energy compensation problem for multibunch operation of future linear colliders. To simplify the problem, we will assume that the RF pulse is an ideal step-function without dispersive effects and that the charged particles all travel with the speed of light.

4.1 GENERAL SOLUTION OF THE TRANSIENT BEAM LOADING PROBLEM FOR THE CONSTANT-GRADIENT STRUCTURE

In the absence of a beam, the steady-state variation of the RF power flow $P(z)$ along an accelerator structure is given by

$$\frac{dP(z)}{dz} = -2\alpha(z)P(z) \quad , \quad (4.1)$$

where $\alpha(z)$ is the attenuation coefficient of the structure. For the constant-gradient structure, $\alpha(z)$ is a slowly varying function along the structure. The attenuation constant for the entire section of length ℓ is

$$\tau = \int_0^{\ell} \alpha(z) dz \quad . \quad (4.2)$$

In the presence of an electron beam and taking into account time, the RF power loss per unit length is given by

$$\begin{aligned} \frac{dP}{dz} &= \left(\frac{dP}{dz} \right)_{wall} + \left(\frac{dP}{dz} \right)_{beam} \\ &= -2\alpha(z)P(z, t) - i(t)E(z, t) \quad , \end{aligned} \quad (4.3)$$

where $E(z, t)$ is the amplitude of the electric field at (z, t) on axis, the first term is the power dissipated in the structure walls, and the second term is the power absorbed by the beam. By seeking the total differential of $P(z, t)$ with respect to z , one obtains

$$\frac{dP(z, t)}{dz} = \frac{\partial P(z, t)}{\partial z} + \frac{\partial P(z, t)}{\partial t} \frac{dt}{dz} \quad . \quad (4.4)$$

In order to obtain the expression for dt/dz , let us study a disturbance at (z_1, t_1) , which travels with the group velocity v_g and arrives at z at time t :

$$t = t_1 + \int_{z_1}^z \frac{dz}{v_g(z)} \quad . \quad (4.5)$$

By differentiating, one gets

$$\frac{dt}{dz} = \frac{1}{v_g(z)} \quad , \quad (4.6)$$

and Eq. (4.3) then becomes:

$$\frac{\partial P(z, t)}{\partial z} + \frac{1}{v_g(z)} \frac{\partial P(z, t)}{\partial t} = -2\alpha(z)P(z, t) - i(t)E(z, t) \quad . \quad (4.7)$$

By using the relation $P = (E^2/2\alpha r)$ and assuming that the shunt impedance per unit length r does not change along the section, (4.7) becomes

$$\frac{\partial E(z, t)}{\partial z} + \frac{1}{v_g(z)} \frac{\partial E(z, t)}{\partial t} + \left[\alpha(z) - \frac{1}{2\alpha(z)} \frac{d\alpha}{dz} \right] E = -\alpha(z) r i(t) \quad . \quad (4.8)$$

Taking the Laplace transform with respect to time, we obtain

$$\frac{\partial E(z, s)}{\partial z} + \left[\frac{s}{v_g(z)} + \alpha(z) - \frac{1}{2\alpha(z)} \frac{d\alpha(z)}{dz} \right] E(z, s) = -r\alpha(z) i(s) \quad . \quad (4.9)$$

For the constant-gradient structure without beam, the attenuation coefficient can be derived from Eqs. (1.4) and (1.5) as:

$$\begin{aligned} \alpha(z) &= \frac{(P_{in} - P_{out})/2\ell}{P(z)} = \frac{(P_{in} - P_{out})/2\ell}{P_{in} - (P_{in} - P_{out})(z/\ell)} \\ &= \frac{(1 - e^{-2\tau})/2\ell}{1 - (1 - e^{-2\tau})(z/\ell)} \quad . \end{aligned} \quad (4.10)$$

Differentiating both sides of (4.10) with respect to z , one obtains:

$$\frac{d\alpha(z)}{dz} = \frac{(P_{in} - P_{out})/2\ell \cdot (P_{in} - P_{out})/\ell}{[P_{in} - (P_{in} - P_{out})z/\ell]^2} = 2\alpha^2(z) \quad . \quad (4.11)$$

By substituting (4.11) into (4.9) and integrating, we obtain

$$E(z, s) = E(0, s)e^{-st_z} - e^{-st_z} r i(s) \int_0^z e^{st_z} \alpha(z) dz \quad , \quad (4.12)$$

where t_z is the time it takes the RF power to propagate from 0 to z :

$$t_z = \int_0^z \frac{dz}{v_g(z)} = \int_0^z \frac{2Q\alpha(z)}{\omega} dz = -\frac{Q}{\omega} \ln \left[1 - (1 - e^{-2\tau}) z/\ell \right] \quad . \quad (4.13)$$

By using the substitution of variable

$$dt_z = \frac{1}{v_g(z)} dz = \frac{2Q\alpha(z)}{\omega} dz \quad , \quad (4.14)$$

and performing the integration in (4.12), one obtains:

$$E(z, s) = E(0, s)e^{-st_z} - \frac{\omega r i(s)}{2sQ} [1 - e^{-st_z}] \quad . \quad (4.15)$$

The energy gain of a synchronous electron ($v \approx c$) passing through the structure is given by

$$V(t) = \int_0^\ell E(z, t) dz \quad . \quad (4.16)$$

Correspondingly, its Laplace transform is

$$V(s) = \int_0^\ell E(z, s) dz \quad . \quad (4.17)$$

From (4.13) we have:

$$z = \frac{\ell}{(1 - e^{-2\tau})} \left[(1 - e^{-(\omega/Q)t_z}) \right] \quad , \quad (4.18)$$

$$dz = \frac{\omega \ell}{(1 - e^{-2\tau})Q} e^{-(\omega/Q)t_z} dt_z \quad . \quad (4.19)$$

By substituting $E(z, s)$ from (4.15) and dz from (4.19) into (4.17) and performing the integration, (4.17) becomes

$$V(s) = \frac{E(0, s)\omega \ell}{(1 - e^{-2\tau})(s + \omega/Q)Q} \left[1 - e^{-(s+\omega/Q)t_F} \right] - \frac{\omega r i(s)\ell}{2sQ(1 - e^{-2\tau})} \quad , \quad (4.20)$$

$$\left[\left[1 - e^{-(\omega/Q)t_F} \right] - \frac{\omega}{Q(s + \omega/Q)} \left[1 - e^{-(s+\omega/Q)t_F} \right] \right]$$

where $t_F = t_z(\ell) = 2\tau Q/\omega$ is the filling time of the section.

Now let us assume that $E(0, t)$ and $i(t)$ are step functions as follows:

$$\begin{cases} E(0, t) & = E_0 U(t) \\ i(t) & = i_0 U(t - t_i) \end{cases} \quad . \quad (4.21)$$

where t_i is the time when the beam is injected, i_0 is the average beam current, E_0 is the amplitude of the electric field at $z = 0$ and $U(t)$ is the unit step function.

If there are a total of N equally spaced bunches, each of charge q , and the bunch train has a time span t_b , the average current i_0 can be expressed as

$$i_0 = Nq/t_b \quad . \quad (4.22)$$

The Laplace transforms of (4.21) can then be written as

$$\begin{cases} E(0, s) = E_0/s \\ i(s) = (i_0/s) e^{-st_i} \end{cases} , \quad (4.23)$$

and (4.15) and (4.20) become

$$E(z, s) = \frac{E_0}{s} e^{-st_z} - \frac{\omega r i_0}{2Q} \left[\frac{e^{-st_i}}{s^2} - \frac{e^{-s(t_i+t_z)}}{s^2} \right] \quad (4.24)$$

$$\begin{aligned} V(s) = & \frac{E_0 \omega \ell}{(1 - e^{-2\tau})(s + \omega/Q)sQ} \left[1 - e^{-2\tau} \cdot e^{-st_F} \right] - \frac{\omega r i_0 e^{-st_i} \ell}{2Q s^2} \\ & \left[1 - \frac{\omega}{(1 - e^{-2\tau})(s + \omega/Q)Q} (1 - e^{-2\tau} \cdot e^{-st_F}) \right] \quad . \quad (4.25) \end{aligned}$$

The inverse transforms of (4.24) and (4.25) give respectively the electric field at any point and the energy gain as a function of time.

$$E(z, t) = E_0 U(t - t_z) - \frac{\omega r i_0}{2Q} \left[(t - t_i) U(t - t_i) + (t - t_i - t_z) U(t - t_i) \right] \quad (4.26)$$

$$\begin{aligned}
V(t) = & \frac{E_0 \ell [1 - e^{-(\omega/Q)t}]}{(1 - e^{-2\tau})} U(t) - \frac{E_0 \ell e^{-2\tau}}{(1 - e^{-2\tau})} \\
& \left[1 - e^{-(\omega/Q)(t-t_F)} \right] U(t - t_F) \\
& + \frac{r i_0}{2} \left\{ \frac{\omega \ell e^{-2\tau}}{Q(1 - e^{-2\tau})} (t - t_i) - \frac{\ell}{(1 - e^{-2\tau})} \right. \\
& \left. \left[1 - e^{-(\omega/Q)(t-t_i)} \right] \right\} U(t - t_i) \\
& - \frac{r i_0}{2} \left\{ \frac{\omega \ell e^{-2\tau}}{Q(1 - e^{-2\tau})} (t - t_i - t_F) - \frac{\ell e^{-2\tau}}{(1 - e^{-2\tau})} \right. \\
& \left. \left[1 - \frac{\omega}{Q}(t - t_i - t_F) \right] \right\} U(t - t_i - t_F) \quad .
\end{aligned} \tag{4.27}$$

Having obtained these general expressions, let us now apply them to some practical examples. The first example is for the case where the beam is injected exactly after one RF filling time. Most of the traveling-wave linear accelerators work in this mode. The second example is for the case where beam injection takes place before the RF structure is entirely filled up. The linear colliders accelerating multibunches will work in this mode.

4.2. BEAM INJECTION EXACTLY AFTER ONE FILLING TIME

In this case, for convenience we choose the time at which the beam is turned on as zero. The new time then starts after one filling time, t_F . Eq. (4.27) then becomes

$$\begin{cases} V(t) = E_0 \ell + \frac{r i_0}{2} \left[\frac{\omega \ell e^{-2\tau}}{Q(1 - e^{-2\tau})} t - \frac{\ell}{1 - e^{-2\tau}} (1 - e^{-\frac{\omega}{Q}t}) \right] & 0 \leq t \leq t_F \\ V(t) = E_0 \ell - \frac{r i_0 \ell}{2} \left[1 - \frac{2\tau e^{-2\tau}}{1 - e^{-2\tau}} \right] & t \geq t_F \end{cases} \tag{4.28}$$

where

$$E_0 \ell = (1 - e^{-2\tau})^{1/2} (P_{in} r \ell)^{1/2} \quad .$$

The energy gain $V(t)$ is schematically shown in Fig. (4.1). The transient beam loading for $0 \leq t \leq t_F$ can then be expressed as

$$\begin{aligned} \Delta V_b = V(t) - E_0 \ell &= -\frac{r i_0 \ell}{2(1 - e^{-2\tau})} \left[1 - \frac{\omega}{Q} e^{-2\tau t} - e^{-(\omega/Q)t} \right] \\ &= -\frac{r i_0 \ell}{2(1 - e^{-2\tau})} \left[1 - 2\tau e^{-2\tau} \left(\frac{t}{t_F} \right) - e^{-2\tau(t/t_F)} \right] . \end{aligned} \quad (4.29)$$

From this expression we can obtain some familiar results. First let us examine what happens at the very beginning of beam injection ($t \ll t_F$):

$$\left. \frac{d(\Delta V_b)}{dt} \right|_{t=0} = -\frac{i_0 r \omega \ell}{2Q} = 2k\ell \Delta q / \Delta t \Big|_{t=0} , \quad (4.30)$$

where k is the loss parameter per unit length for the fundamental mode. Eq. (4.30) is consistent with the result derived from the fundamental theorem of beam loading Eq. (2.2).

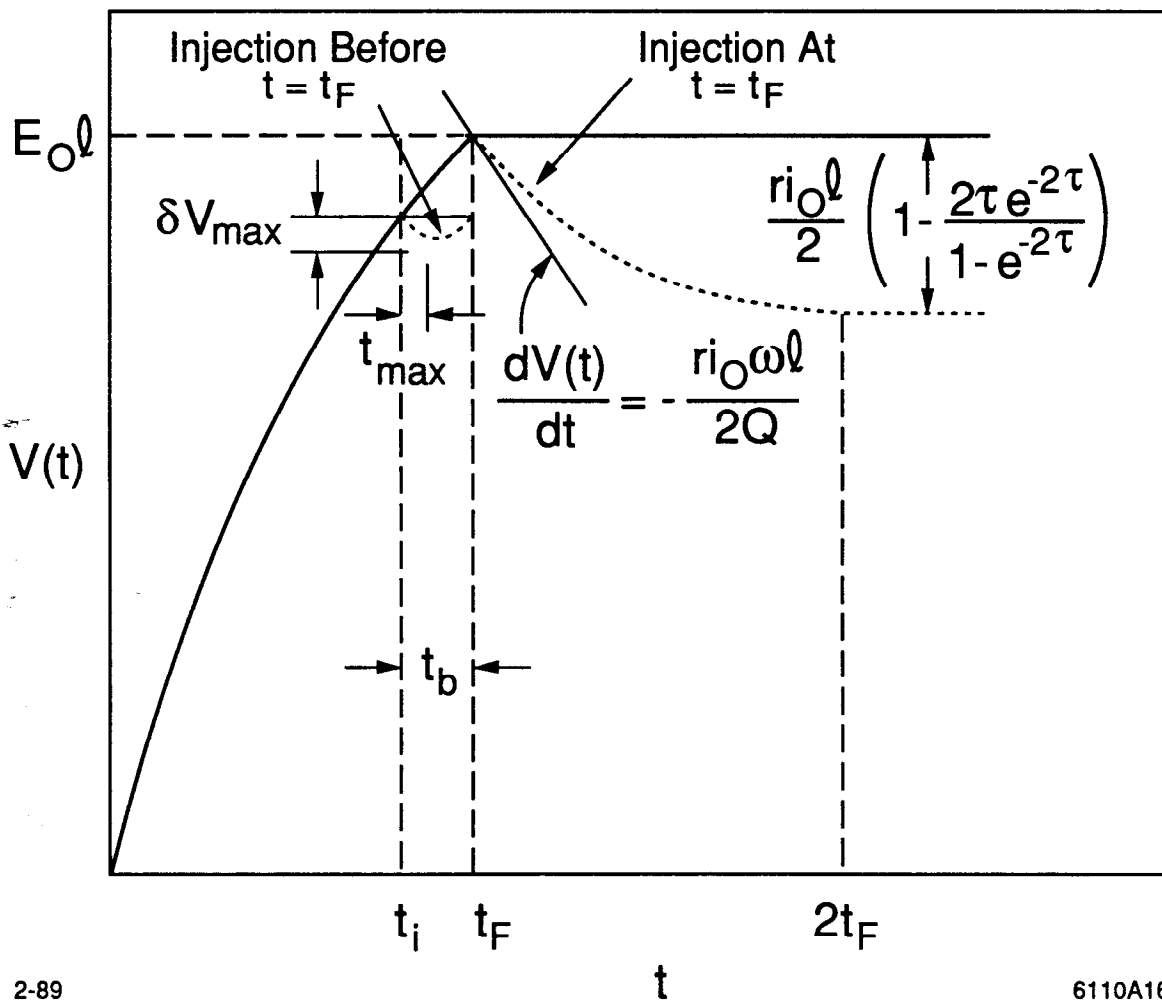
Conversely let us see what happens at time t_F after the beam has been turned on. From Eq. (4.29) it is easy to find that

$$\left. \frac{d(\Delta V_b)}{dt} \right|_{t=t_F} = 0 . \quad (4.31)$$

This corresponds to the transition from transient to steady-state beam loading when $t \geq t_F$. We can see that the transition is smooth.

4.3. EARLY BEAM INJECTION FOR MULTIBUNCH OPERATION

In order to increase the luminosity and RF energy transfer efficiency of a linear collider, multibunch operation will almost certainly be required. The beam should then be injected before the accelerator section is completely filled so that to first order, the energy decrease due to beam loading is compensated by the energy increase due to filling.



2-89

6110A16

Fig. 4.1. Transient beam loading shown schematically in arbitrary units for injection before $t = t_F$ and at $t = t_F$.

We assume in this example that the beam injection starts at time $t_i = t_F - t_b$ and ends at time t_F (see Fig. 4.1). To obtain the best energy compensation we choose to assume that the following condition must be satisfied:

$$V(t_i) = V(t_F) \quad . \quad (4.32)$$

From (4.27), this condition yields:

$$\frac{E_0 \left[1 - e^{-2\tau(1-t_b/t_F)} \right]}{1 - e^{-2\tau}} = E_0 + \frac{ri_0}{2} \left[\frac{2\tau e^{-2\tau} t_b}{1 - e^{-2\tau} t_F} - \frac{1 - e^{-2\tau t_b/t_F}}{1 - e^{-2\tau}} \right] \quad .$$

By assuming $t_b \ll t_F$ and expanding the exponential functions, we can write the condition for best energy compensation as

$$E_0 + \frac{ri_0}{2} \left[(1 - e^{2\tau}) + \tau \left(\frac{t_b}{t_F} \right) e^{2\tau} \right] = 0 \quad . \quad (4.33)$$

For best collider operation, it is important to know the energy deviation in a bunch train. Let $t = t_i + t^*$ in the time interval $t_i < t < t_F$. From (4.27) the energy gain at time t^* can be written as

$$\begin{aligned} V(t_i + t^*) &= \frac{E_0 \ell}{1 - e^{-2\tau}} \left[1 - e^{-(\omega/Q)(t_F - t_b + t^*)} \right] \\ &+ \frac{ri_0 \ell}{2(1 - e^{-2\tau})} \left[\frac{\omega e^{-2\tau}}{Q} t^* - \left[1 - e^{-(\omega/Q)t^*} \right] \right] \quad . \end{aligned}$$

Again, by expanding the exponential functions, the energy gain can be written as

$$\begin{aligned} V(t_i + t^*) &= \frac{E_0 \ell}{1 - e^{-2\tau}} \left[1 - e^{-2\tau} \left[1 + \frac{2\tau(t_b - t^*)}{t_F} \right] \right] \\ &+ \frac{ri_0 \ell}{2(1 - e^{-2\tau})} \left[\frac{\omega e^{-2\tau}}{Q} t^* - 2\tau \left(\frac{t^*}{t_F} \right) + 2\tau^2 \left(\frac{t^*}{t_F} \right)^2 \right] \quad . \quad (4.34) \end{aligned}$$

V_0 , the energy of the first bunch, can be obtained by letting $t_* = 0$ in Eq. (4.34):

$$V_0 = \frac{E_0 \ell}{1 - e^{-2\tau}} \left[1 - e^{-2\tau} \left[1 + 2\tau \left(\frac{t_b}{t_F} \right) \right] \right]. \quad (4.35)$$

From (4.34) and (4.35) the energy deviation from V_0 is

$$\begin{aligned} \delta V &= V(t_i + t^*) - V_0 \\ &= \frac{2E_0 \ell \tau e^{-2\tau}}{1 - e^{-2\tau}} \left(\frac{t^*}{t_F} \right) + r i_0 \ell \tau \left[-\frac{t^*}{t_F} + \frac{\tau}{1 - e^{-2\tau}} \left(\frac{t^*}{t_F} \right)^2 \right]. \end{aligned} \quad (4.36)$$

In order to find the time at which the energy is minimum, we set

$$\frac{d(\delta V)}{dt^*} = 0, \quad ,$$

which yields

$$t^* = \left(\frac{1 - e^{-2\tau}}{2\tau} - \frac{e^{-2\tau} E_0}{\tau r i_0} \right) t_F. \quad (4.37)$$

By using the condition for energy compensation (4.33), the maximum energy deviation happens at time t_{max} , which can be expressed as

$$t_{max} = \frac{t_b}{2}. \quad (4.38)$$

Under this condition where $t_b \ll t_F$, we see that the maximum energy sag is located at the center of the bunch train.

By substituting t_{max} in (4.38) into (4.36) and using (4.33) to simplify the result, the maximum energy deviation can be expressed as

$$\delta V_{max} = -r i_0 \ell \frac{\tau^2}{4(1 - e^{-2\tau})} \left(\frac{t_b}{t_F} \right)^2. \quad (4.39)$$

4.4. SOLUTIONS EXPRESSED IN TERMS OF MULTIBUNCH PARAMETERS

The charged particles accelerated in an RF linac are rigidly and regularly bunched. Let us assume that the N bunches are equally spaced, ΔS apart from each other. Then, we have the following relations:

$$i_0 t_b = Nq \quad , \quad (4.40)$$

$$N\Delta S = ct_b \quad , \quad (4.41)$$

$$\tau = \frac{\omega}{2Q} t_F = 2 \left(\frac{\omega r}{4Q} \right) \frac{t_F}{r} = \frac{2kt_F}{r} \quad . \quad (4.42)$$

By using the above relations, condition (4.33) can be rewritten as

$$E_0 + Nkqe^{2\tau} = kq \left(\frac{Nt_F}{t_b} \right) \left(\frac{e^{2\tau} - 1}{\tau} \right) \quad . \quad (4.43)$$

By using $t_b = \frac{\Delta S}{\ell} \left(\frac{N\ell}{c} \right)$ from Eq. (4.41), one obtains

$$\frac{\Delta S}{\ell} = \left(\frac{e^{2\tau} - 1}{\tau} \right) \left(\frac{ct_F}{\ell} \right) \frac{kq}{E_0 e^{-2\tau} + Nkq} \quad . \quad (4.44)$$

The n^{th} bunch which has the maximum energy sag can be calculated from (4.38):

$$n \approx \frac{N}{2} \quad . \quad (4.45)$$

The energy deviation of this bunch can be expressed as

$$\delta V_{max} = -\frac{\tau}{2(1 - e^{-2\tau})} \left(\frac{\ell}{ct_F} \right) N^2 kq \Delta S \quad . \quad (4.46)$$

For the case of small attenuation τ , the best energy compensation condition (4.44) becomes

$$\frac{\Delta S}{\ell} = \left(\frac{ct_F}{\ell} \right) \frac{2kq}{E_0 + Nkq} \quad . \quad (4.47)$$

From (4.44), the maximum energy sag is given by

$$\delta V_{max} = -\left(\frac{\ell}{ct_F}\right)\frac{N^2}{4}kq\Delta S \quad . \quad (4.48)$$

The condition of best energy compensation (4.47) and the maximum energy deviation (4.48) are similar to the results derived by R. Ruth²¹ from the analysis of the energy loss due to the wake field for the case of small attenuation τ .

Chapter 5

RF BREAKDOWN STUDIES IN ROOM TEMPERATURE ELECTRON LINAC STRUCTURES

5.1. MOTIVATION

This chapter concerns itself with the study of RF breakdown, field emission and RF processing in room temperature electron linac structures. The motivation behind this work was twofold: in a fundamental way, to contribute to the understanding of the RF breakdown phenomenon, and as an application, to determine the maximum electric field gradient that can be obtained and used safely in future e^\pm linear colliders approaching the TeV (10^{12} eV) energy range. Indeed, the accelerating gradient is one of the crucial parameters affecting their design, construction and cost. For a specified total energy, the gradient sets the accelerator length, and once the RF structure, frequency and pulse repetition rate are selected, it also determines the peak and average power consumption. These three quantities are at the heart of the ultimate realizability and cost of these accelerators.

For many years, the accelerator community has relied on the so-called Kilpatrick Criterion⁷ to predict RF breakdown limits of structures as a function of frequency. However, many experimenters have shown in the meantime that these limits can be greatly exceeded. The work reported here, carried out as part of a much broader linear collider research program at SLAC, attempts to establish the ultimate accelerating gradients that can be reached in practical structures at S-, C-, and X-band frequencies. Related topics which are also treated are field emission, RF processing, thermal effects, x-ray radiation, sparking, emission of gasses, surface damage and its possible control.

5.2 ACCELERATING STRUCTURES TESTED AND MAXIMUM GRADIENTS REACHED

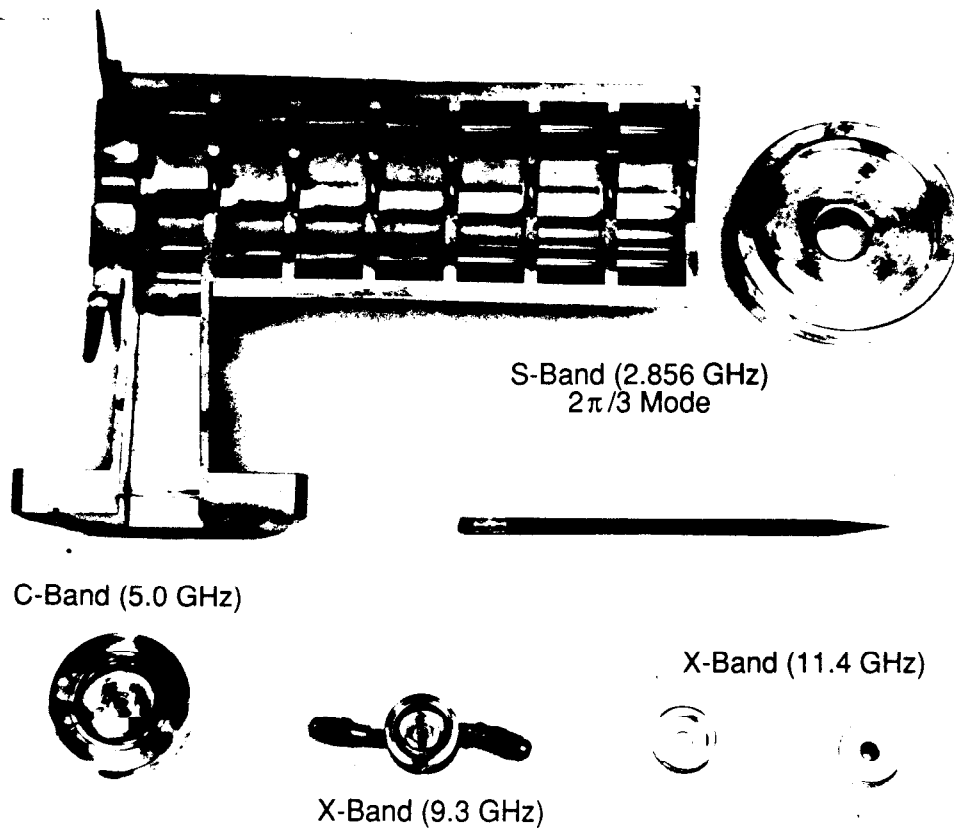
All experiments reported here, except for one that was started recently and is still incomplete, were performed on resonant standing-wave structures consisting of one or a few cavities. The use of such structures was made necessary by the present unavailability of the extremely high peak power sources that will eventually be required (500 to 1000 MW/m). The accelerating gradient in a short standing-wave section of length ℓ , shunt impedance per unit length r_{sw} , and peak input power P is given by

$$V = \sqrt{\frac{P}{\ell} r_{sw}} \quad , \quad (5.1)$$

whereas for a corresponding traveling-wave section, it is

$$V = \sqrt{2\tau \frac{P}{\ell} r_{tw}} \quad , \quad (5.2)$$

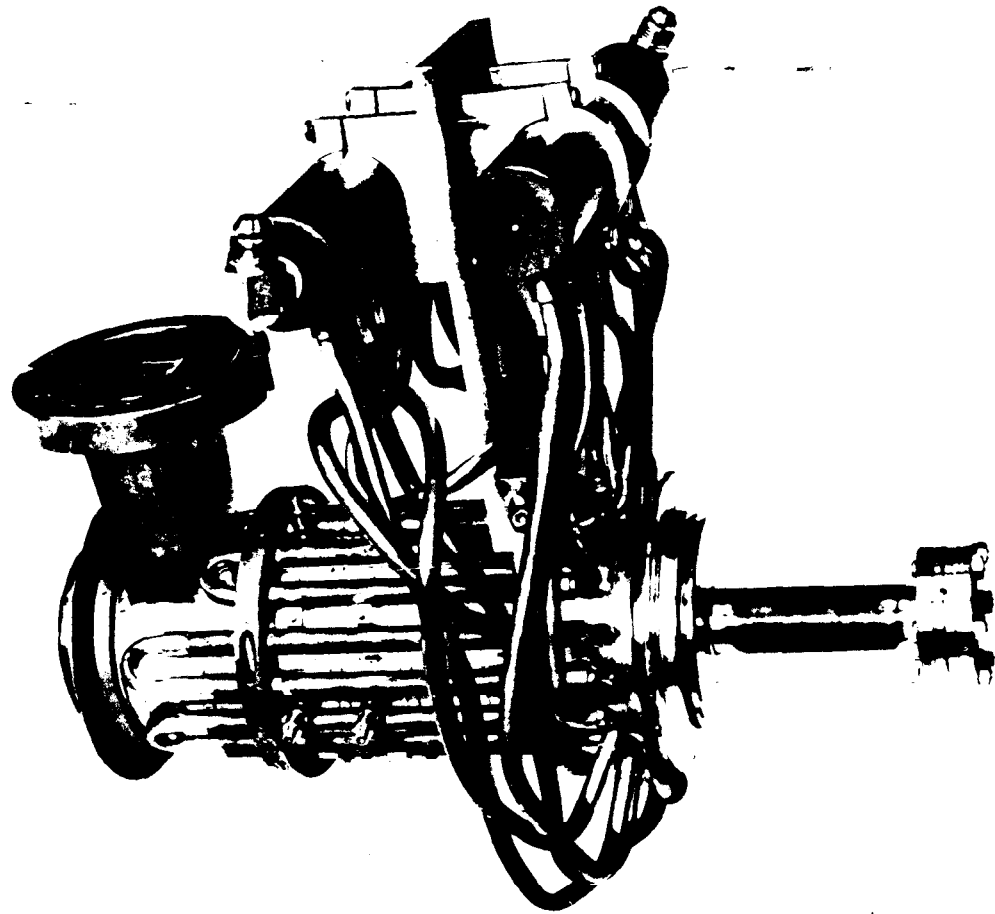
valid for $\tau \ll 1$, where τ , the attenuation of the section, is given by $\omega\ell/2v_gQ$ and r_{tw} , the traveling-wave shunt impedance, differs from r_{sw} by at most a factor of 2. It is in principle possible to increase τ for a short section of length ℓ by decreasing the group velocity v_g to raise the stored energy density (typically by reducing the size of the irises or by putting inductive slots in the disks). However, the structure would then not be entirely representative of the ultimate accelerator design as presently conceived. Standing-wave tests were done at S-, C- and X-band at SLAC^{22,23,24} and at Varian,^{25,26} and tests on a traveling-wave structure, also at X-band, were recently begun in connection with the relativistic klystron program²⁷ carried out by SLAC in collaboration with LBL and LLNL. The first series of S-band tests was done with a seven-cavity resonant section of SLAC $2\pi/3$ -mode constant-gradient structure. The structure can be seen in cross section in Fig. 5.1 and complete with its water cooling system in Fig. 5.2. It was supplied with RF from a 47 MW peak power XK-5 klystron with a 2.5 μ sec pulse width at



5-89

0110A49

Fig. 5.1. Collection of S-band (seven-cavity, $2\pi/3$ -mode), C-band and X-band cavities used in tests.



5-89

6110A48

Fig. 5.2. S-band (seven-cavity, $2\pi/3$ -mode) structure, complete with water cooling system.

60 pps. The second series of S-band tests was done with a specially built π -mode two-cavity structure with nose cones. Their presence increased the ratio of peak-to-accelerating field, thereby reducing the required peak power from the above klystron to about 10 MW. Such a structure, with one RF feed per wavelength, was proposed²⁸ to circumvent the need for extremely high peak power. It is shown in Fig. 5.3. The C- and X-band cavities are also shown in Fig. 5.1. To simplify the tests, only half-cavities were used in these cases. The experiments were carried out at Varian with ~ 1 MW magnetrons. Finally, preliminary tests have been done with a $2\pi/3$ -mode thirty-cavity traveling-wave structure at 11.424 GHz. Individual cavities can be seen in the lower right-hand corner of Fig. 5.1. Short (10 to 25 nsec) pulses of 60 to 200 MW peak power from a six cavity relativistic klystron were used to drive the section. The repetition rate, however, was only 1 pps, and no clearly measurable breakdown was reached as this thesis goes to press. In all cases, standing-wave and equivalent traveling-wave, accelerating and surface fields were calculated using the SUPERFISH computer program, as will be explained in Section 5.3.1. The results are summarized in Table 5.1.

All experimentally measured maximum gradients for standing-wave structures are summarized in Table 5.2 for pulse lengths as shown. For the S-band tests, increasing the pulse length from 1.5 to 2.5 μsec caused only a 2% reduction in the maximum attainable gradient. The peak surface electric fields are plotted as a function of frequency in Fig. 5.4. A rough fit to this curve is

$$E_s \sim 195 [f(\text{GHz})]^{1/2} \quad (5.3)$$

We see that if this empirical relationship is valid at the higher frequencies such as four times SLAC (11.424 GHz) or six times SLAC (17.136 GHz) which are presently being considered for a future linear collider, we could expect the breakdown limits shown in Table 5.3.



5-89

6110A47

Fig. 5.3. S-band (two-cavity, π -mode) structure, complete with water cooling system.

Table 5.1. Fields calculated for normalizing condition[†]
 $|\int_0^L E_z(z) \exp\{j(\omega z/c)\} dz|/L = 1 \text{ MV/m.}$

	S-band		C-band Half-cavity*	X-band	
	Disk-loaded ($2\pi/3$ -mode)	With nose cone (π -mode)		Half-cavity*	Disk-loaded ($2\pi/3$ -mode)
Frequency, f (MHz)	2856.1	2856.38	4998.0	9346.5	11423.7
Length for calculation, L (cm)	5.2485	5.2485	1.507	0.806	1.3121
Beam hole diameter, $2a$ (cm)	1.99	1.6	0.748	0.40	0.75
Factor of merit, Q	13,803	18,489	7018	5595	6960
Shunt impedance [◇] ($M\Omega/m$)	62.6/2	74.2	79.6	88.83	98.0/2
Energy stored in cavity of length L , W (J)	1.2445×10^{-3}	7.254×10^{-4}	3.951×10^{-5}	7.205×10^{-5}	2.5415×10^{-5}
Power dissipated, $P_D = \omega W/Q$ (W)	1611.8	704.12	176.8	75.26	262.07
Average accelerating field, \bar{E}_{acc} [‡] (MV/m)	0.9824	0.9977	0.966	0.9087	0.9893
Maximum axial field at $z = 0$, $ E_{z,SW} _{max}$ (MV/m)	2.685	1.8655	3.1683	2.0212	1.616
Maximum surface field, $ E_{s,SW} _{max}$ (MV/m)	3.81	4.145	7.542	4.876	4.502
$ E_{z,SW} _{max} / \bar{E}_{acc}$	2.733	1.87	3.28	2.224	1.633
$ E_{s,SW} _{max} / \bar{E}_{acc}$	3.88	4.15	7.81	5.37	4.55

[†] The SUPERFISH program calculates all the field and energy properties for the indicated normalizing condition.

*For half-cavities with end-plate, r and Q are lower than they would be for a full cavity.

[◇] Shunt impedances given here are for SW case. Conversely, if the S-band $2\pi/3$ -mode section is used as a TW structure, the shunt impedance is twice as high, i.e. 62.6 $M\Omega/m$.

[‡] \bar{E}_{acc} is slightly lower than 1MV/m because it is the real or imaginary part of the normalizing integral, depending on the boundary conditions (see section 5.3.1).

Table 5.2. Experimentally obtained breakdown-limited gradients.

	S-band		C-band Half-cavity	X-band	
	Disk-loaded ($2\pi/3$ -mode)	With nose cone (π -mode)		Half-cavity	Disk-loaded ($2\pi/3$ -mode)
Frequency, f (MHz)	2856	2858	4998	9303	11424
Total length (cm)	24.5	10.5	1.507	0.806	26.25
Filling time* (μs)	0.77	1.0	0.172	0.082	0.028
Pulse length (μs)	1.5-2.5	1.5-2.5	3.5	3.8	0.025 [†]
Peak power input (MW)	47	10.8	0.8	1.2	200 [†]
Peak surface field, E_s (MV/m)	313	340	445	572	303 [†]
Corresponding traveling-wave accelerating field [‡]	161	175	229	295	133 [†]

*For critical coupling in the case of standing-wave structures.

[†]Preliminary results, limited by available RF power and not by breakdown.

[‡]Assuming SLAC structure, working in the traveling-wave mode, in which $E_s/\bar{E}_{acc} = 1.94$, except for X-band disk-loaded TW structure which was built with $E_s/\bar{E}_{acc} = 2.28$.

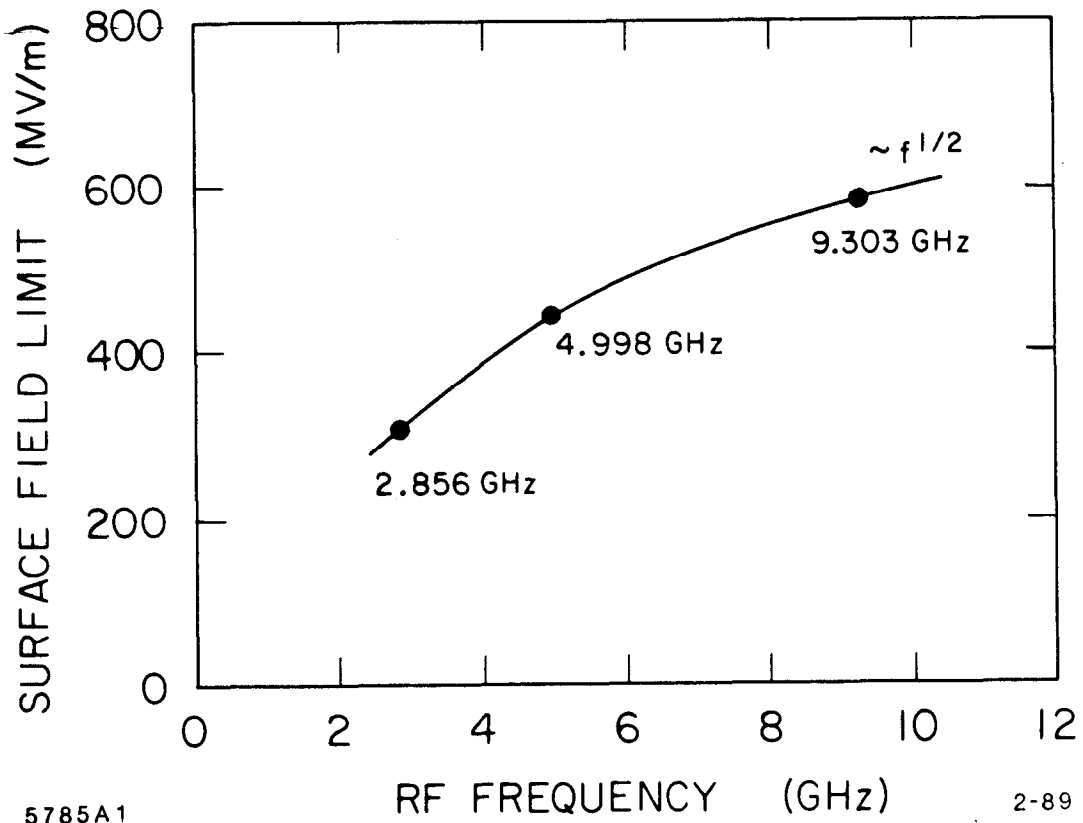


Fig. 5.4. Peak breakdown surface fields measured as a function of frequency.

Table 5.3. Predicted limiting gradients for future colliders at specific frequencies.

Extrapolated Limiting Gradients	11.424 GHz	17.136 GHz
Peak Surface Field (MV/m)	660	807
Accelerating Field (MV/m) assuming $E_s/\bar{E}_{acc} = 2.5$	264	323

In this table it is assumed that the iris diameter ($2a$) of the disk-loaded waveguide is chosen to be relatively large ($2a/\lambda \approx 0.2$) so that the longitudinal and transverse wake fields can be minimized. This results in a ratio of peak surface field to average accelerating field of 2.5. Also, the possible advantage of going to much shorter pulse lengths (20 – 100 nsec) at the higher frequencies and conversely, the disadvantage of having to incorporate lossy radial slots in the disks to damp higher order modes, are neglected or assumed to cancel each other.

We will now discuss the details of the experimental conditions under which the above results were obtained.

5.3. STRUCTURE DESIGN, EXPERIMENTAL SET-UPS AND TESTS PERFORMED

5.3.1. S-Band Disk-loaded Waveguide Structure

Design Principles

The accelerating gradient at which the SLAC disk-loaded waveguide runs routinely for the SLC is about 20 MV/m. The highest accelerating gradient ever measured until 1984 at SLAC dates back to undocumented experience with a short accelerator section in a resonant ring used to test RF components during the construction period (1962-1966) of the linear accelerator. It is believed that at that time, this short section reached an accelerating gradient of 46 MeV/m without obvious signs of breakdown.

— To reach 100 MV/m in a conventional SLAC three-meter constant-gradient section, one would need a klystron with a peak power output of 900 MW. Since

such a tube is not available, we decided to use a short standing-wave section in which the resonant fields build up. The design criteria for this section, the fabrication, the matching and tuning, the experimental set-up and the results are described below.

Standing-wave accelerators are generally built in the π -mode or some variation thereof so that both forward and reflected waves contribute to the acceleration of a synchronous particle. In the case of this experiment, however, we were not interested in accelerating electrons but rather, in testing a $2\pi/3$ -mode SLAC-type of section to its maximum field. We took advantage of the availability of short six-cavity stacks, already brazed onto a coupler, to speed up the experiment (see Fig. 5.1). These stacks were actually the input and output segments of the SLAC three-meter sections which consist of a total of 84 regular cavities and two coupler cavities. These stacks were brazed separately and then joined onto the center portion (74 cavities). We chose the output stack because it has a lower group velocity and a higher field intensity for a given power input, and we capped it off at the end opposite to the coupler to make it resonant. Thus our standing-wave section consisted of seven cavities.

The conceptual passage from standing waves to traveling waves and vice versa can be understood by referring to Fig. 5.5 and Ref. 29. The traveling-wave E_z field for the accelerating TM_{01} -type mode can be expressed as

$$E_{z,TW} = \sum_{n=-\infty}^{n=+\infty} a_n J_0(k_{rn}r) e^{-j(\omega t - \beta_n z)} \quad (5.4)$$

where

$$\beta_n = \beta_0 + 2\pi n/d$$

$$\beta_0 = \omega/c$$

$$d = \text{periodic length}$$

$$a_n = \text{amplitude of } n^{\text{th}} \text{ space harmonic}$$

$$k_{rn}^2 = (\omega/c)^2 - \beta_n^2$$

The standing wave can be viewed as the sum of two traveling waves, one traveling to the right ($e^{+j\beta z}$), the other to the left ($e^{-j\beta z}$). For a particle traveling to the right on crest at the velocity of light, the first wave alone produces acceleration. As stated above, because of the periodic nature of the structure, the fields are actually made up of summations of space harmonics of amplitude a_n of which only the first (a_0) travels at the velocity of light. If we choose the origin at a point of symmetry of the structure (in the middle of a cavity or a disk) and set proper boundary conditions, the expression for the axial SW electric field is simplified. For example, if we let the tangential component of the electric field be zero at both end-planes, this results in the so-called Neuman boundaries shown on the left-hand side of Fig. 5.5 (b) and the axial SW electric field can be expressed as

$$E_{z, SW} = e^{-j\omega t} \sum_{n=-\infty}^{n=+\infty} 2a_n \cos \beta_n z. \quad (5.5)$$

Conversely, if we let the tangential component of the magnetic field be zero at both end-planes, this results in the so-called Dirichlet boundaries shown on the right-hand side of Fig. 5.5(b) and the axial SW electric field can be expressed as

$$E_{z, SW} = e^{-j\omega t} \sum_{n=-\infty}^{n=+\infty} 2a_n \sin \beta_n z. \quad (5.6)$$

The snapshots of E_z and E_r at the instants chosen in Fig. 5.5(a) and 5.5(b) are indistinguishable, except that in the standing-wave case the E_z (or E_r) and H_ϕ are in time quadrature. This is the only basic physical difference between a TW structure and its simulation by a SW test. We did not feel that this difference was sufficient to invalidate the tests, even though the trajectories of field-emitted electrons would clearly be different in the two cases.

To calculate the field parameters in our standing-wave section, we used the **SUPERFISH** program for cavity No. 79 of the constant-gradient stack. Since the

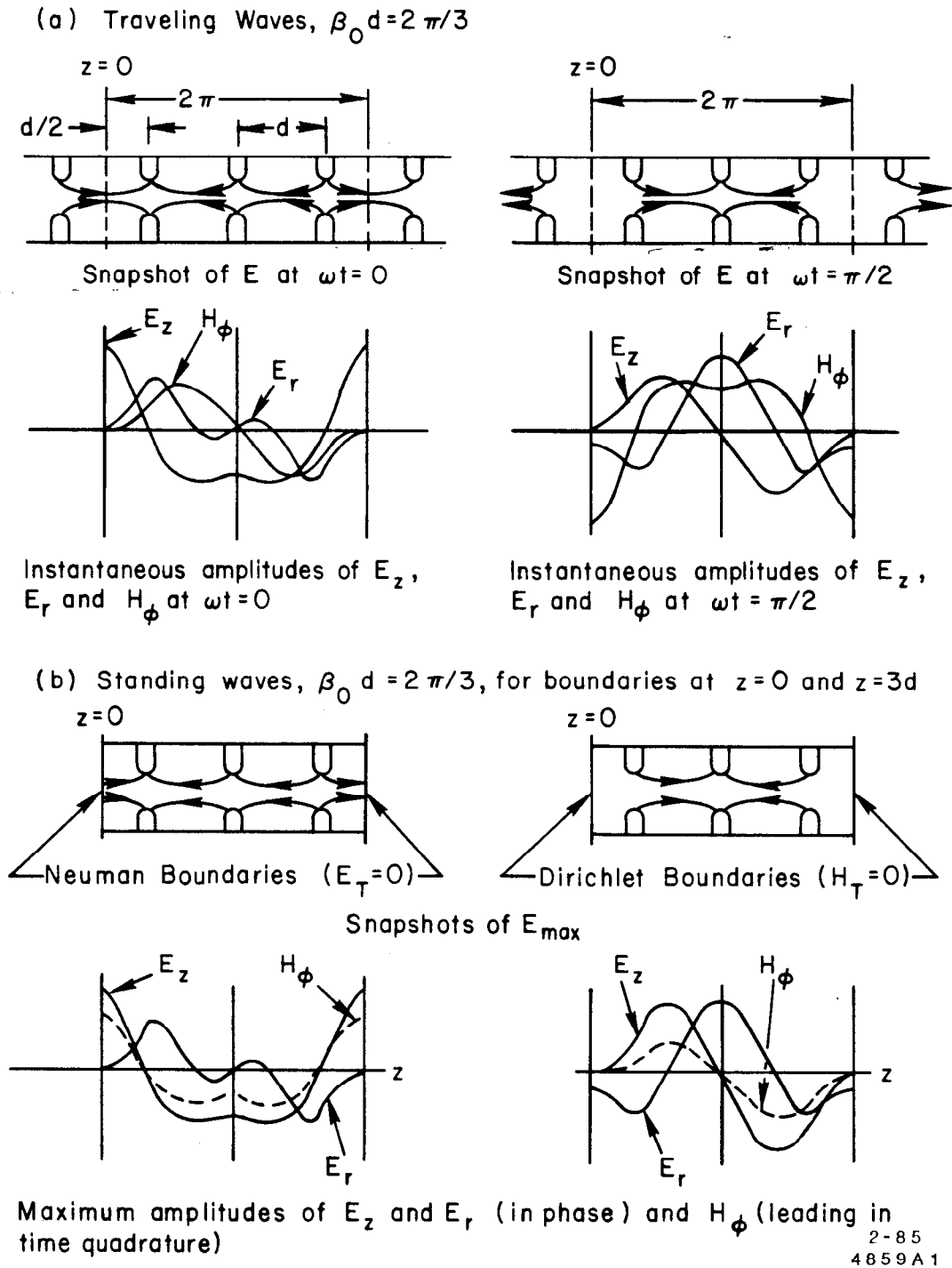


Fig. 5.5. Traveling waves and standing waves in the SLAC structure with their respective field amplitudes in arbitrary units. Note that E_z is taken on-axis and E_r and H_ϕ are off-axis.

other cavities (No. 80 through No. 85) have slightly higher fields, this calculation is on the conservative side. The calculation was performed for Neuman-Neuman boundaries for one and one-half cavity ($L = 5.25$ cm) with the normalizing condition given in the SUPERFISH program as

$$\left| \int_0^L E_z(z) e^{j(\omega z/c)} dz \right| = 1 \text{ MV/m.} \quad (5.7)$$

If the SW field is maximum at the $z = 0$ boundary of the section under calculation, the average accelerating field can be expressed as

$$\bar{E}_{acc} = \frac{1}{L} \int_0^L E_z(z) \cos(\omega z/c) dz.$$

Conversely, if the SW field is zero at the $z = 0$ boundary of the section under calculation, the average accelerating field can be expressed as

$$\bar{E}_{acc} = \frac{1}{L} \int_0^L E_z(z) \sin(\omega z/c) dz.$$

For this reason, \bar{E}_{acc} in Table 5.1 is always slightly lower than 1 MV/m.

Also, referring back to Table 5.1, the shunt impedance for the standing wave is half of that for the traveling wave (except in the π -mode) because twice the energy is stored for the same accelerating field. Conversely, it should be noticed that the ratio of maximum surface electric field to average accelerating field for the standing-wave structure is twice that for the traveling-wave case, i.e.

$$|E_{s,SW}|_{max} / \bar{E}_{acc} = 2 |E_{s,TW}|_{max} / \bar{E}_{acc} \quad (5.8)$$

From this expression we see, for example, that for a SW structure consisting of $2\pi/3$ -mode cavities, an average accelerating field of 50 MV/m results in the same peak surface field (in one out of three cavities, i.e., the half-cavities on the left-hand side of Fig. 5.5(b)) as would exist, at successive times ($T/3$ apart), in

all cavities of a $2\pi/3$ -mode TW structure with an average accelerating field of 100 MV/m. Since in our breakdown tests the physically limiting field is the peak surface field, we must obtain a relationship between the input power (P_{in}) to the SW structure and this field. This can be done by using Table 5.1 and noting that in a SW cavity, at steady-state, $P_{in} = P_D$. Our $2\pi/3$ -mode section having an equivalent length of 6.34 cavities and a measured Q value of ~ 13500 , we can derive the following relationships:

$$\begin{aligned} E_{s, SW} &= 3.88 \times 0.9824 \sqrt{\frac{P_{in} \times 13500}{1611.8 \times (6.34/1.5) \times 13803 \times 10^{-6}}} \\ &= 45.7 \sqrt{P_{in}} \quad \text{MV/m} \end{aligned} \quad (5.9)$$

and thus

$$\bar{E}_{acc, TW} = 23.56 \sqrt{P_{in}} \quad \text{MV/m} \quad (5.10)$$

where P_{in} is in MW. The results are found in Table 5.2.

Fabrication, Matching and Tuning

Several mechanical modifications were made to complete the fabrication of the standing-wave section from the available coupler stack. The first was to braze sixteen (instead of the usual eight) cooling tubes around the section to improve the cooling. The second modification was to drill small holes (by EDM) into the wall and disks of the section (see Fig. 5.6) to insert thermocouples for temperature monitoring at test points 1-4. Test point 1 is used to monitor the temperature of the end-plate. The holes at test points 2 and 3 are deep enough to measure the temperatures of the edges of the disks. Test point 4 is located in a shallow hole in the wall to measure the average temperature of the whole section. The third modification was to cap off the last cylinder (cavity No. 79) with a cut-off disk, and a subsequent plate to provide a vacuum seal. The fourth modification was to braze an extra matching iris into the input coupler to critically couple the section for maximum power delivery. The iris is shown schematically in Fig. 5.7.

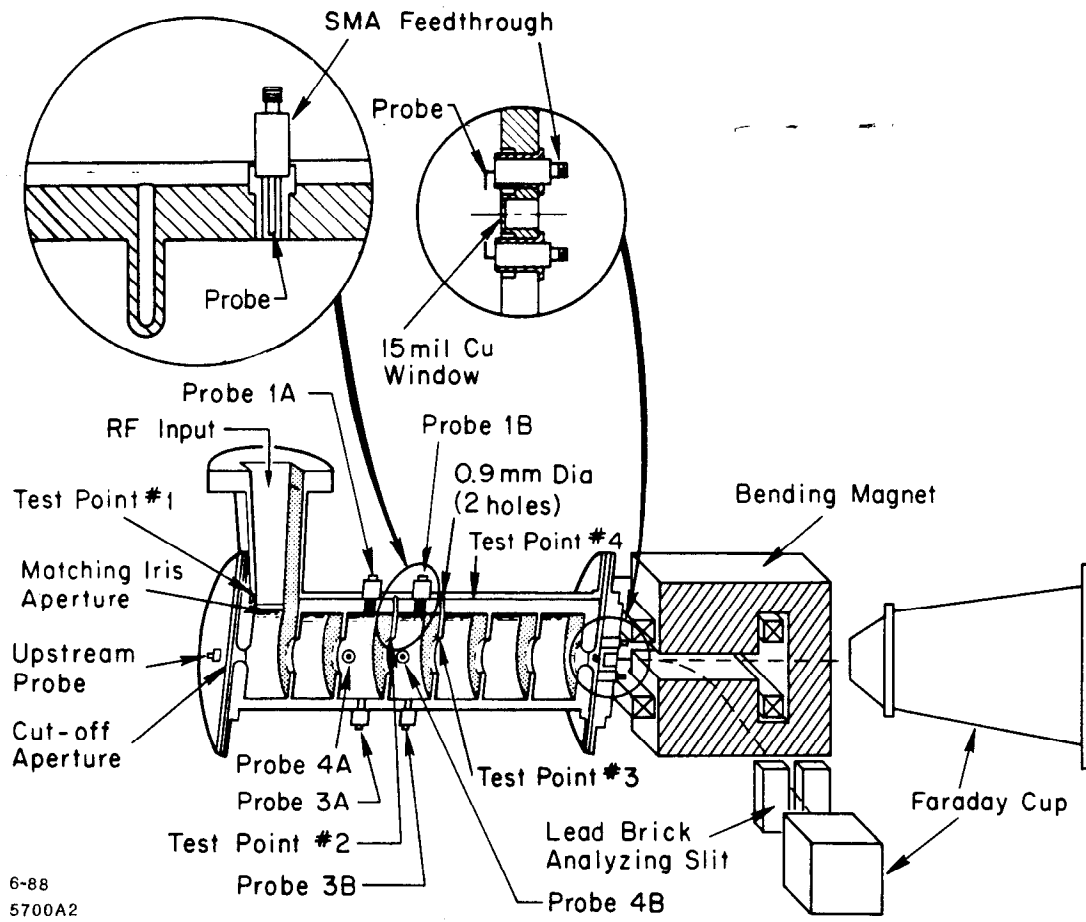


Fig. 5.6. Experimental set-up used for S-band (seven-cavity, $2\pi/3$ -mode) structure.

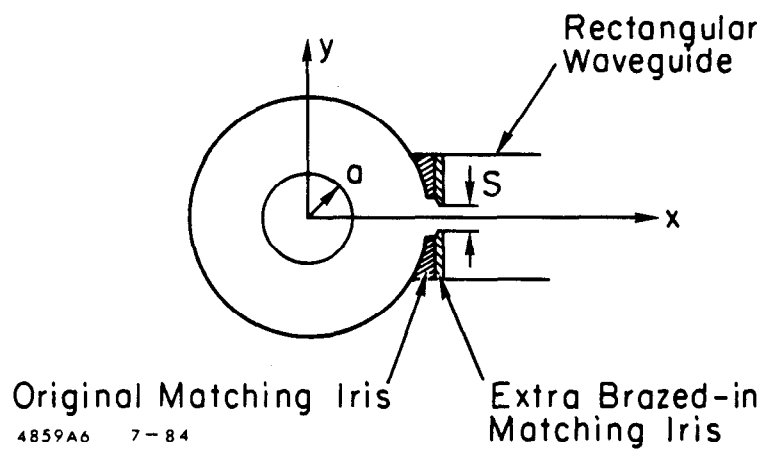


Fig. 5.7. Cross-section of coupler cavity showing extra brazed-in matching iris to obtain critical coupling.

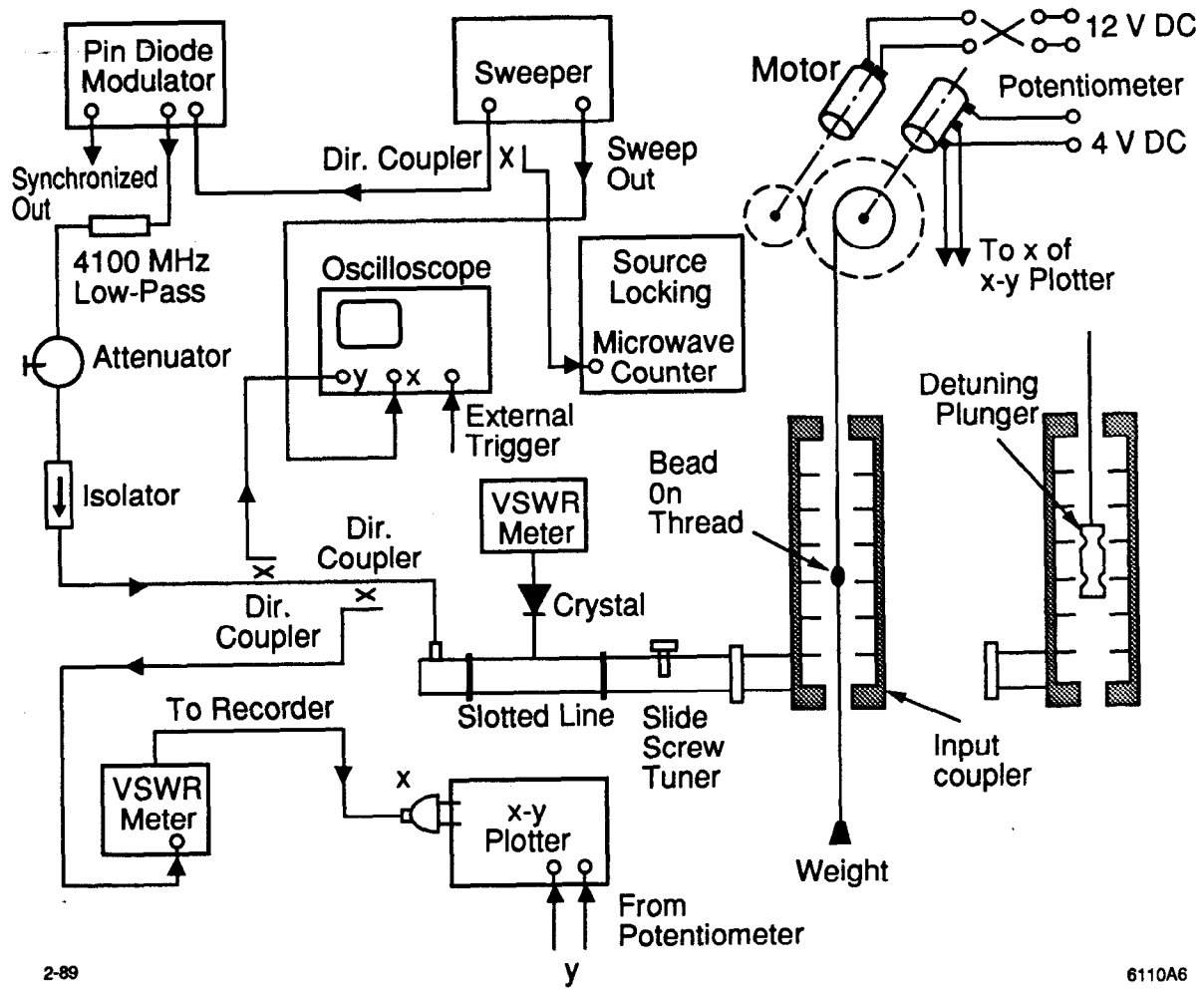
The end-plates were originally made out of stainless steel. However, in one of the early experiments an RF-focused field-emitted (FE) beam punctured the downstream plate. After this incident the stainless steel plates were replaced by 1.25 cm thick copper plates, thinned down on axis to 0.38 mm thick, 1.4 cm diameter “windows” to permit extraction and analysis of the FE beam. Two internal probes with coaxial SMA feedthroughs were installed at both ends to monitor and measure internal FE currents. Subsequently, eight transverse coaxial SMA probes were installed (3A, 4A, etc. in the full-field cavity A, and 3B, 4B, etc. in the half-field cavity B), also to measure FE currents, but this time to detect any azimuthal asymmetries in emission.

The process of tuning consisted of adjusting the phase shift of every cavity to the $2\pi/3$ design value at the correct temperature and pressure. The process of matching consisted of adjusting the coupling between the input rectangular waveguide and the section to obtain the lowest possible standing-wave ratio. Because the two processes are not independent, the Kyhl nodal shift method³⁰ was adopted. The experimental arrangement for tuning, matching and measuring of the electric field on-axis is illustrated in Fig. 5.8. For the nodal shift measurement, a detuning copper plunger was inserted into a given cavity as shown on the right-hand side of Fig. 5.8. For the field measurement, a dielectric bead was then pulled along the axis of the section, also as shown. The signal reflected by the bead was connected to an X-Y plotter via an VSWR meter: the resulting plot is shown in Fig. 5.9. Note that cavities No. 80 and No. 83 are the ones that reach the maximum field; the coupler and other cavities do not.

By adjusting the iris aperture S , a VSWR Γ of 1.08 was obtained for $S = 0.78$ in. Thus, the reflection coefficient ρ of the section was

$$\rho = \frac{\Gamma - 1}{\Gamma + 1} = 0.0385 \quad (5.11)$$

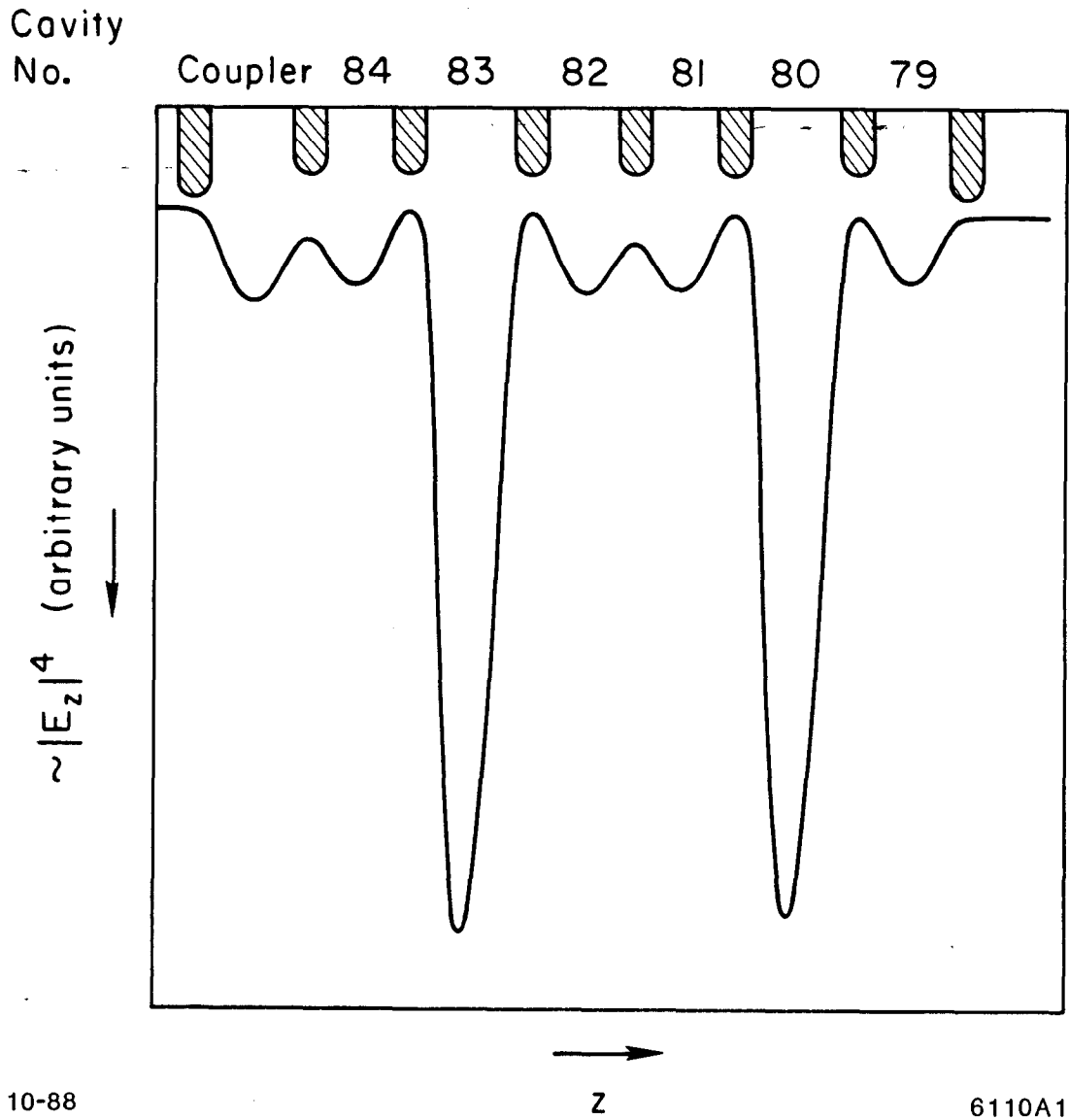
Thus, once steady-state was reached, only 0.15% of the input power was reflected.



2-89

6110A6

Fig. 5.8. The microwave measurement set-ups for matching, tuning and bead-pulling.



10-88

z

6110A1

Fig. 5.9. Power reflected by bead as a function of axial position (in arbitrary units). This power, if it were measured with a perfect square-law crystal, would be proportional to $|E_z|^4$ because the reflection coefficient of the bead is proportional to $|E_z|^2$ and the reflected power scales as the square of the reflection coefficient.

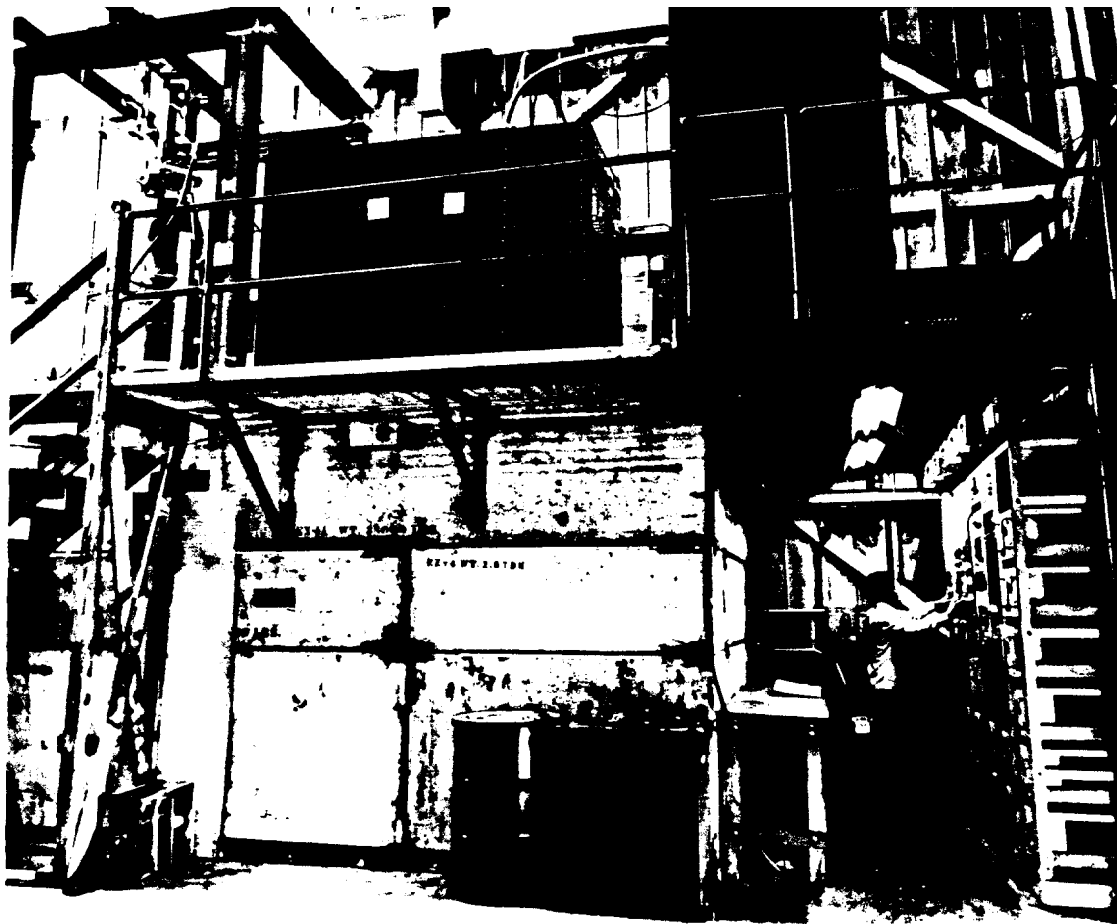
When holes were machined into the wall of the section and the eight transverse probes were brazed into them, several cavities were deformed. In the process, the original tuning and matching were spoiled and the entire procedure had to be redone.

Experimental Set-up

During the course of this research, the experimental set-up for the high power tests was gradually modified to refine the measurements and allow different observations. A general RF block diagram is shown in Fig. 5.10. The RF system consisted of a low-level variable frequency oscillator, a pin-diode modulator, two traveling-wave amplifiers, and an XK-5 klystron which supplied up to about 47 MW of peak power to the accelerator section. The variable frequency oscillator was needed because the temperature of the section changed as the input power was increased, and the oscillator had to be retuned to keep the section resonant. The trigger system was used to vary the repetition rate and the pin diode allowed us to adjust the length of the RF pulse. The forward and reflected powers were monitored by means of two modified Bethe-hole couplers.

All the tests were done inside a concrete vault in the SLAC Cryogenics Building. Fig. 5.11 shows a view inside the building. This vault consists of three-foot thick shielding blocks and a complete radiation safety interlock system. The klystron, modulator and power supply are located on the roof of the vault and the microwave power is piped to the accelerator structure via a vertical rectangular waveguide whose vacuum is separated from the structure vacuum by a ceramic window.

When the accelerated and axially extracted FE currents became measurable, a bending magnet, momentum analyzing slit and Faraday cups were added at the down-stream end (on the right in Fig. 5.6.). Later, this equipment and the downstream copper window were removed and a glass window, mirror and black-and-white video camera were installed in the shielding vault to look inside the section during high-gradient operation. An attempt was also made to use two



12-88

6110A13

Fig. 5.11. Overall view of experimental set-up for S-band test.

color video cameras, but neither could be operated successfully, the first one because it was affected by x-ray radiation, and the second because of insufficient sensitivity. Dipole magnets were wrapped around the section and/or along an axial output pipe, to prevent FE electrons from melting the glass window. The effect of these magnets was to bend the electrons into the walls, but—in the process—to generate additional x-rays which produced a strong luminescent background glow as they passed through the glass window.

High Power Tests

The peak power dissipated per unit length in the $2\pi/3$ -mode structure was more than twenty times higher than in the SLAC linac running in the SLC mode. For this reason, it was important to check the behavior of the section under the effect of RF heating. For our test, the cooling water flow was set at 15 gpm and the input water temperature was 83° F.

Figure 5.12 shows the temperatures monitored in the section as a function of average power dissipated. All variations appear to be linear. As pointed out earlier, test points 2 and 3 are in successive disks, and test point 4 is in the outer wall. As we see, test point 2 rose much faster than test point 3. This can be explained by noticing that the magnetic fields near the edges of different disks are different, as shown in Fig. 5.5(b). Figure 5.12 also shows the resonant frequency of the section as a function of average power dissipated. The linear variations, repeatable from measurement to measurement, indicated that the deformations of the section caused by heat in this range are not permanent.

It should be mentioned that the average powers plotted in Fig. 5.12 were indeed the powers delivered to the section, after subtraction of the reflected power from the forward power measured by the directional couplers in Fig. 5.10. The ratios of reflected-to-forward energy or average power for a critically coupled cavity can be expressed as³¹

$$-\quad \frac{\bar{P}_{ref}}{\bar{P}_{for}} = \frac{T_C}{T_P} \left(1 - \frac{1}{2} e^{-2T_P/T_C} \right) \quad , \quad (5.12)$$

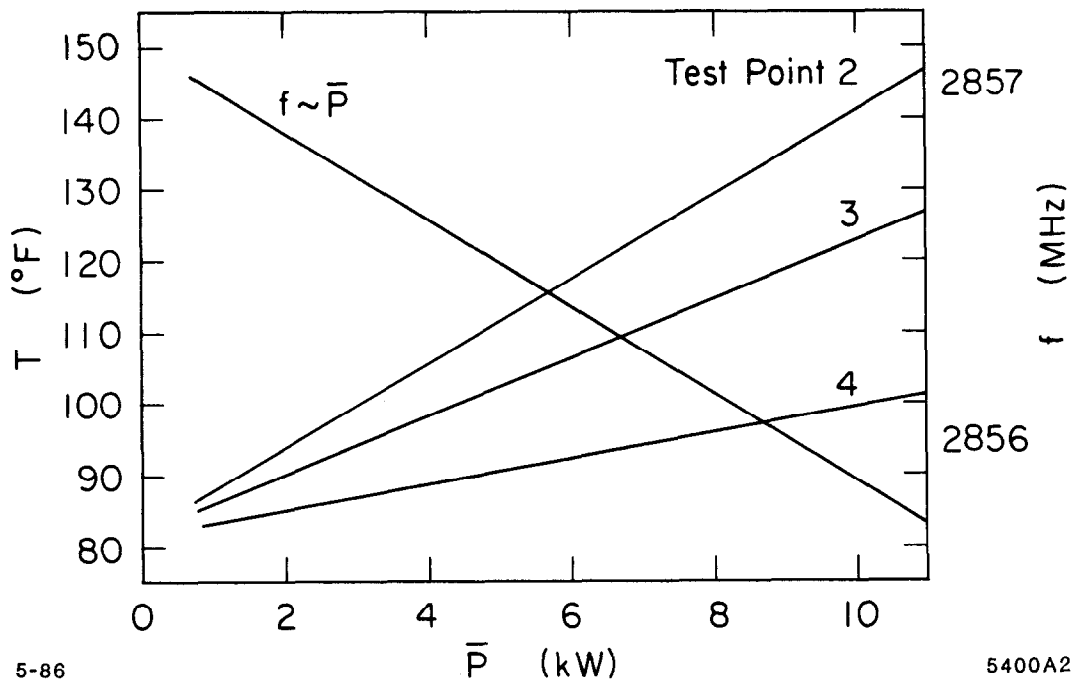


Fig. 5.12. Temperatures for the test points shown in Fig. 5.6, and resonant frequency, both as a function of average power dissipated in accelerator section.

where T_P is the length of the RF pulse and $T_C = 2Q_L/\omega$ or Q_0/ω since the loaded Q_L of the cavity is equal to $Q_0/2$. For our experiment, T_P was 2.5 μsec and $T_C \sim 0.75 \mu\text{sec}$. The ratio calculated by the above expression was monitored throughout the measurements by means of the directional couplers.

The cross-section of the field emitted beam was measured with a piece of cinemoid film placed on both upstream and downstream outside surfaces of the windows and found to be approximately 3 mm in diameter, almost independently of RF power level. The field emission electrons were very well focused because of the focusing effect of the RF field in the accelerating structure

The beam current transmitted through the downstream window was measured with the straight-ahead Faraday cup and found to reach 25 mA peak at 35 MW peak power, as shown in Fig. 5.13. By passing through the window, the electrons produced an electromagnetic shower and were scattered at various energies and angles. The relative beam current transmitted to the beam collector behind the slit formed by two lead bricks (see Fig. 5.6.) was measured as a function of the spectrometer setting between 0 and 4000 G to give energy spectra for various power levels. These energy spectra had to be corrected for scattering through the window and gas scattering. This was done with the aid of various people in the Health Physics group at SLAC by using the computer program EGS4³² which simulates bremsstrahlung, electron-electron scattering, ionization loss, pair production, photoelectric effect and multiple Coulomb scattering, and the computer program TRANSPORT. Corresponding to a certain energy of the electrons incident upon the window, a suitable magnetic field is needed to maximize the transmission through the slit. The ratio of current received by the collector to current incident upon the window was calculated (see the various examples of Fig. 5.14). This ratio was then used to renormalize the measured spectra at various power levels and obtain the actual electron spectra (see Fig. 5.15). The double humps correspond to electrons captured in the third cavity and accelerated through the entire section or captured in the sixth cavity and accelerated to the output end.

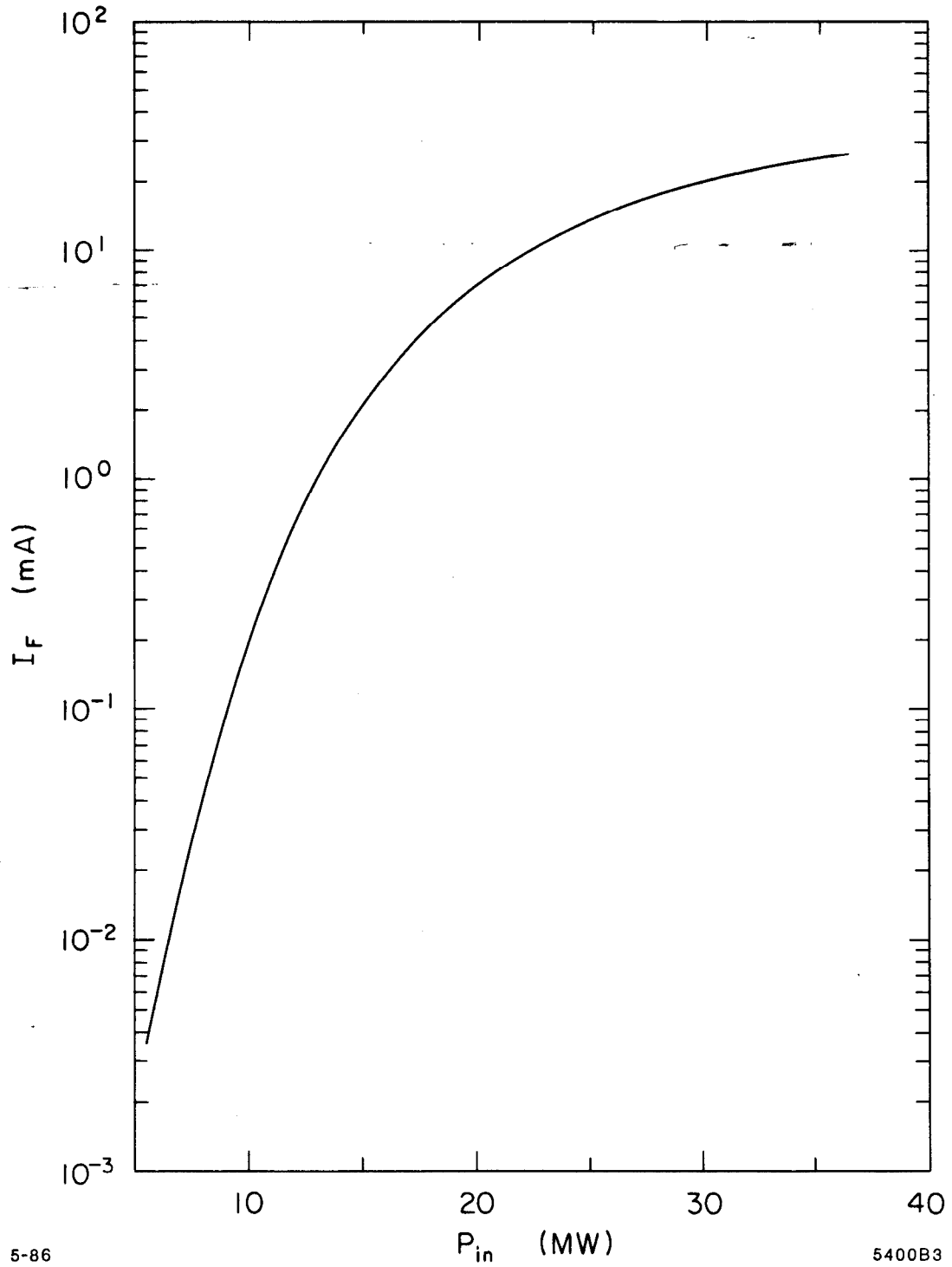


Fig. 5.13. Field emitted current transmitted through downstream window (right-hand side in Fig. 5.6) to Faraday cup, as a function of peak input power.

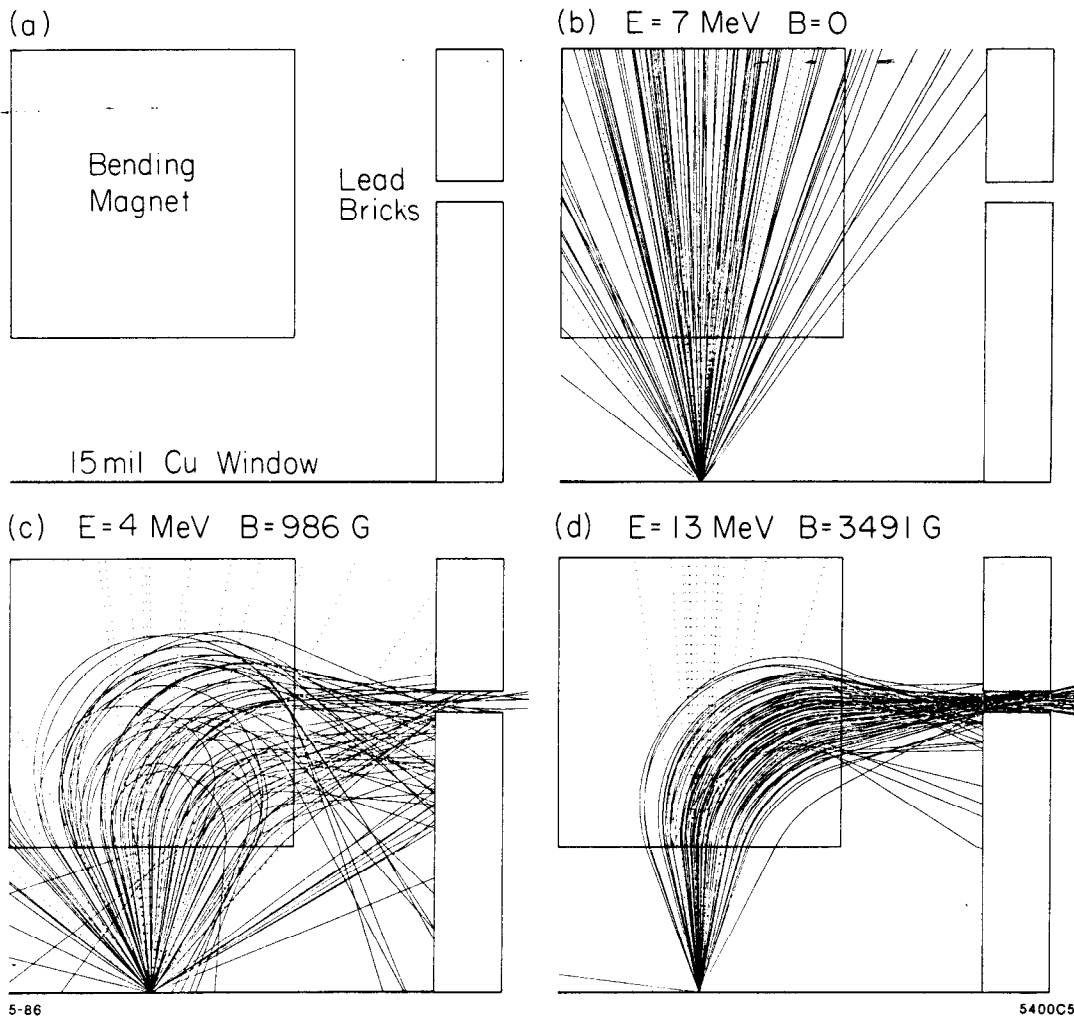


Fig. 5.14. (a) Layout of window, spectrometer magnet and slit; (b), (c) and (d) electron trajectories (continuous lines) and γ -rays (dotted lines) for various initial electron energies and magnetic fields.

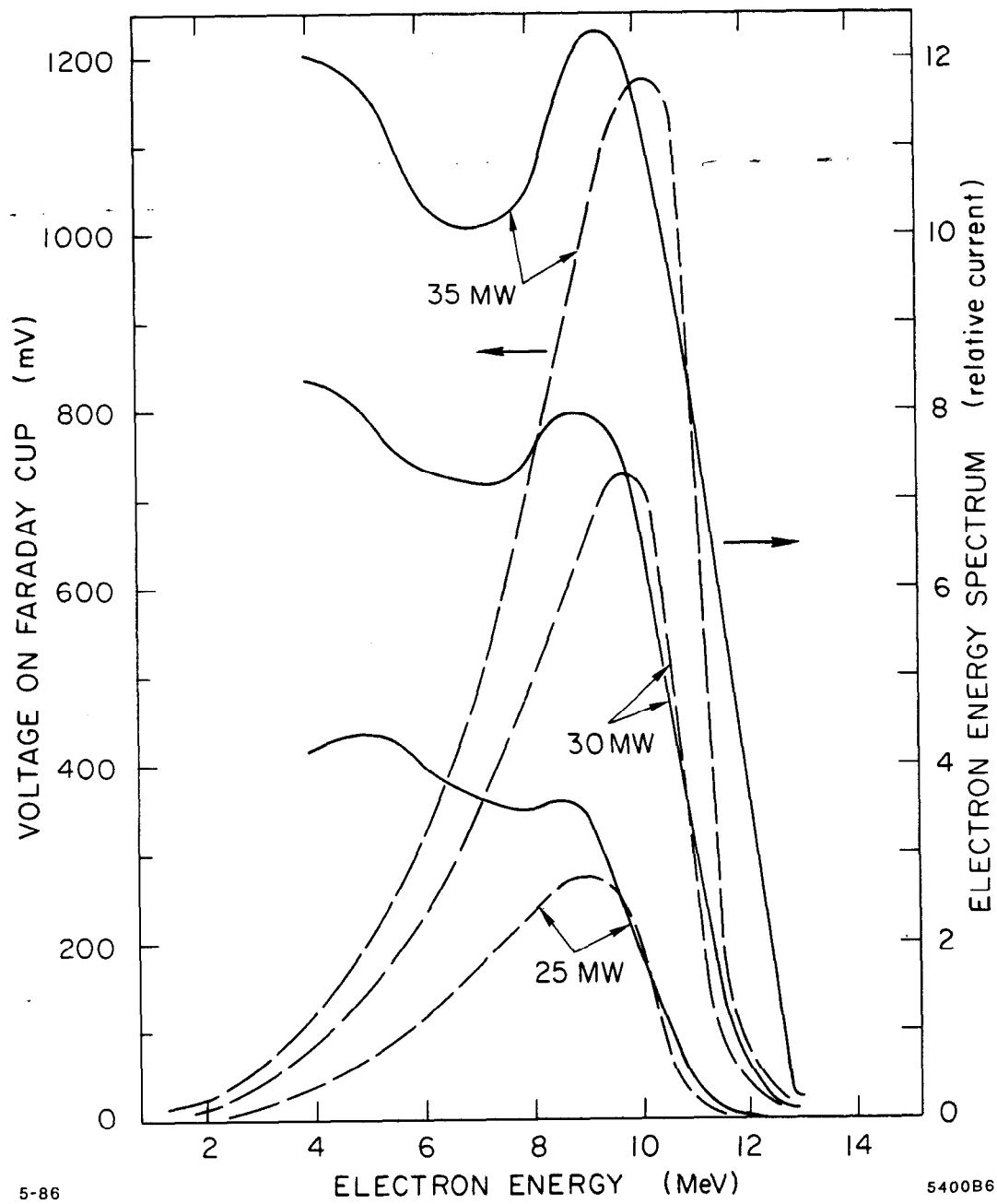


Fig. 5.15. Uncorrected (dashed lines) and corrected (continuous lines) electron energy spectra for various values of peak input power into S-band seven-cavity structure.

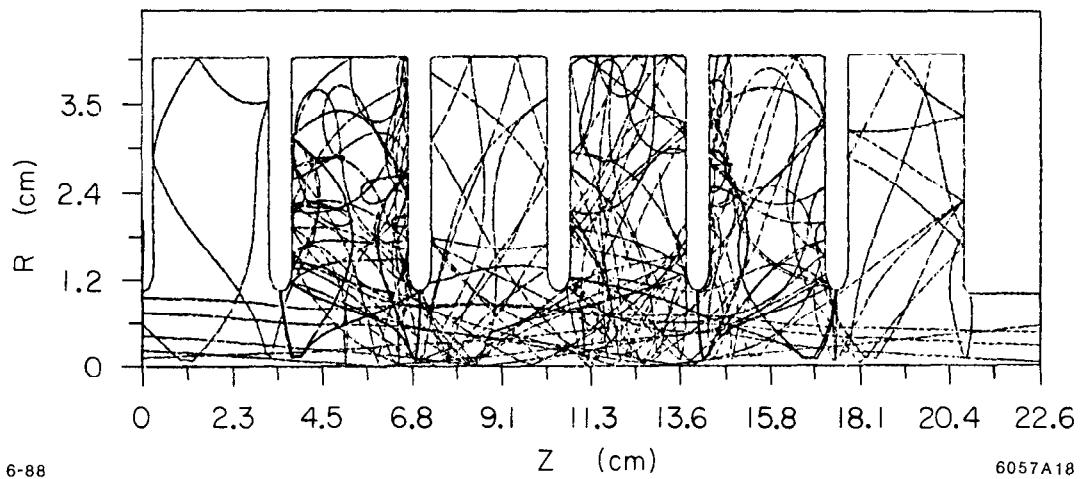
An attempt was made to calculate the possible trajectories and energies of FE electrons accelerated and focussed by the RF fields. Typical trajectories are shown in Fig. 5.16, as calculated by the program NEWTRAJ,³³ and indicate how an intense beam can actually be generated everywhere inside the structure. This code calculates the motion of an electron for which the initial energy, orientation and RF phase at departure are given. When the electron, which is accelerated by the RF field, strikes the cavity wall at some impact point, a “new” electron is generated. It may be a secondary or backscattered electron, depending on the energy of the impact electron and its impact angle.

When electrons of kinetic energies as high as 13 MeV hit the copper walls of the cavities, an electromagnetic shower is produced. The SLAC disk-loaded waveguide has an outer wall thickness of ~ 1 cm, which can stop almost all the electrons, but the bremsstrahlung γ -rays with energies above 0.5 MeV can pass through the walls without much loss. An extremely elevated x-ray dosage was measured by the small pre-calibrated ion chambers. The spatial distribution of the dosage is shown in Fig. 5.17. A specially made pin hole camera was used to obtain a picture of the transverse x-ray emission from the section. The picture revealed that at very high fields the disks were actually responsible for the highest transmission of x-rays.

5.3.2. S-Band π -Mode Accelerator Structure

The $2\pi/3$ -mode structure tests required that the power output of the available XK-5 klystron be pushed to its ultimate capability (47 MW). The two-cavity π -mode structure described here was built for two reasons: a) so that its breakdown field could be reached at a more conservative power level (~ 10 MW), and b) to test the principle of an idea²⁸ whereby an accelerator could be built with an array of such two-cavity structures, each one wavelength long and supplied by a separate source of moderate peak power (Fig. 5.18).

— The π -mode cavity is shown with its dimensions in Fig. 5.19. The principal design considerations were the choice of the beam hole dimension (2a), the



6-88

6057A18

Fig. 5.16. Field emitted electron trajectories plotted for S-band ($2\pi/3$) structure by means of computer program NEWTRAJ (courtesy of R. Parodi [Ref. 33]).

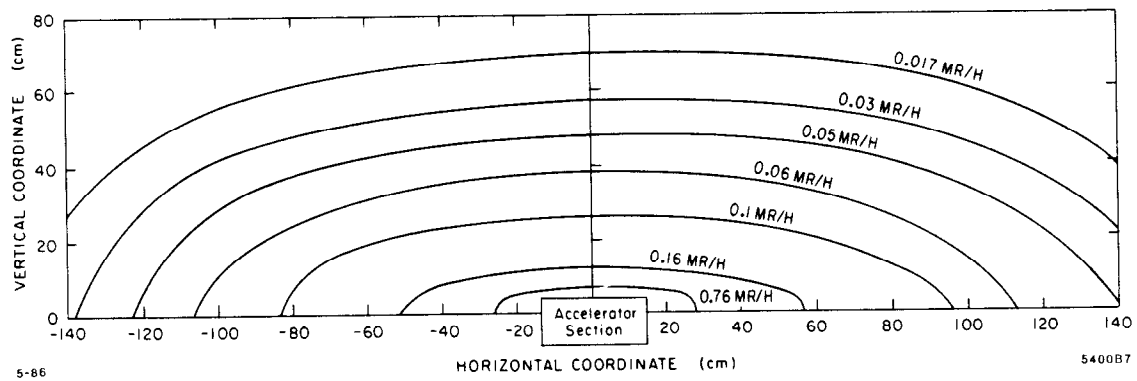


Fig. 5.17. Average x-ray dosage distribution around S-band (seven-cavity, $2\pi/3$ -mode) accelerator section (300 MV/m surface field, 2.5 μ sec, 120 pps).

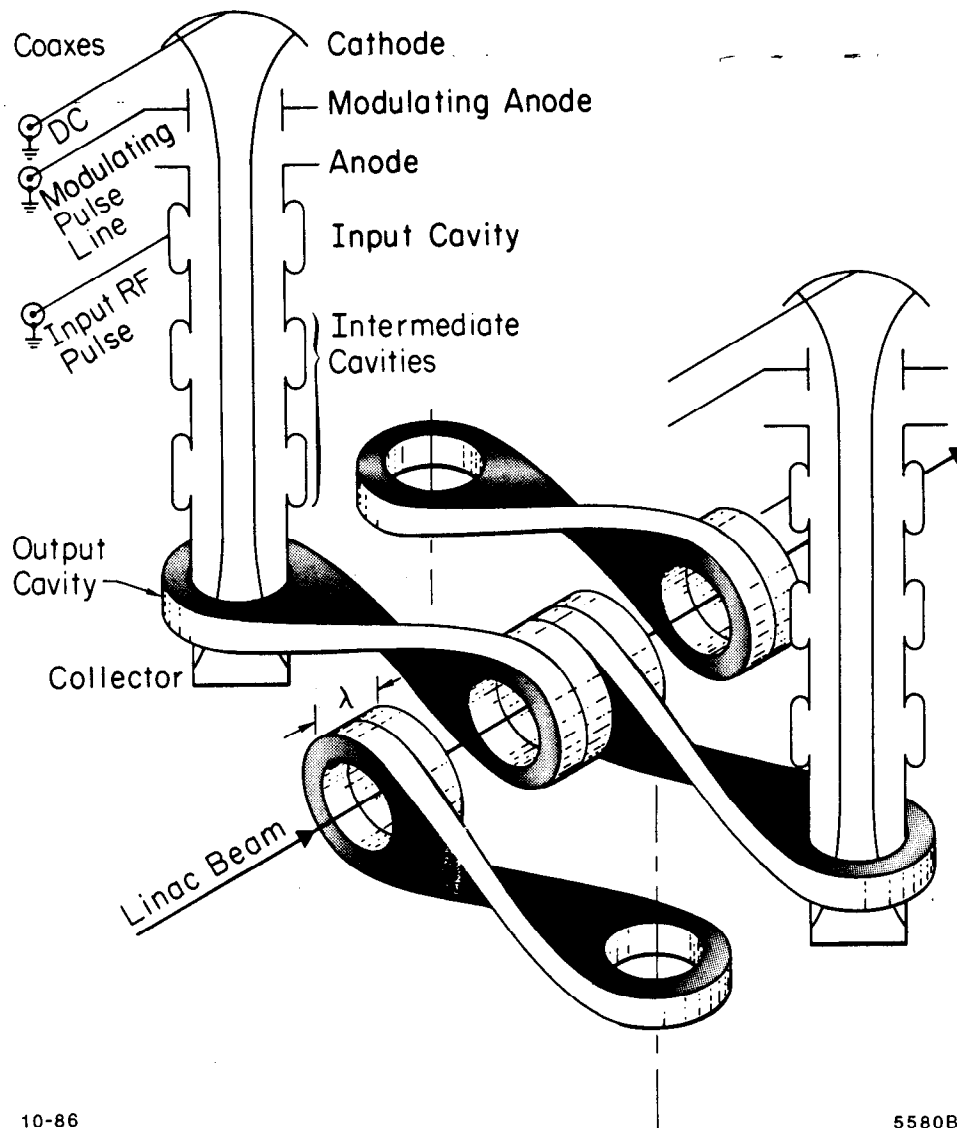
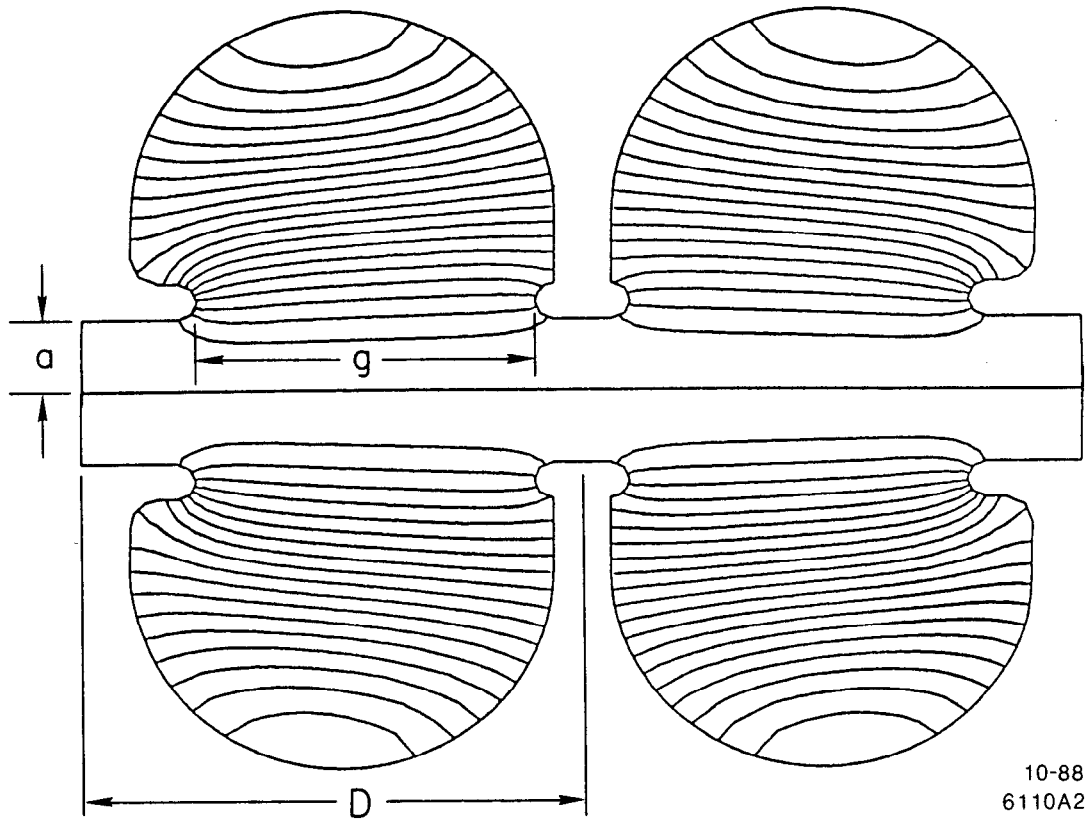


Fig. 5.18. Exploded view of continuous array of klystron beamlets and π -mode accelerator cavities directly connected to them (from Loew [Ref. 28]).



10-88
6110A2

Fig. 5.19. Cutaway view of S-band π -mode section.

maximization of the shunt impedance, the shape of the nose cones, and the frequency separation between the “0”- and “ π ”-mode resonances. All these factors interact with each other. Using available theory,³⁴ the beam hole dimension was chosen to give approximately the same longitudinal and transverse wakefields as the $2\pi/3$ -mode structure. The nose cones increase the shunt impedance but also enhance the E_s/\bar{E}_{acc} ratio (which is unfavorable for the ultimate accelerator but decreases the necessary klystron power for the tests). The nose cones between the two cavities also determine the coupling and the resulting mode separation. All the calculated parameters can be found in Table 5.1.

Using the same reasoning as for the $2\pi/3$ -mode section, the following relationship can be obtained:

$$E_{s,SW} = 103.62\sqrt{P_{in}} \quad \text{MV/m} \quad (5.13)$$

where P_{in} is in MW. This formula was corrected for the fact that the actual measured Q_0 was 16,310 instead of 18,489. The results are found in Table 5.2.

The two-cavity π -mode section was installed inside the vault of the SLAC Cryogenics Building in the same general configuration as the $2\pi/3$ -mode section. However, several modifications were made in the ancillary equipment. The vacuum system, shown in Fig. 5.20, consisted of a main 60ℓ ion pump, a cryo pump, an RGA (residual gas analyzer) with a 20ℓ ion pump and a leak valve to introduce various gasses into the section under controlled conditions.

5.3.3. C-Band and X-band Standing Wave Structure

The C-band and X-band tests reported here were done in collaboration with Varian Associates²⁵ to shed extra light on the breakdown phenomenon as a function of frequency and to examine the general behavior of structures at these higher frequencies where future linear colliders are likely to be built. As is well known, the advantages of the higher frequencies are higher shunt impedance (scaling as $\omega^{1/2}$), lower energy stored for a given gradient ($\sim \omega^{-2}$), shorter filling time

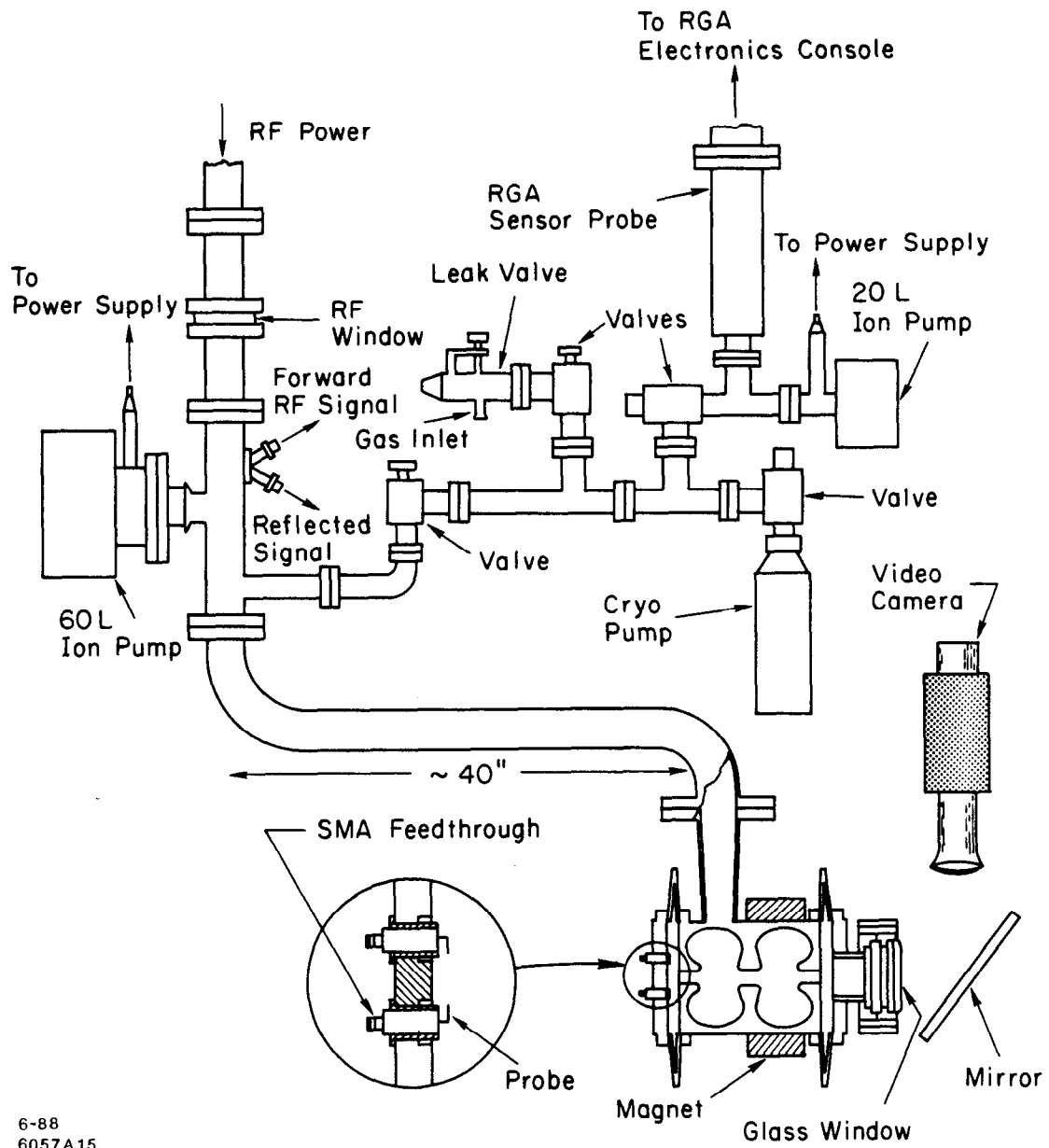


Fig. 5.20. Experimental set-up used for S-band (two-cavity, π -mode) structure, showing details of vacuum system.

($\sim \omega^{-3/2}$) and smaller dimensions ($\sim \omega^{-1}$). The main disadvantage is the lack of availability of high power sources. The experiments were done at Varian Associates with $\sim 1.5\text{MW}$ peak power magnetrons and the structures consisted of half-cavities. All the RF parameters calculated by SUPERFISH are listed in Table 5.1.

Figures 5.1 and 5.21 show the C-band half-cavity which was built at SLAC. This cavity was clamped to the end-plate with six bolts torqued to 100 inch-pounds. The cavity was made out of OFHC copper and the end-plate was made out of stainless steel plated with copper. In order to obtain good RF contact and eliminate any gap between the cavity body and the end plate, a knife-edge was machined around the cavity. Two indium gaskets were placed at the outer diameter of the cavity body to maintain high vacuum. The microwave power was transmitted through the coupling iris in the end-plate. A quarter-wavelength transformer was designed to reduce the size of the coupling iris. The dimensions of the coupling iris to obtain a perfect match between the cavity and the outer RF system were arrived at empirically. To minimize the shift in resonant frequency caused by heat deformation of the cavity under high power operation, a cooling water passage was incorporated within its body. The power transmitted to the cavity was monitored by a small current probe made from a feedthrough located in the end-plate.

The X-band cavity, which is shown in Fig. 5.1, was made at Varian Associates. The basic tester assembly was quite similar to that of the C-band test shown in Fig. 5.21. A pure copper gasket was pressed between the cavity and the end-plate to maintain high-vacuum and good electric contact. In a later version of the X-band tester, several improvements were made. The cavity wall was pushed or pulled through a threaded connection which was operated by a stepping motor. By adjusting the amplitude and direction of the voltage on the stepping motor, the resonant frequency of the cavity could be made equal to the RF frequency of the magnetron. A glass view port was added to the cavity body to permit observation of surface phenomena during RF processing and breakdown.

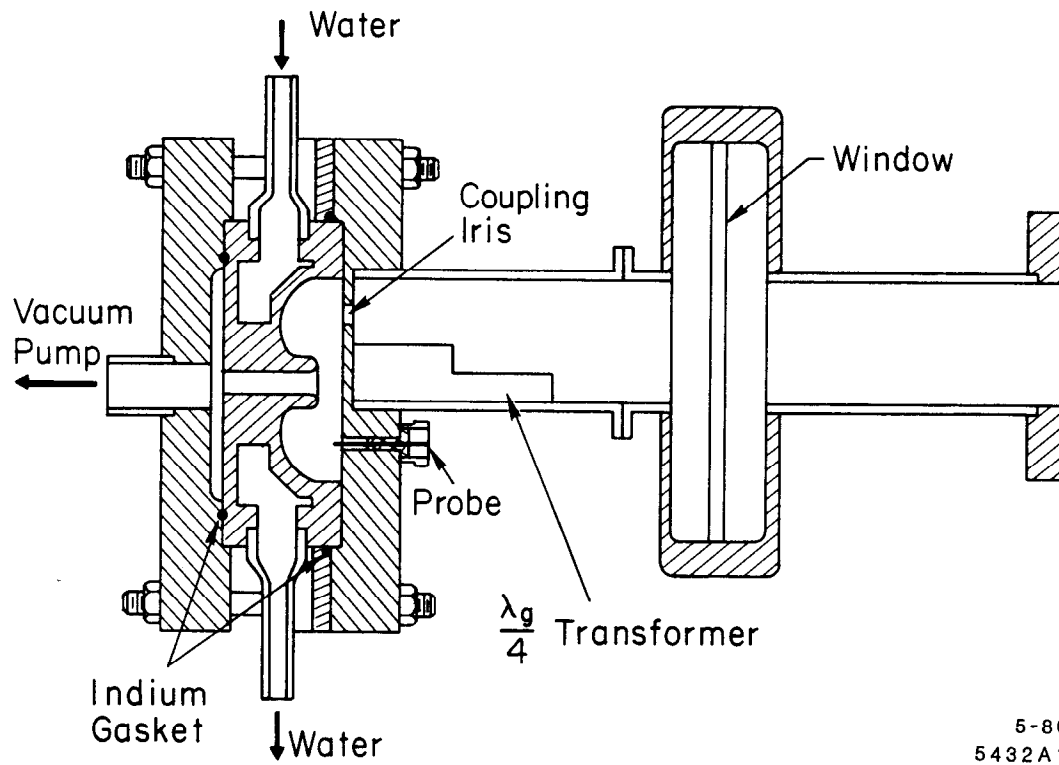


Fig. 5.21. C-band tester for high-gradient experiments.

Figure 5.22 is a picture of the set-up for the X-band high-gradient test.

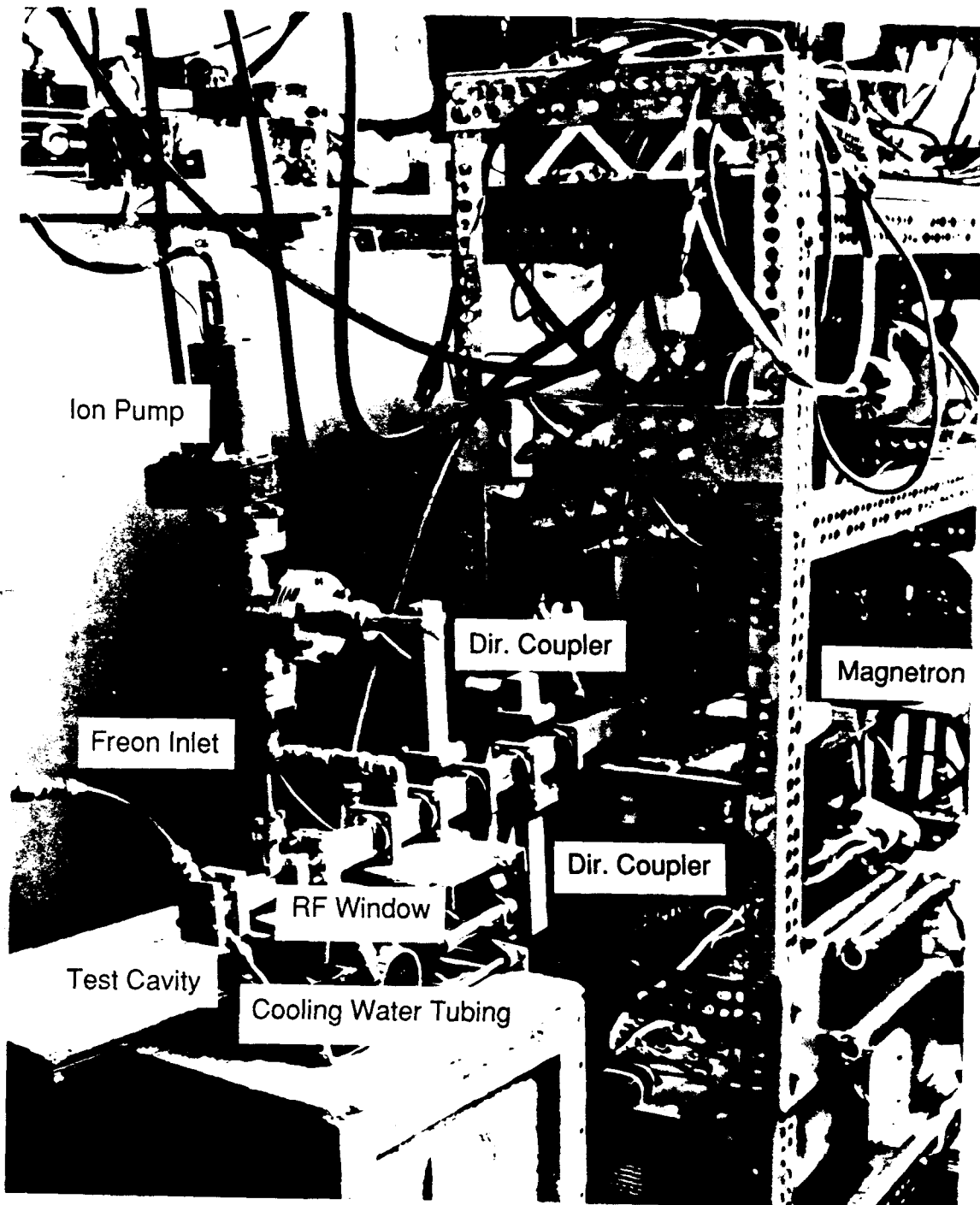
5.3.4. 11.424 GHz High Gradient Accelerator

The last structure which was designed for this series of tests was a traveling-wave section built in conjunction with the relativistic klystron program being carried out at SLAC and LLNL.²⁷ This program is expected to result in a power source producing ~ 50 nsec pulses of 0.5 - 1.0 GW power at 11.424 GHz, which could be used to test such a traveling-wave structure up to accelerating gradients of 200 MV/m. The section which was built was a constant-impedance, $2\pi/3$ -mode disk-loaded waveguide with a $(2a)$ dimension of 0.75 cm, large enough to give relatively small wake fields, a large group velocity ($v_g/c = 0.031$) and a filling time of 28.4 nsec for a length of 30 cells. The RF parameters calculated by SUPERFISH are listed in Table 5.1. The structure was assembled from machined cups (shown in the lower right-hand corner of Fig. 5.1) brazed together and fitted with input and output couplers. The coupling cavity and tapered rectangular waveguides were machined out of single pieces of copper and their dimensions were obtained by extrapolation from S-band data and cold tests. A special tool permitted each cavity to be tuned up or down in frequency to obtain the correct phase advance per cell. Figure 5.23 shows the assembled section on the left and the microwave set-up used for the measurements.

As mentioned earlier, however, the high power results shown in Table 5.2 are only preliminary because the maximum power obtained so far from the relativistic klystron has not exceeded 200 MW.

5.3.5. Chemical Cleaning and Baking

At various stages when the sections described above were removed from the experimental area and had to be machined, they were subsequently cleaned. The chemical procedure that was typically used for the $2\pi/3$ -mode and π -mode structures is described in Table 4. The various steps that are listed were empirically developed by the Plating Shop at SLAC. Occasionally, the sections were also



5-89

6110A12

Fig. 5.22. Experimental set-up used for X-band cavity.

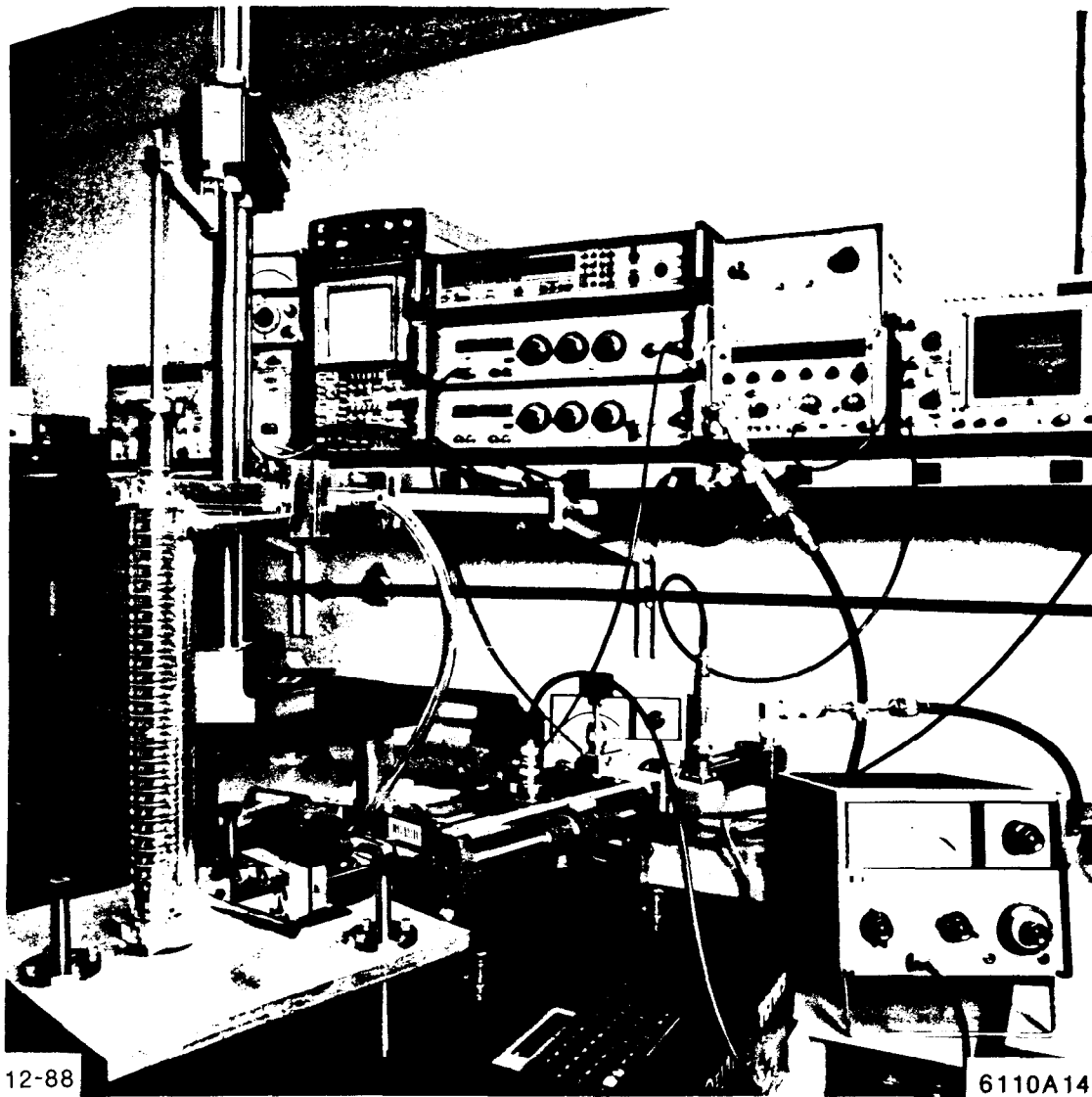


Fig. 5.23. High gradient 11.424 GHz accelerator section and equipment set-up for microwave measurements.

baked at 250°C, principally to remove the water vapor from the inside surfaces. This procedure seemed well-suited to shorten the RF processing time.

Table 5.4. Procedure for chemical cleaning.

- | |
|---|
| <ul style="list-style-type: none"> • Vapor degrease in trichlorethane for five minutes • Remove oxide by immersion in non-etch copper cleaner (citrate, McDermid 9268) at 100°F for five minutes • Tap water rinse • Immerse in OXYBAN 60 solution for two minutes • Rinse in tap water, cold and hot de-ionized water • Immerse in 115°F isopropyl alcohol for 15 seconds • Blow with dry air • Dry in hot air oven at 150°F for two hours |
|---|

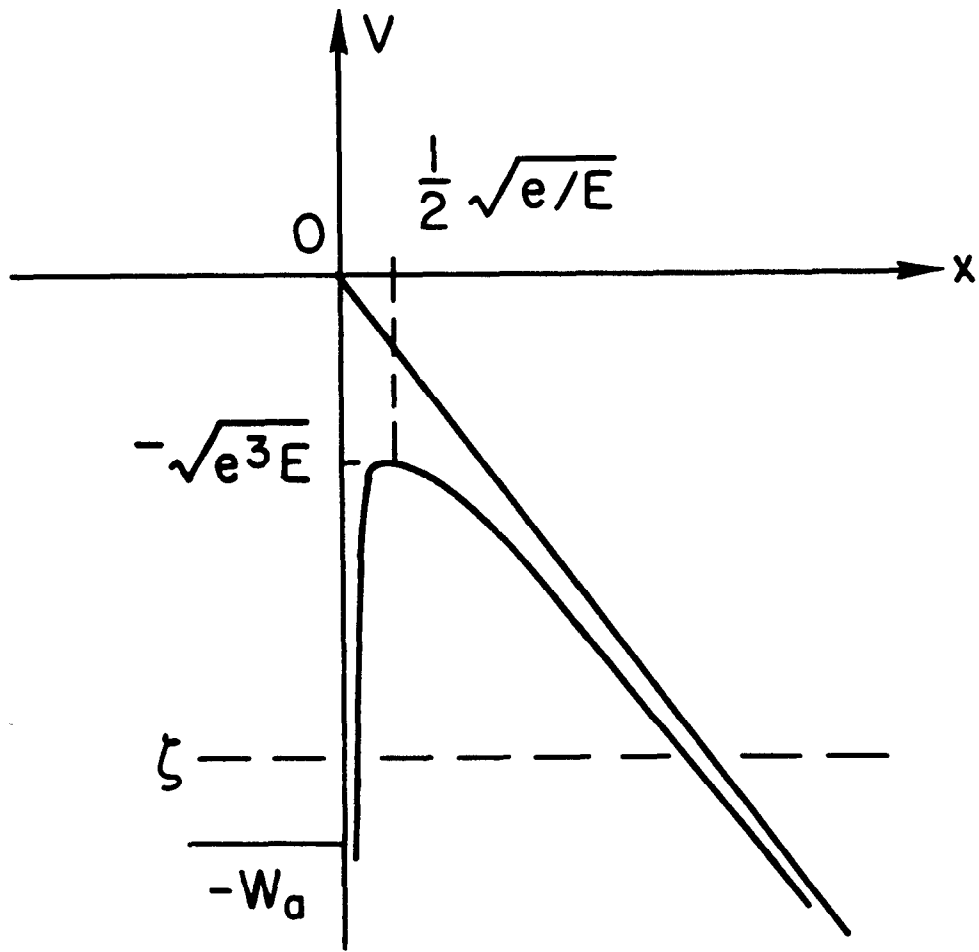
5.4. FIELD EMISSION AND FOWLER–NORDHEIM PLOTS

An understanding of electron field emission (FE) is a prerequisite to discussing prebreakdown and breakdown phenomena. In this section, we review the Fowler-Nordheim equation and associated field plots, the problem of DC and AC electron emission and several physics models for enhanced field emission (EFE).

5.4.1 DC Field Electron Emission from Ideal Metal Surface

Following Sommerfeld, Fowler and Nordheim calculated the quantum mechanical tunnelling of conduction electrons through a modified potential barrier at an ideal metal surface in an applied electric field.^{35,36} The actual mathematical derivation is briefly outlined below. The one-dimensional potential barrier is illustrated in Fig. 5.24. The effective potential energy $V(x)$ is

$$V(x) = \begin{cases} -W_a & \text{where } x < 0 \\ -eEx - e^2/4x & \text{where } x > 0 \end{cases}, \quad (5.14)$$



4-87

5387A3

Fig. 5.24. Potential energy diagram showing the modified electric field potential barrier.

where the term $-e^2/4x$ is the contribution of the interaction of the emitted electron with its image charge and $-W_a$ is the potential energy of the electron when it is inside the metal. Fowler and Nordheim assumed that the conduction electrons in the metal form a gas of free particles which obey Fermi-Dirac statistics. The number of electrons within a volume v and with momenta within the range $dP_x dP_y dP_z$ can be expressed by

$$dn = \frac{2v}{h^3} \frac{dP_x dP_y dP_z}{e^{\frac{\epsilon - \zeta}{kT}} + 1} , \quad (5.15)$$

where h is Planck's constant, k is Boltzmann's constant, ζ is called the Fermi energy and T is the temperature. The flux of electrons that have normal energy components between W_x and $W_x + dW_x$ and are incident upon the barrier at the surface of the metal is $N(W_x)dW_x$, where $N(W_x)$ is the supply function which can be found by integrating Eq. (5.15) over all P_y and P_z . The probability $D(W_x)$ of an electron tunnelling through the barrier is called the transmission coefficient. Using the WKB approximation, the solution for the time-independent Schrödinger equation yields

$$D(W_x) = \exp \left[- \int_{x_1}^{x_2} \sqrt{\frac{8m}{\hbar^2} [V(x) - W(x)]} dx \right] , \quad (5.16)$$

where x_1 and x_2 are the zeros of the radicand. The total number of electrons that tunnel through the barrier is obtained by integrating the expression $N(W_x)D(W_x)dW_x$ over all energies. Ordinarily, the lowest energy $-W_a$ is far below the Fermi energy. By setting this limit to $-\infty$, the field emission current density j_F can be obtained:

$$j_F = e \int_{-\infty}^{\zeta} D(W_x) N(W_x) dW_x . \quad (5.17)$$

For low temperature ($T \leq 300^\circ\text{K}$), it has the form:

$$j_F = \frac{1.54 \times 10^{-6} E^2}{\phi t^2(y)} \exp \left[\frac{-6.83 \times 10^9 \phi^{1.5} v(y)}{E} \right] \text{ (A/m}^2\text{)} , \quad (5.18)$$

where E is the surface electric field in V/m, ϕ is the work function of the emitting material in eV, $t(y)$ and $v(y)$ are tabulated dimensionless elliptic functions, and

$$y = 3.79 \times 10^{-5} E^{0.5} / \phi \quad (5.19)$$

$$v(y) = 0.956 - 1.062 y^2 . \quad (5.20)$$

By substituting these into (5.18) and letting $t(y) \approx 1$, the Fowler-Nordheim equation takes the following form:

$$j_F = \frac{1.54 \times 10^{-6} \times 10^{4.52\phi^{-0.5}} E^2}{\phi} \exp \left(- \frac{6.53 \times 10^9 \phi^{1.5}}{E} \right) \text{ (A/m}^2\text{)} . \quad (5.21)$$

5.4.2 Enhanced Field Emission (EFE)

In reality, any metal surface in an accelerator cavity is far from planar and clean, and as a result there are large variations in the microscopic surface field. A local field enhancement can be caused by a protruding microstructure or a dielectric impurity. The resulting field enhancement β is the ratio of the microscopic electric field E_m at the surface irregularity to the ideal field E :

$$\beta = \frac{E_m}{E} . \quad (5.22)$$

If we assume that the surface irregularity has an effective emitting area A_e , the resulting field emitted current I_F can be derived from Eq. (5.21) as follows:³⁷

$$I_F = \frac{1.54 \times 10^{-6} \times 10^{4.52\phi^{-0.5}} A_e \beta^2 E^2}{\phi} \exp \left(- \frac{6.53 \times 10^9 \phi^{1.5}}{\beta E} \right) \text{ A} . \quad (5.23)$$

The numerical value of β for a particular surface can be obtained by plotting I_F/E^2 versus $1/E$ on semilog paper and noting that the slope of the line is given by:

$$\frac{d(\log_{10} I_F/E^2)}{d(1/E)} = - \frac{2.84 \times 10^9 \phi^{1.5}}{\beta} . \quad (5.24)$$

The intercept of the $\log_{10} I_F/E^2$ line with the $1/E$ axis, i.e.

$$\log_{10} (I_F/E^2)_{E \rightarrow \infty} = \log_{10} \left[\frac{1.54 \times 10^{-6} A_e \beta^2 10^{4.52\phi^{-0.5}}}{\phi} \right] , \quad (5.25)$$

enables one to calculate the value of A_e .

The effect of random emitter arrays has been studied by several authors.^{38,39} It turns out that the Fowler-Nordheim plot based on the total field emission current due to several emitters still looks like a straight line, the slope of which approximates the β value of the sharpest emitter. The resulting emitting area yields a value somewhat lower than the summation of the individual areas for each of the emitters.

5.4.3 Enhanced Field Emission Models

Geometric Field Enhancement

If we consider a pure metal surface, irregularities such as protrusions or cracks will result in a geometrically enhanced local electric field. This field enhancement has been reported by a number of authors^{37,40,41} and β -values have been calculated and plotted for a few idealized geometries.

For a semi-ellipsoid with semi-major axis h (height) and semi-minor axis b (half width of the base), the enhancement factor can be expressed as:

$$\beta = \frac{(\lambda^2 - 1)^{1.5}}{\lambda \ln \left[\lambda + (\lambda^2 - 1)^{0.5} \right] - (\lambda^2 - 1)^{0.5}} , \quad (5.26)$$

where $\lambda = h/b$. If $\lambda \sim 1$, which corresponds to a semisphere on a plane, the enhancement factor β is ~ 3 . For a needle-like microprotrusion ($\lambda \gg 10$), the approximate expression for β becomes

$$\beta \simeq \frac{\lambda^2}{\ln \lambda - 0.3} \quad (5.27)$$

For a cylinder topped by a semisphere with height $h \geq 5r$, a simple expression for β can be written as:

$$\beta \simeq \frac{h}{r} + 2 \quad (5.28)$$

Figure 5.25 shows enhancement factors as a function of h/r or h/b for several cases: sphere above plane, cylinder topped by semisphere and ellipsoid. As can be seen, β -values as high as 1000 can be reached in theory. In practice, as will be shown later, after many hours of RF processing, the surface irregularities due to breakdown as observed with a scanning electron microscope in one of our cavities lead to calculated β -values between 5 and 10. On the other hand, the values measured in the S-band cavities from Fowler-Nordheim plots are on the order of ~ 60 . To explain this disparity, it is necessary to consider another enhanced field emission mechanism due to dielectric impurities.

Non-Metallic Field Emission Enhancement

The enhanced field emission from a contaminated metal surface was experimentally studied by using sophisticated in situ analytical techniques.^{42,43,44} To explain the experimental results, several models have been proposed. One of the prevalent ones is by Latham and his co-workers.^{45,46} and is called Field-Induced Hot-Electron Emission model (FIHEE). This theory assumes that oxides, adsorbed organic residues or dielectric inclusions exist on the metal surface, especially in the vicinity of surface cracks or between grain boundaries. These impurities can be in intimate contact with the metal, perhaps partially embedded as shown schematically in Fig. 5.26. The band diagram is shown in Fig. 5.27. Without external field, the metal-insulator interface forms a blocking contact with band bending on the interface (the so-called "off" state of a conducting channel). When an external electric field is applied, the electric field penetrates through

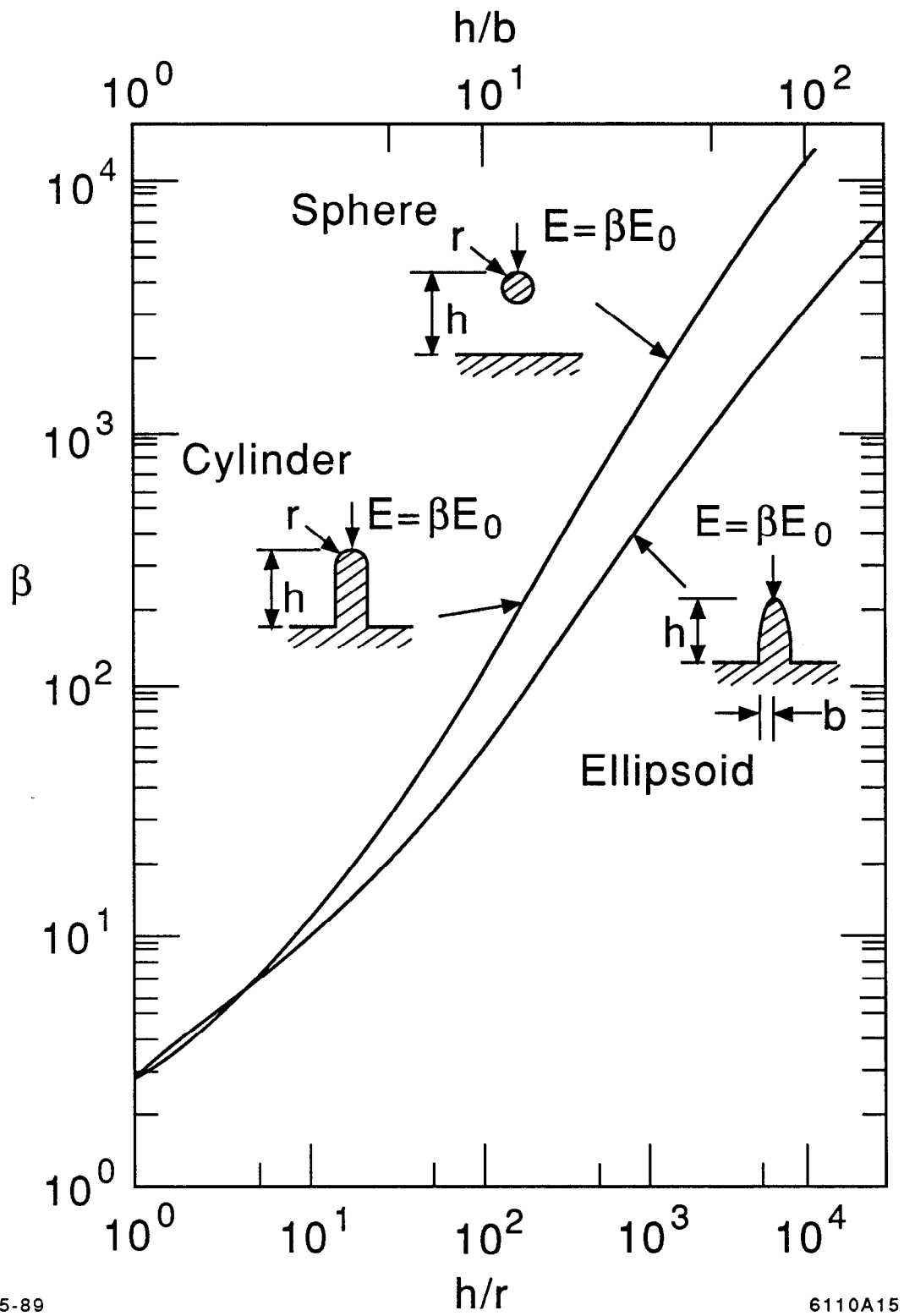


Fig. 5.25. Field enhancement factor β associated with various idealized micro-protrusion geometries (From Rohrbach [Ref. 40]).

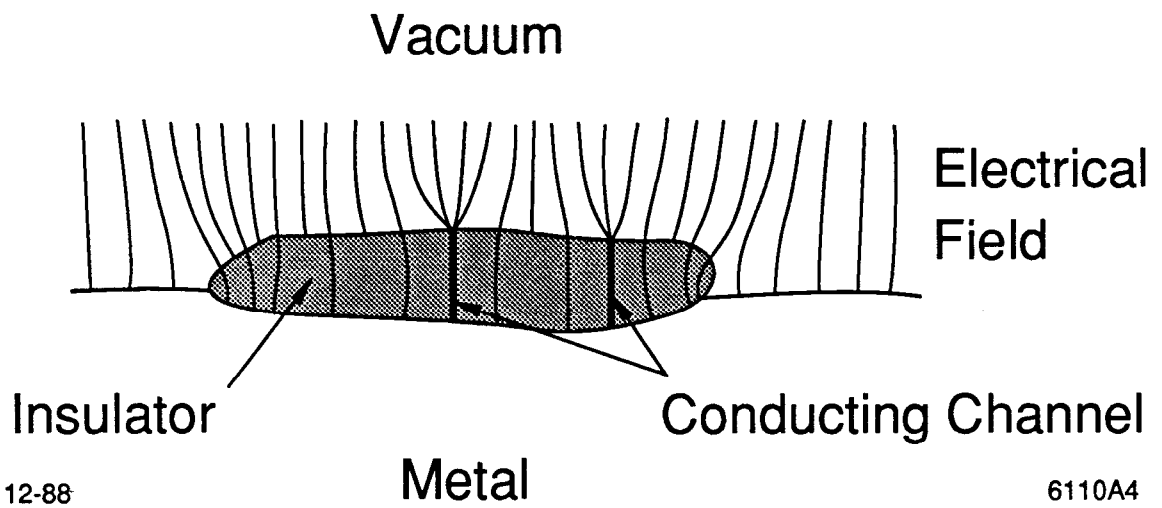
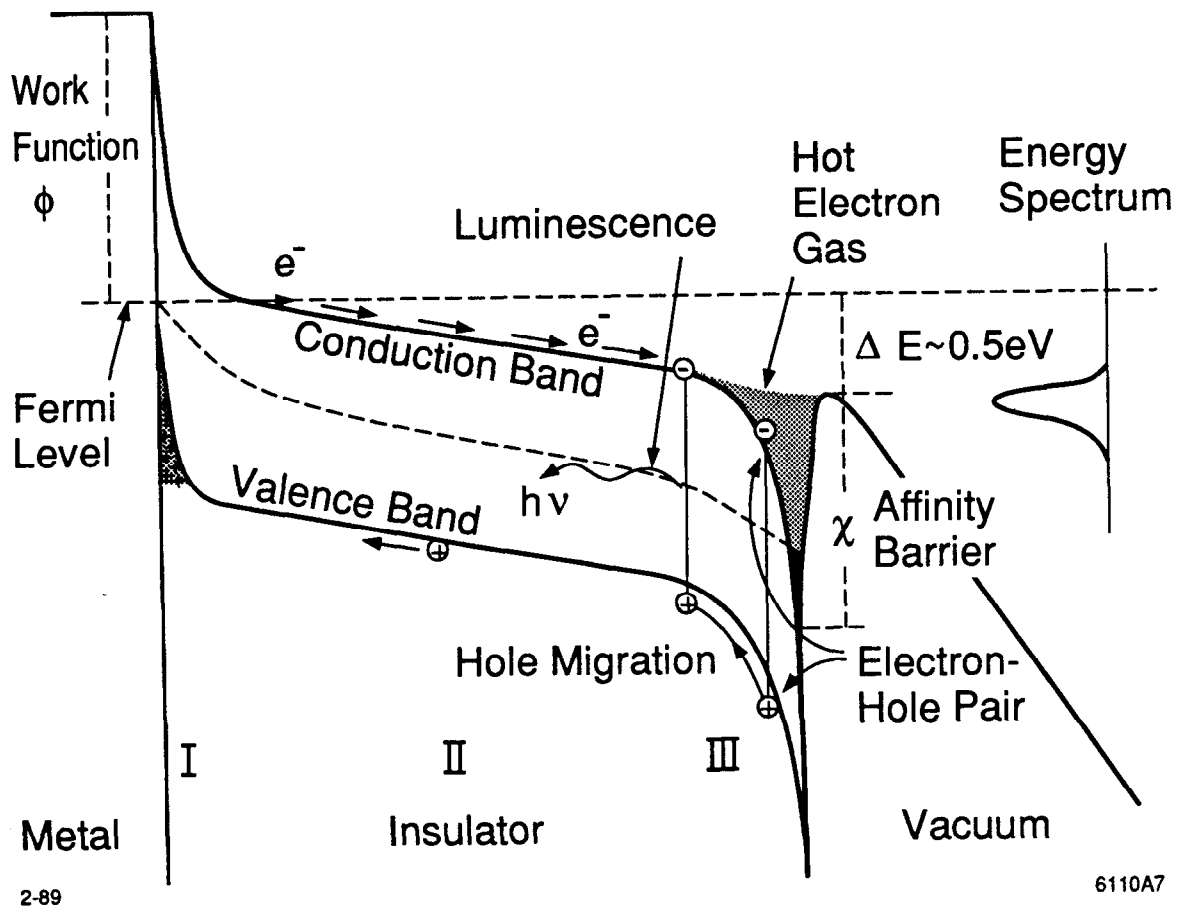


Fig. 5.26. A schematic representation of the emission regime showing the conducting channels in the insulating inclusion and the associated microscopic field enhancement (from Latham [Ref. 46]).



2-89

6110A7

Fig. 5.27. A band-diagram of a "on" state of an electron and photon emitting composite microregime (From Latham [Ref. 37]).

the entire insulating layer. As the external field is increased, the metal-insulator barrier becomes thin enough for electrons to tunnel into the conduction band of the insulator to fill empty traps and insulator surface states. A subsequent increment in external field finally leads to the "on" state of a conducting channel at some specific location.

The electrons initially tunnel through the potential barrier of the metal-insulator interface in Region I (see Fig. 5.27), and are then accelerated (thermalized) through the insulator in the bottom of the conduction band in Region II. Having higher effective temperature, the heated electrons are stored near the insulator surface. Just like the electrons at a metal surface at high temperature, they obey Maxwell-Boltzman statistics and are emitted in a quasi-thermionic process following the Richardson-Dushman law (discussed later in detail in Section 5.7.). As a result, the external field penetrates more effectively into the insulator and enhances the tunneling.

In the high-field Region III, the electron-phonon scattering process creates electron-hole pairs, the holes migrate toward the metal-insulator interface and build a positive space charge layer which reinforces the conducting tendency. At the same time, the recombination of electrons and holes near the vacuum interface via interband trapped states causes the release of a few eV photons, thereby explaining the observed electroluminescence. This initial threshold switching process occurs in a few ns at highly localized filaments or channels where the presence of high charge-carrier concentration causes the band structure to rearrange itself to a stable equilibrium configuration: subsequently in an few μ s, the conduction channel will be electroformed to a permanent structure, as shown in Fig. 5.26.

Latham and Bayliss experimentally studied the spectral characteristics of the field emitted electrons from a planar electrode. Their quantitative analysis explains the dependence of the spectral width (FWHM) and spectral shift from the Fermi level of the cathode material on the field amplitude. Furthermore, their theoretical calculation for the emitted current closely fits the results obtained

experimentally from Fowler-Nordheim plots with β values in the range from 300 to 500.

Dynamical Enhanced Field Emission Model

Halbritter⁴⁷ proposed a rather complicated alternative mechanism for enhanced field emission, which is called the dynamical enhanced field emission model. The most significant contribution of this model is to predict that the self-sustained enhanced field emission is pulsating. In a way similar to the FI-HEE model, it assumes that low-density adsorbates (like hydrocarbons, H_2O ,) contaminate the metal surface. When an electric field is applied, some electrons are emitted from the metal and gain energy from the electric field, which penetrates into the contaminants. The hot electrons can create impact ionization, which yields a high conductivity state without causing the destruction of the material. The immobile positive charges left behind at the metal-adsorbate boundary enhance the field emission and cause a fast growth of the field emission current. However, the positive charges in the adsorbate also increase the electron affinity in the contaminant-vacuum interface, and only the fastest electrons can penetrate through the potential barrier at the contaminant-vacuum interface into the vacuum. In addition to the impact ionization, the inelastic process for hot electrons is accompanied by the emission of photons and gas desorption. The initial fast growth of the enhanced field emission is counteracted by the following effects: a) the increased affinity allows less electrons to penetrate through the adsorbate-vacuum interface, b) as the kinetic energy of the hot electrons is increased, the cross-section of the inelastic scattering is also increased, and the ability of the hot electrons to penetrate the affinity barrier is decreased, c) the slowed-down electrons can neutralize the positive charges, thereby reducing the enhanced field emission. As a result, the field emission is saturated, depressed and finally stopped for a short time before the whole process starts again. In other words, the emission current is caused to pulsate.

A pulsation on the order of 1 ns for a 0.1 μm adsorbate coating on a metal surface was predicted and observed.⁴⁷ For the RF case, the enhancement factor can be obtained by using an average field emission current (which will be calculated in the following section). Many high gradient measurements have shown that for a similar surface condition, the enhancement factor β decreases as the applied RF frequency is increased. According to the dynamical model, the build-up time has a significant influence on the charging and avalanche process when the RF frequency f is greater than 1 GHz. This gives a qualitative explanation for the decrease in β with increased RF frequency.

5.4.4. Field Electron Emission for Alternating Field

If we assume that the electric field on a metal surface is of the form $E_0 \sin \omega t$, the average field emission current can be calculated by time-averaging of Eq. (5.23):

$$\bar{I}_F = \frac{1}{T} \int_0^T I_F(t) dt = \frac{1.54 \times 10^{-6} A_e \beta^2 E_0^2 10^{4.52\phi^{-0.5}}}{\phi} \frac{2}{T} \int_0^{\frac{T}{4}} \sin^2 \omega t \exp\left\{-\frac{6.53 \times 10^9 \phi^{1.5}}{\beta E_0 \sin \omega t}\right\} dt ,$$

where T is the period of the RF field. Then, the problem becomes one of solving the following integration:

$$S(\mu) = \frac{2}{T} \int_0^{\frac{T}{4}} \sin^2 \omega t \exp\left\{-\frac{\mu}{\sin \omega t}\right\} dt , \quad (5.29)$$

where

$$\mu = \frac{6.53 \times 10^9 \phi^{1.5}}{\beta E_0} . \quad (5.30)$$

In a similar way to Ref. 48, let us substitute $1/x$ for $\sin \omega t$, and rewrite the integration $S(\mu)$ as:

$$\begin{aligned}
S(\mu) &= \frac{1}{\pi} \int_1^{\infty} \frac{e^{-\mu x}}{x^3 \sqrt{x^2 - 1}} dx \\
&= \frac{1}{\pi} \int_1^{\infty} R(x) \frac{e^{-\mu x}}{\sqrt{x - 1}} dx ,
\end{aligned}$$

where

$$R(x) = \frac{1}{x^3 \sqrt{x + 1}} .$$

It yields

$$S(\mu) \approx \frac{1}{\pi} \tilde{R}(\mu) \int_1^{\infty} \frac{e^{-\mu x}}{\sqrt{x - 1}} dx = \frac{\tilde{R}(\mu)}{\sqrt{\pi \mu}} e^{-\mu} . \quad (5.31)$$

$\tilde{R}(\mu)$ is a slowly varying function of μ . A numerical calculation of the integration of $S(\mu)$ shows that for different conducting materials and large variations of the field strength, $R(\mu)$ only changes by $\pm 8\%$ from 0.53. Then the field-emission current for an alternating field can be expressed as:

$$\begin{aligned}
\bar{I}_F &= \frac{5.7 \times 10^{-12} \times 10^{4.52\phi^{-0.5}} A_e (\beta E_0)^{2.5}}{\phi^{1.75}} \\
&\quad \exp \left\{ -\frac{6.53 \times 10^9 \times \phi^{1.5}}{\beta E_0} \right\} \text{ A} ,
\end{aligned} \quad (5.32)$$

where ϕ is the work function in eV, E_0 is the amplitude of the macroscopic surface field in V/m, β is the enhancement factor and \bar{I}_F is the average field emission current on an emitting area A_e in m^2 .

5.5. VACUUM BREAKDOWN PHENOMENA AND SOME BREAKDOWN MODELS

5.5.1. The Kilpatrick Criterion and Its Derivation

The Kilpatrick criterion⁷ was based on the idea that breakdown happens when field emission is enhanced by a cascade of secondary electrons ejected from the cathode by ion bombardment. Assuming a linear dependence of secondary electron emission upon maximum ion energy, an expression for the breakdown or “*sparking*” threshold was obtained empirically from a number of experimental points from diverse laboratories, as:

$$WE^2 \exp(-1.7 \times 10^5/E) = 1.8 \times 10^{14} \quad , \quad (5.33)$$

where W is the maximum possible ionic energy in electron volts, and E is the electric cathode gradient in V/cm. The relationship of W vs. E is presented graphically in Fig. 5.28.

For the RF case, the calculation of the maximum possible ionic energy W must include the effects of transit-time and phase. Kilpatrick only considered the case of parallel plate electrodes with gap width g . Figure 5.29 shows how the maximum ion energy W depends on the RF voltage V . The quantity V^* is defined as

$$V^* = (g/\lambda)^2 (m_0 c^2 / \pi q), \quad (5.34)$$

where $\lambda = \lambda/2\pi$, q is the electron charge and m_0 is the mass of atomic hydrogen. It turns out that all the experimental points which he collected fell in the linear region [$V/V^* \leq 1$] where the slope for W/V is approximately $0.636V/V^*$. The maximum energy of an ion can then be derived as

$$W = \frac{0.159 q^2 E^2}{m_0 \pi f^2} \quad . \quad (5.35)$$

This result could have been obtained directly by solving the simple differential equation

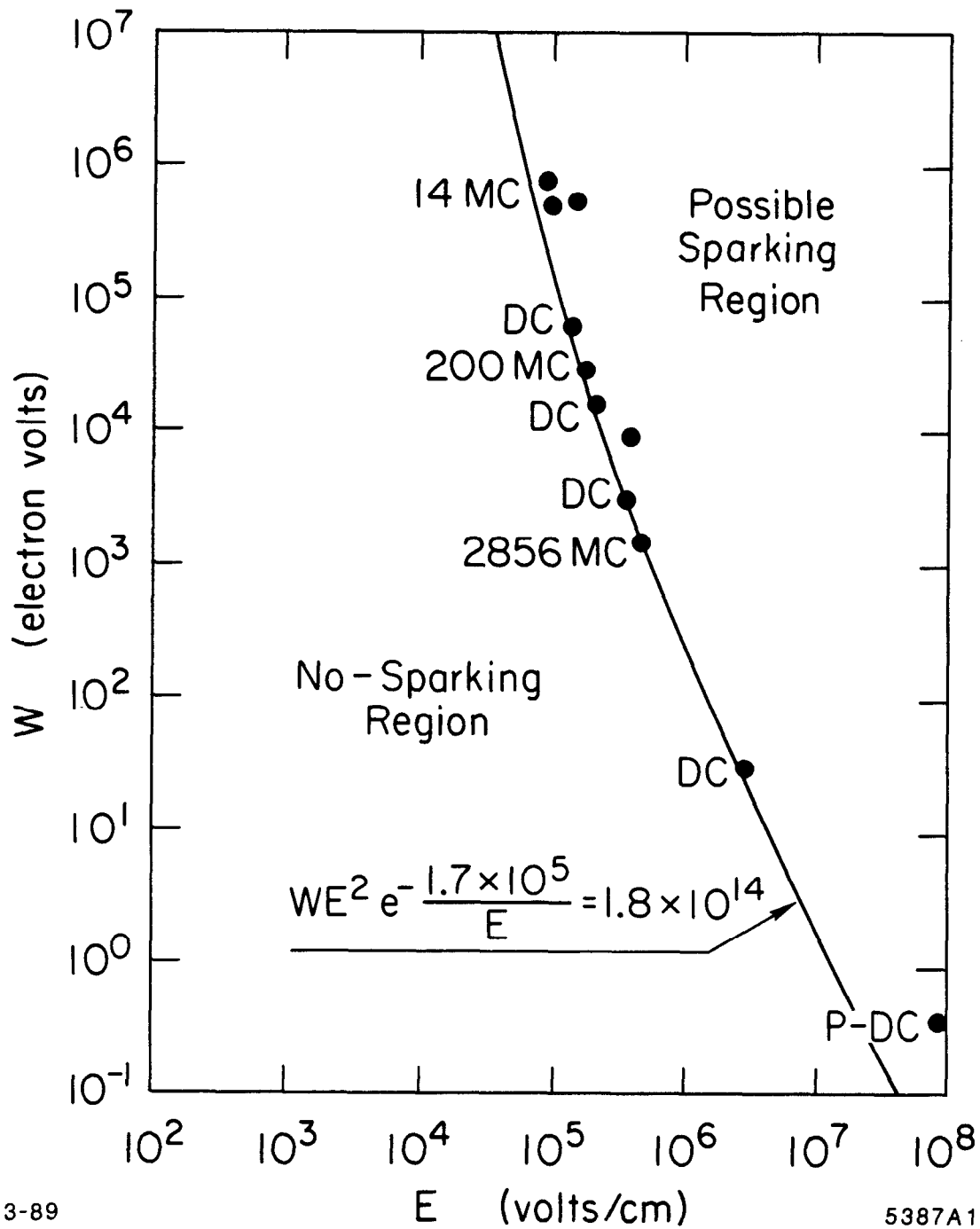


Fig. 5.28. W plotted against E , the cathode gradient. For DC, W corresponds to the applied voltage; for RF, W is a function of frequency and gap (From Kilpatrick [Ref. 7]).

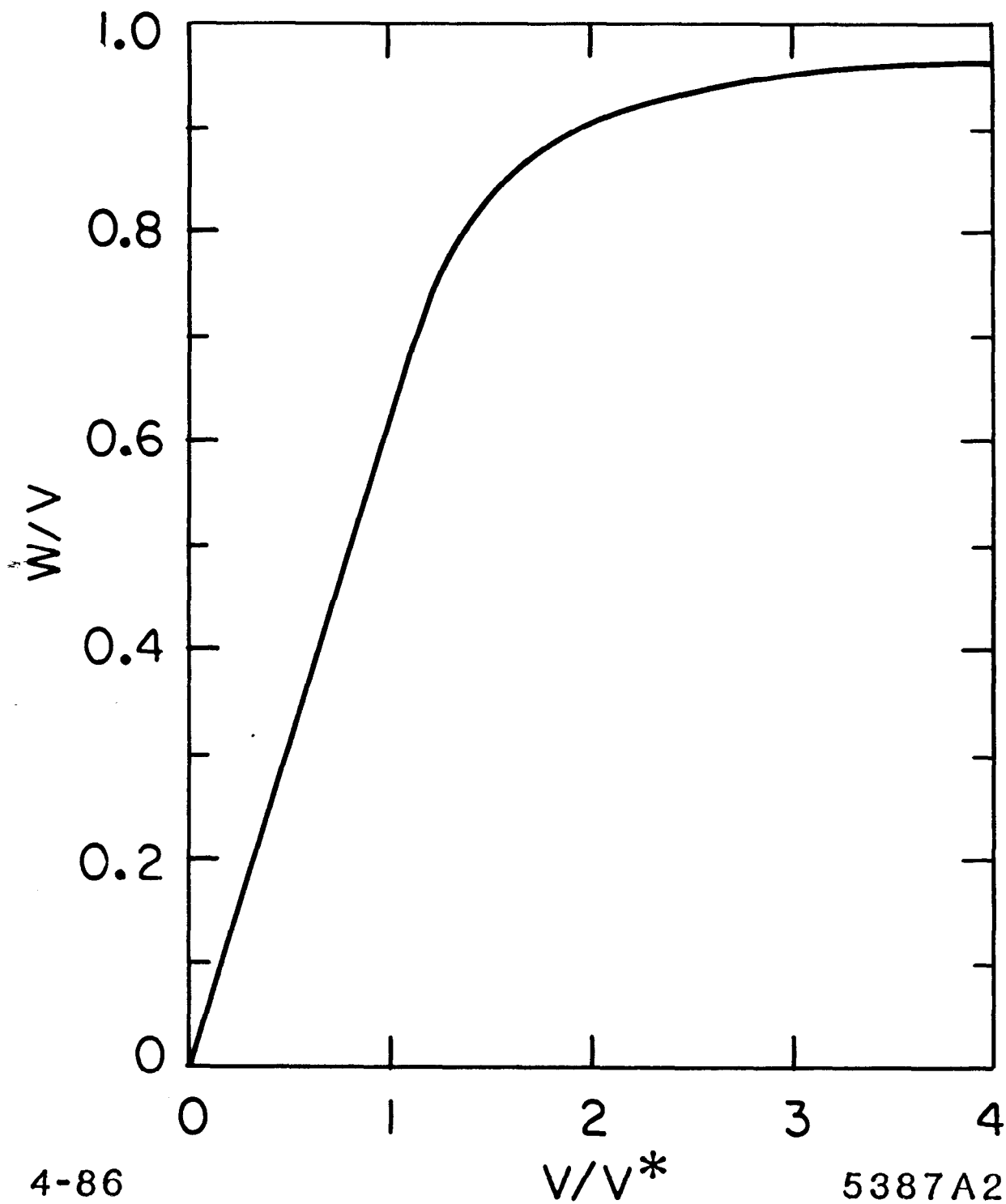


Fig. 5.29. Graph for ion transit-time correction. For plane parallel fields, $V^* = (g/\lambda)^2 M_0 c^2 / \pi q$. For computing the maximum cathode ion energy, where $\nabla \cdot E$ is not ≈ 0 , the calculation of W or V^* is without reference (From Kilpatrick [Ref. 7]).

$$m_0 \frac{d^2 x}{dt^2} = qE \sin(2\pi ft + \phi) \quad (5.36)$$

for an infinitely wide gap with uniform field amplitude E and frequency f . By assuming a very wide gap, one avoids the case where ions hit the electrode before they have reached their maximum energy. By then substituting W from Eq. (5.35) into Eq. (5.33), the relation of maximum electric field E_s in MV/m and RF frequency f in GHz can be written as

$$E_s \exp(-4.25/E_s) = 24.7 f^{1/2} \quad . \quad (5.37)$$

The interesting fact about this equation is that it predicts that the sparking threshold field E_s varies roughly as the square root of the RF frequency, which functionally agrees with our results (Eq. (5.3)). On the other hand, since 1957, many breakdown threshold experiments all over the world have largely exceeded the fields shown in Fig. 5.28 and the Kilpatrick model has been put into question. For example, the original point at 2856 MHz that was given to Kilpatrick was $E = 0.5$ MV/cm (and not 3.4 MV/cm as it is found to be now), corresponding to $W = 1.5$ keV (as opposed to 53 keV for today's 3.4 MV/cm). By definition, our points cannot lie on the same curve. Also, the Kilpatrick formula for W was based on a gap of parallel plates which is quite different from the condition inside RF cavities with rounded disks or nose cones. In his discussion, the strong field emission enhancements due to microprotrusions and dielectric inclusions were not considered. Finally, the multiplicative effect of W in Eq. (5.33) assumed that the avalanche of secondary electrons produced by ion collisions was the dominant cause of RF breakdown. With FE current densities as high as 10^8 A/cm², it is improbable that the relatively small number of ions ($\sim 10^{10}$ hydrogen atoms/cm³ in a vacuum of 10^{-6} Torr) can play a dominant role. Thus it appears that at least in the case of RF accelerators, a modified or different model must now be invoked.

5.5.2. Some Vacuum Breakdown Models

Vacuum insulation of a high voltage device can suddenly be broken and lost because of sparking or arcing on surfaces supporting high fields. We call this irreversible catastrophic phenomenon **electrical breakdown**. It can cause permanent damage on metal surfaces and may limit the reliability of further operation.

For several decades, much effort has been expended by investigators in industry, research institutes and universities in the study of the various phases of this sudden and complicated process. Most of the breakdown studies have been carried out under pulsed or DC conditions. It is commonly agreed that the prerequisite of a breakdown event is the creation of a micro-plasma near an electrode. This micro-plasma can only be developed from an ionized local metal vapour or an ionizable contaminant released from the surface by local heating.

Breakdown can occur on either the cathode or the anode. “**cathode initiated breakdown**” is generally agreed to result from heating due to Explosive Electron Emission (EEE) at a particular spot. “**anode initiated breakdown**” can occur when a locally-focussed field-emitted current delivers enough power to an anode spot. Furthermore, all metal surfaces, even when they are well cleaned and electrically conditioned, are still covered with a variety of loosely adhering debris and microparticles, some of which are due to the above localized explosions. These microparticles can be extracted and accelerated by the electric field, and cause surface damage and breakdown, the so-called “**microparticle initiated breakdown**”.

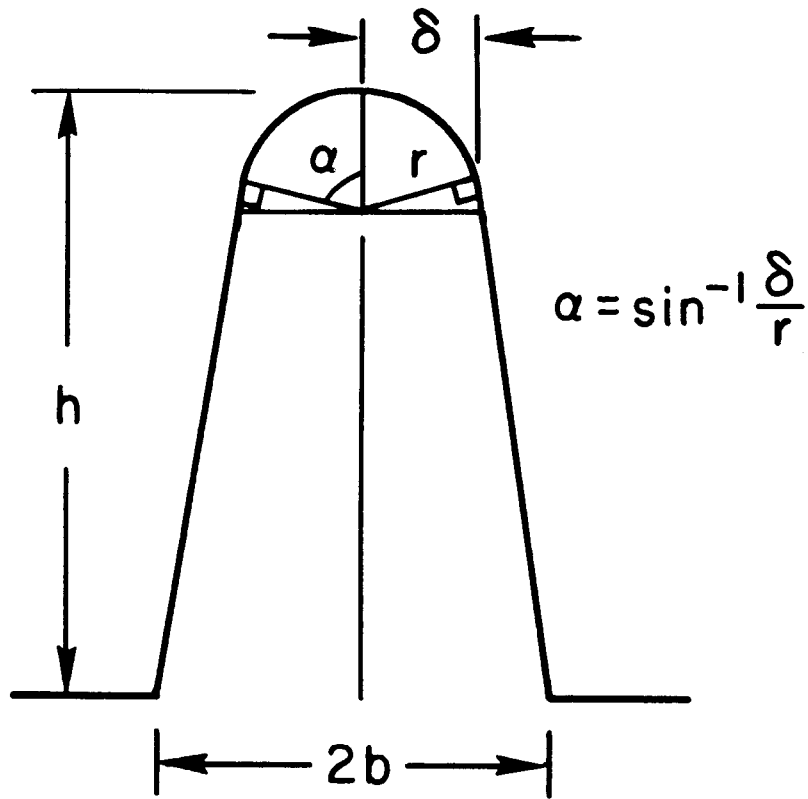
Particle accelerators, as we have seen, use high frequency resonant cavities in which the peak electric field at some location such as a nose cone, the edge of a disk, or a vane for an RFQ, may be as high as eight times the average accelerating field. The most probable breakdown event in an RF cavity is **cathode initiated breakdown** in the highest field locations where Explosive Electron Emission can occur because of a strong localized field emitted current.

Initiation of Explosive Electron Emission

When a strong field emitted current flows into the tip of an microprotrusion, several types of energy exchange take place: thermal cooling due to heat conduction from the shank of the protrusion to the “cold” reservoir provided by the bulk of the cavity body, thermal cooling due to radiation losses from the surface of the emitter, and internal heating or cooling – the so-called Nottingham effect. This effect depends on the temperature and the field strength. In order to simplify the problem, let us consider a thermally steady-state solution for a truncated cone-shape emitter, as shown in Fig. 5.30. The difference between the temperature at the top T_r and the temperature at the base T_b of the emitter can be calculated⁴⁹ as

$$\Delta T = T_r - T_b = [\rho(T)/2K\pi^2] (I_F/\alpha r)^2 + (kT I_F/K\alpha r) \cot \pi p , \quad (5.38)$$

where I_F is the total emission current, $\rho(T)$ is the electrical resistivity and K is the thermal conductivity of the emitter, k is Boltzman’s constant, p is a dimensionless temperature and field dependent parameter given by $p \approx 9.3 \times 10^5 \phi^{0.5} T/E$, which was introduced by considering a strong temperature dependence of the field emission at high temperatures. The first term in Eq. (5.38) is due to resistive heating: it increases rapidly with both emission and temperature. The second term represents the Nottingham effect: it is proportional to I_F and sensitive to T . In the case of high temperature, the average energy of the field emitted electrons are higher than that of the replacing electrons, which are supplied at the Fermi level, so that there will be a cooling effect. Conversely, in the low temperature case, the field emitted electrons are emitted from the states below the Fermi level, so that there will be a heating effect. The transition between cooling and heating is characterized by a inversion temperature T_i , which makes $p = 1/2$ for a certain field strength. When the temperature is below T_i ($\cot \pi p > 0$), the second term is positive and gives Nottingham heating. Conversely, if the temperature is above T_i ($\cot \pi p < 0$), Nottingham cooling occurs. For less refractory metal (comparing



4-86

5387A4

Fig. 5.30. An idealized field-emitting microprotrusion.

with tungsten or molybdenum) such as copper, whose melting point ($\sim 1360^\circ\text{K}$) is lower than the inversion temperature under high electric field condition (above a few MV/m), the Nottingham effect always produces extra heating effect of the emitter.

Many results of theoretical and experimental studies on the Explosive Electron Emission have been reported.^{50,51,52} When the enhanced field emission current density in an emission site exceeds 10^8 – 10^9 A/cm², localized melting of the emitter material leads to an explosion. The explosion is due to a very fast energy dissipation: the explosion follows the field emission current by about 1 nsec, which is substantially shorter than the characteristic time of heat diffusion. Thus, a melting zone is soon formed around a smaller emission center. The explosion is accompanied by transformation of the emitter material into a dense plasma, the so-called cathode-flare plasma. Fig. 5.31 shows the development of a vacuum breakdown initiated by Explosive Electron Emission. This kind of breakdown can happen even for a surface without large β microprotrusions. It can be explained by the FIHEE model, according to which the existence of dielectric films and inclusions can significantly enhance the field emission current at some local sites.

Near-Surface Dense Plasma

The concentration of the observed dense plasma near the surface is generally from 10^{25} to 10^{29} /m³,⁵³ which is very close to the density of the metal in solid state, (for example, $n_{\text{Cu}} \sim 8.42 \times 10^{28}$ /m³). The quasineutral plasma expands outwards in a spherically symmetrical manner. Its concentration decreases evenly with distance from the explosion center. The expansion velocity at the initial stage is on the order of 10^6 cm/s for most metal, (1.7×10^6 cm/s for Cu). The plasma is heated by the ohmic losses produced by the field emission current traversing it.

The development of the discharge is accompanied by light emission and the plasma expansion can be recorded by using ultra high speed photography.^{50,53} The experiments show that the plasma appears at a local point of high surface

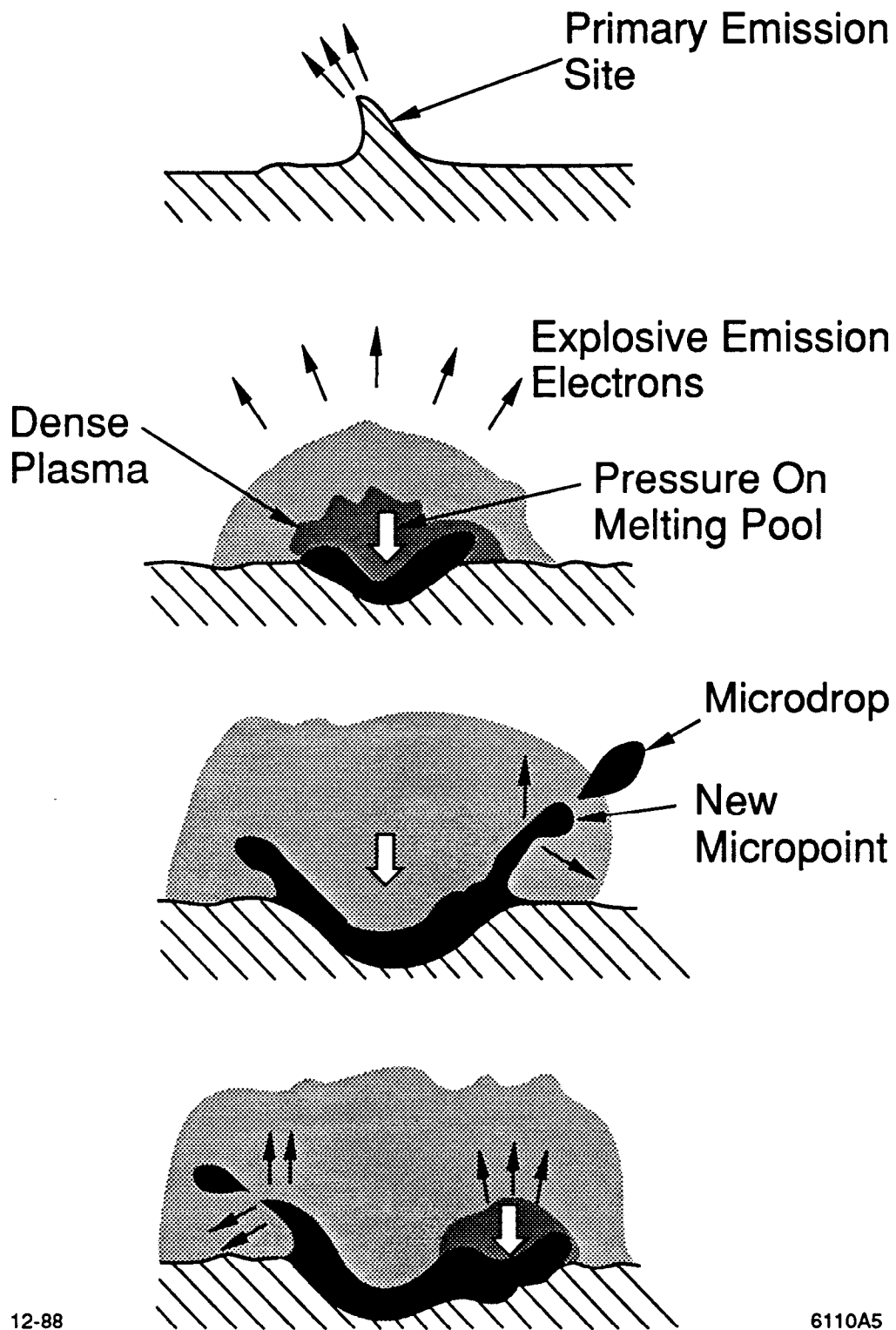


Fig. 5.31. Development of surface erosion in the case of breakdown initiated by Explosive Electron Emission.

field in the initial stage of vacuum breakdown and then spreads over the surface. An intensive electron beam is synchronously recorded.

The mechanism of ejection of electrons from the plasma into the vacuum is thermal field emission. On leaving the plasma, their own space charge produces predominant effect on their motion. The 3/2 power law will be applied.

Surface Erosion and Formation of New Explosive Emission

The dense plasma produces a high pressure on the liquid molten metal pool and leads to a splash and formation of new micropoints on the crater rim. A strong electric field, which is developed between the molten metal drop and the point tip from which the drop departed, can lead to another explosion. Thus, craters usually result from successive explosions. The propagation velocity of the liquid-metal boundary with which the drops scatter, is about 10^2 m/s. The characteristic time of development of the erosion process is $\sim 10^{-8}$ seconds. In this time interval, the erosion can expand to cover a region with dimension of a micron. This process is schematically illustrated in Fig. 5.31.

5.6 OBSERVATIONS OF FIELD EMISSION RF PROCESSING AND RF BREAKDOWN

So far we have described a number of field emission and breakdown models as described in the literature. We will now attempt to summarize our own observations of field emission, RF processing and RF breakdown as we gathered them through our various tests. In the interest of succinctness and clarity, the chronological sequence described below is the result of combining the observations from several of the tests together. Most of the following discussions refer to the experiments on the S-band disk-loaded waveguide structure.

1. Let us assume that we start with a reasonably well machined, high quality copper accelerator structure. It has been cleaned by the techniques described above, and possibly vacuum baked at 200 to 250°C for more than 24 hours. Surfaces appear to be smooth.

2. The structure is pumped down to $\sim 10^{-8}$ Torr.
3. An RGA read-out exhibits a strong H line, weak C, CH, CH₂, CH₃, CH₄, HO lines, medium H₂O and N₂- CO, and weak CO₂; occasionally, also some C₂H₂ (see Fig. 5.32).
4. Pulses of gradually increasing RF power (2.5 μ sec-long) are applied to the structure, starting from about 2 MW peak. This power level corresponds to 86 MV/m peak in our seven-cavity structure or 170 MV/m in our two-cavity structure. Occasional RF breakdown is detected. Breakdown events are manifested by the following observations:
 - (a) The reflected RF pulse jitters violently and the corresponding forward pulse from the source (klystron or magnetron) becomes somewhat erratic [see Figs. 5.33(a), (b)].
 - (b) When a glass window is available, sparks are visible in high field areas, namely on disk edges, via the video monitor and recorder.
 - (c) Whatever field emission (FE) current is observed at a given power level before breakdown, the current jumps instantaneously (i.e., within a few nanoseconds, in the pulse) by a factor of 20 to 30, as viewed via current probes on a scope. When the breakdown stops, the FE current immediately returns to its prebreakdown level.

A typical breakdown event is shown in Fig. 5.34. Such an event was recorded for the seven-cavity S-band structure by using a Camac Interface System to a VAX785 computer to digitize and store eight pulses produced at the instant of breakdown. More than 80 such events were recorded.

When a typical breakdown event takes place, predominantly in cavity (A), (see Fig. 5.6), it is invariably picked up on all four probes in cavity (A), channels one, two, three and four, but does not spill over much into cavity (B), channels five and six. Arcing and gassing seem to expand throughout the cavity in all four directions. The seventh channel in Fig. 5.34 was

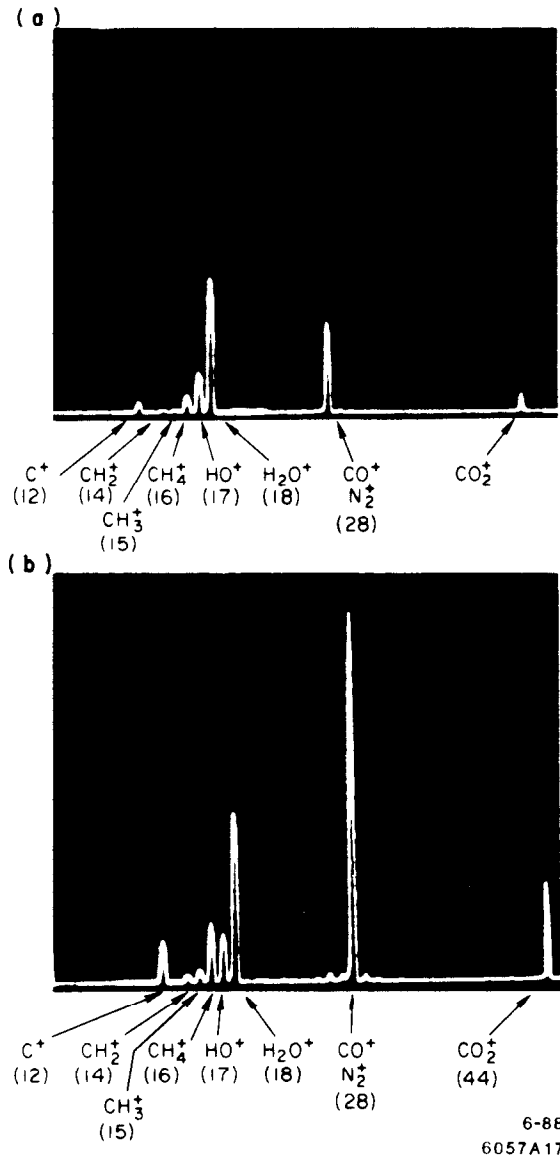


Fig. 5.32. Residual gas analyzer displays during RF processing of S-band, two-cavity structure, a) before breakdown, and b) immediately after breakdown.

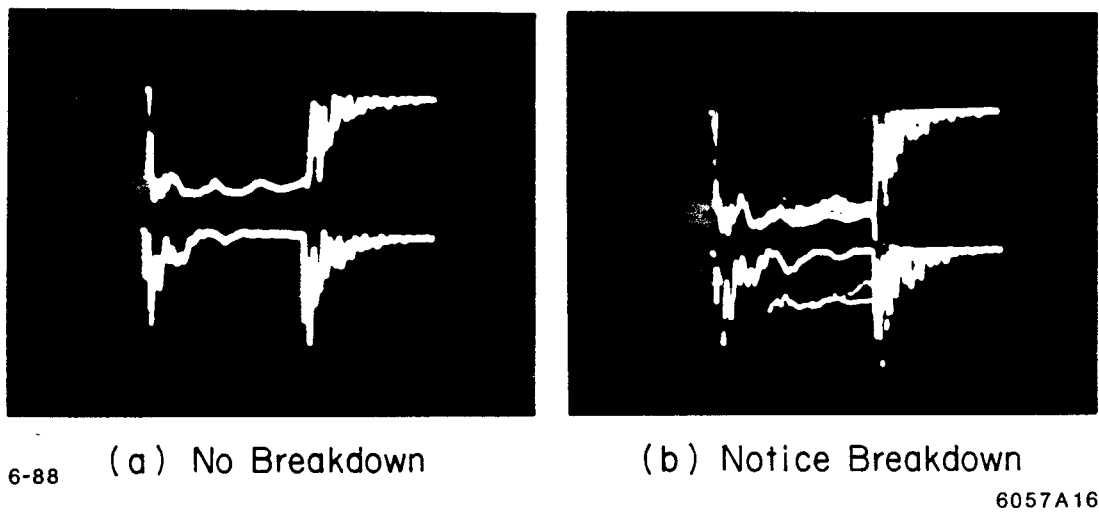


Fig. 5.33. Forward and reflected RF wave shapes: a) normal, b) during breakdown.

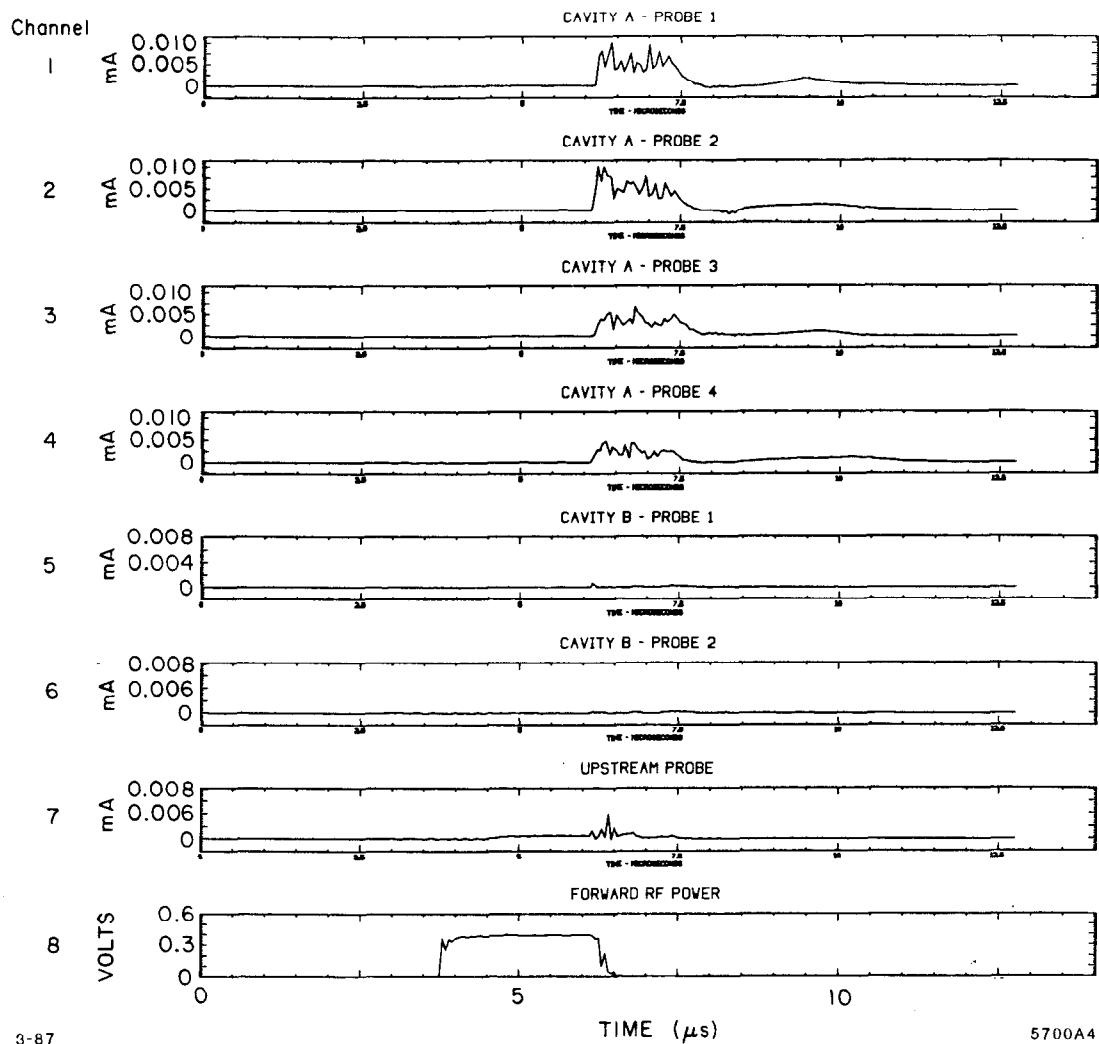


Fig. 5.34. Breakdown "event" recorded at four radial probes in full-field cavity (A), two radial probes in half-field cavity (B), and one upstream probe. The forward RF pulse provides a time reference.

connected to the probe upstream of the left-hand cut-off aperture, and the eighth channel to the forward RF pulse. The breakdown current in most recorded events appears after the first microsecond into the pulse, continues for about one microsecond after the end of the pulse while the structure is discharging, and frequently rebounds at a lower level, when the fields have practically died out. The latter phenomenon is not understood, but could be due to some form of multipactoring.

- (d) X-ray radiation bursts as observed on ion chambers alongside the structure also coincide with these pulses.
 - (e) The RGA exhibits temporary increases in all *C*-related lines [shown in Fig. 5.32(b)].
 - (f) The overall pressure increases to $\sim 10^{-7}$ Torr.
5. These events generally last for only one RF pulse ($2.5 \mu\text{s}$) or sometimes two or three consecutive pulses, unless power is raised too fast, in which case the pressure can increase to 10^{-5} Torr or higher, causing multiple breakdowns and impeding any further progress in RF processing. If the power is simply kept constant for a few minutes, the vacuum improves, *C*-related lines return to steady-state and gradual RF processing can resume.
6. Our observation is that this sequential pattern of breakdown, subsequent recovery and gradually increasing field repeats itself all the way up to the maximum field (~ 340 MV/m on the disks at S-band). With freshly constructed structures or structures processed earlier but exposed to air for several hours, this process has taken between three and fourteen hours (for a typical schedule, see Fig. 5.35). There seems to be no observable difference between the breakdown events in the range from 170 to 340 MV/m, except that the steady-state FE current increases as the field increases. Once the maximum field is reached (beyond which the cavity breaks down almost continuously), it is possible to decrease the power input and then instantaneously increase it back to its maximum value without any break-

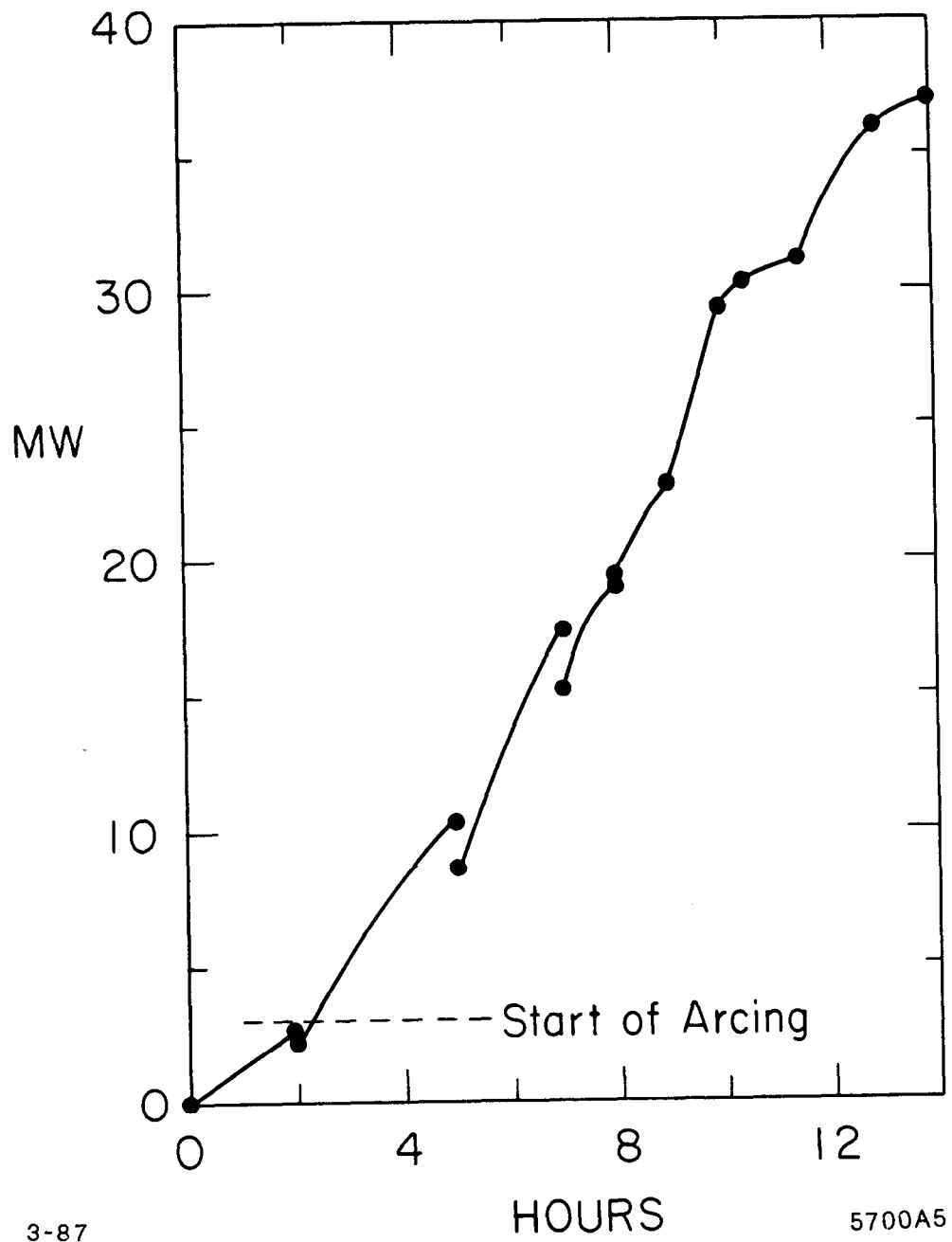


Fig. 5.35. Typical RF processing schedule for S-band, seven-cavity structure.

down. If, after this, the structure is left under good vacuum (10^{-7} to 10^{-8} Torr) for several days, the process takes only a few minutes. Under these conditions, repeatable data points for Fowler-Nordheim plots ($i_{FE}/E^{2.5}$ versus $1/E$) can be obtained. Field enhancement β -values of ~ 60 have been measured over a wide range of conditions for S-band and $\beta \sim 38$ for C-band (see Fig. 5.36).

7. After completion of the tests, the disk edges in the structure exhibit numerous pits, cracks and crater-like holes, several tens of microns in diameter (see Fig. 5.37). The longer one has operated the structure, the more pits one finds. The number of pits does not seem to affect the breakdown level, but it probably increases the steady-state FE current. It shifts the Fowler-Nordheim plots up, but it does not change their slope from their typical value of ~ 60 .
8. Controlled exposure of the evacuated cavities (10^{-7} Torr) to gasses was tried with CO and CO₂. Exposure to 50 milli-Torr of CO for three minutes, followed by pump-down, had the temporary effect of increasing i_{FE} by about 30%, but RF processing for about 15 to 30 minutes lowered it back to its pre-exposure asymptotic value. A very similar experiment carried out subsequently with CO₂ had almost no effect at all.
9. "RF scrubbing" with argon and helium was also tried. The result for argon is illustrated in Fig. 5.38. In both cases, the gas was introduced into the cavities at about 10^{-4} to 10^{-5} Torr and RF processing proceeded at moderate level (corresponding to about 100 MV/m peak field). After pumpdown, i_{FE} was found to be somewhat lower than before "scrubbing," but the value of β remained essentially unchanged, and the ultimate breakdown field did not increase. It should be noted, however, that these "RF scrubbing" experiments were done after the cavities had undergone many hours of RF processing in vacuum and the disk edges were already considerably pitted.

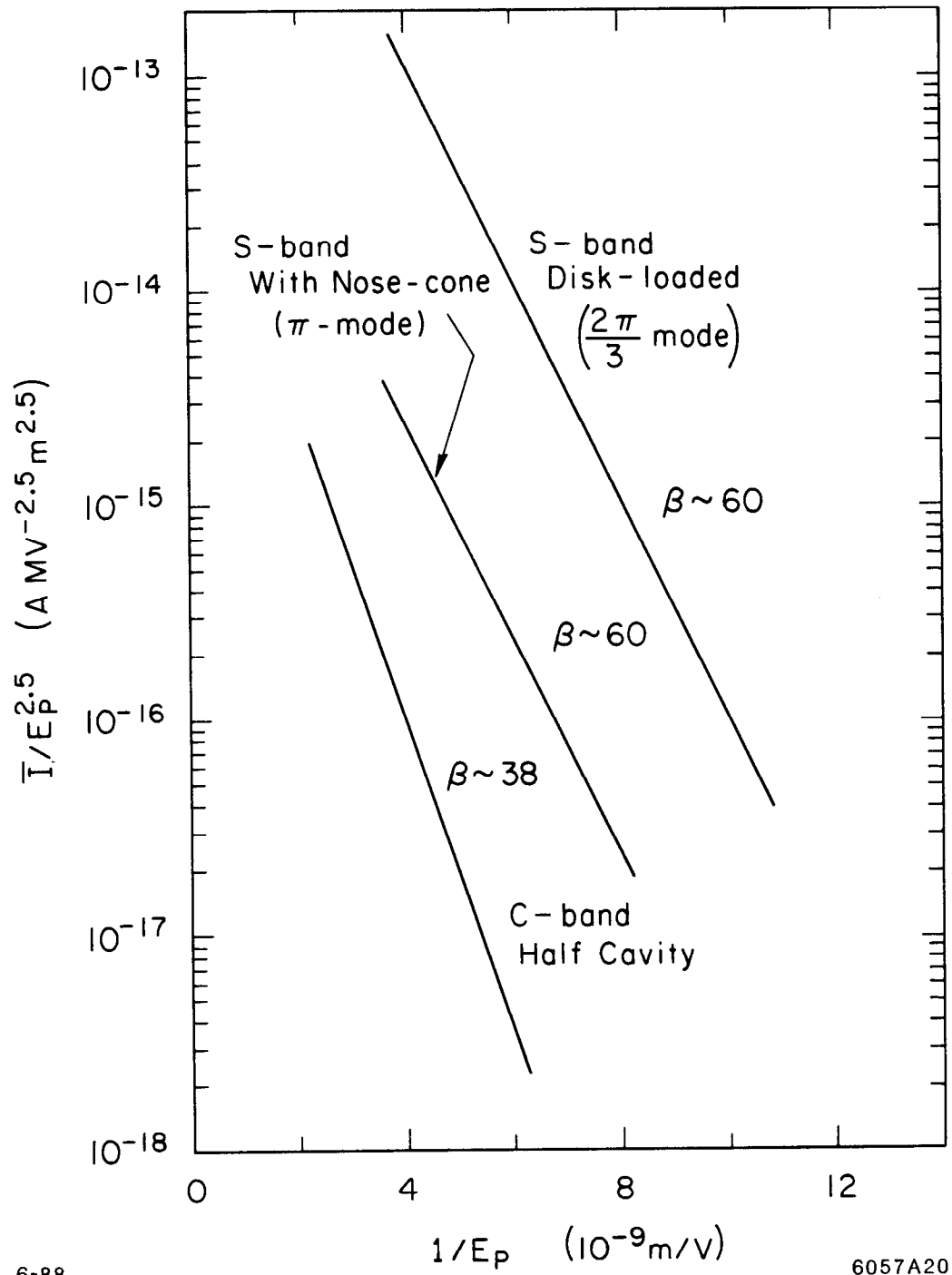


Fig. 5.36. Fowler-Nordheim plots for S-band and C-band structures.

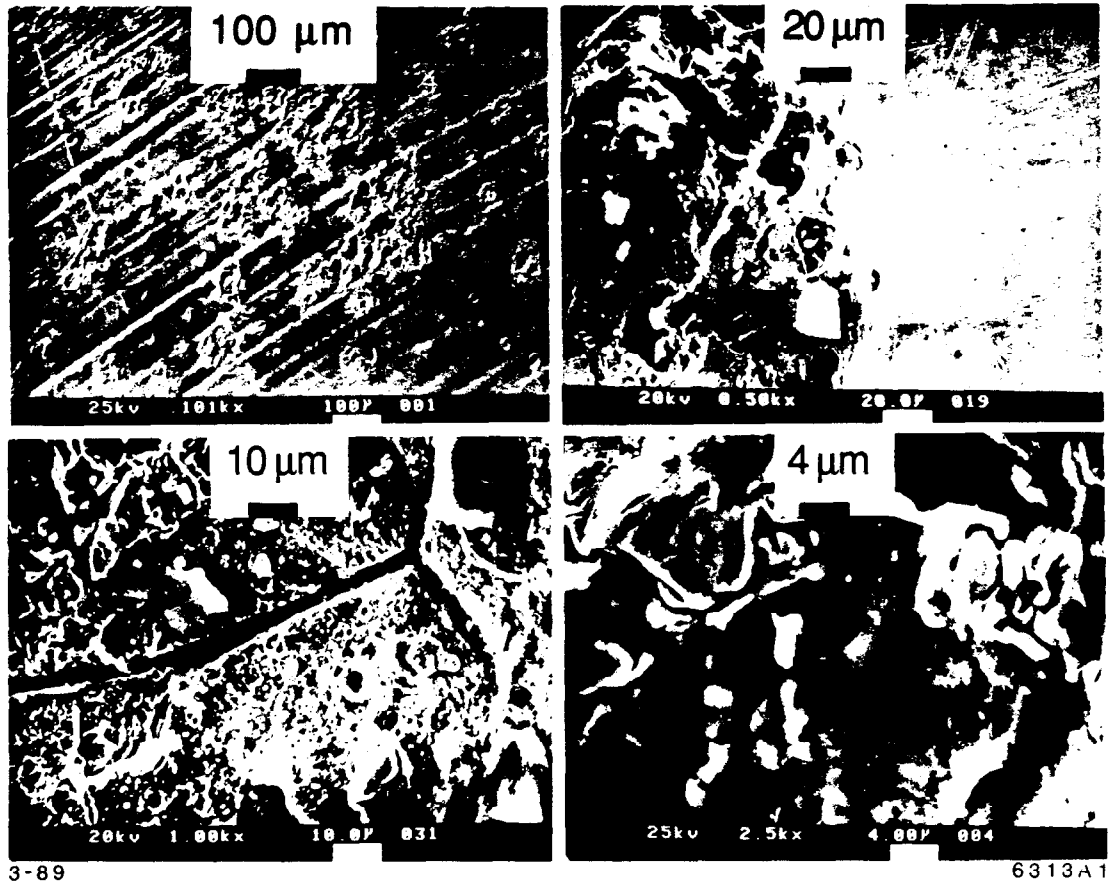


Fig. 5.37. Scanning electron microscope pictures of S-band cavity nose cone showing RF breakdown damage (note four successive degrees of magnification).

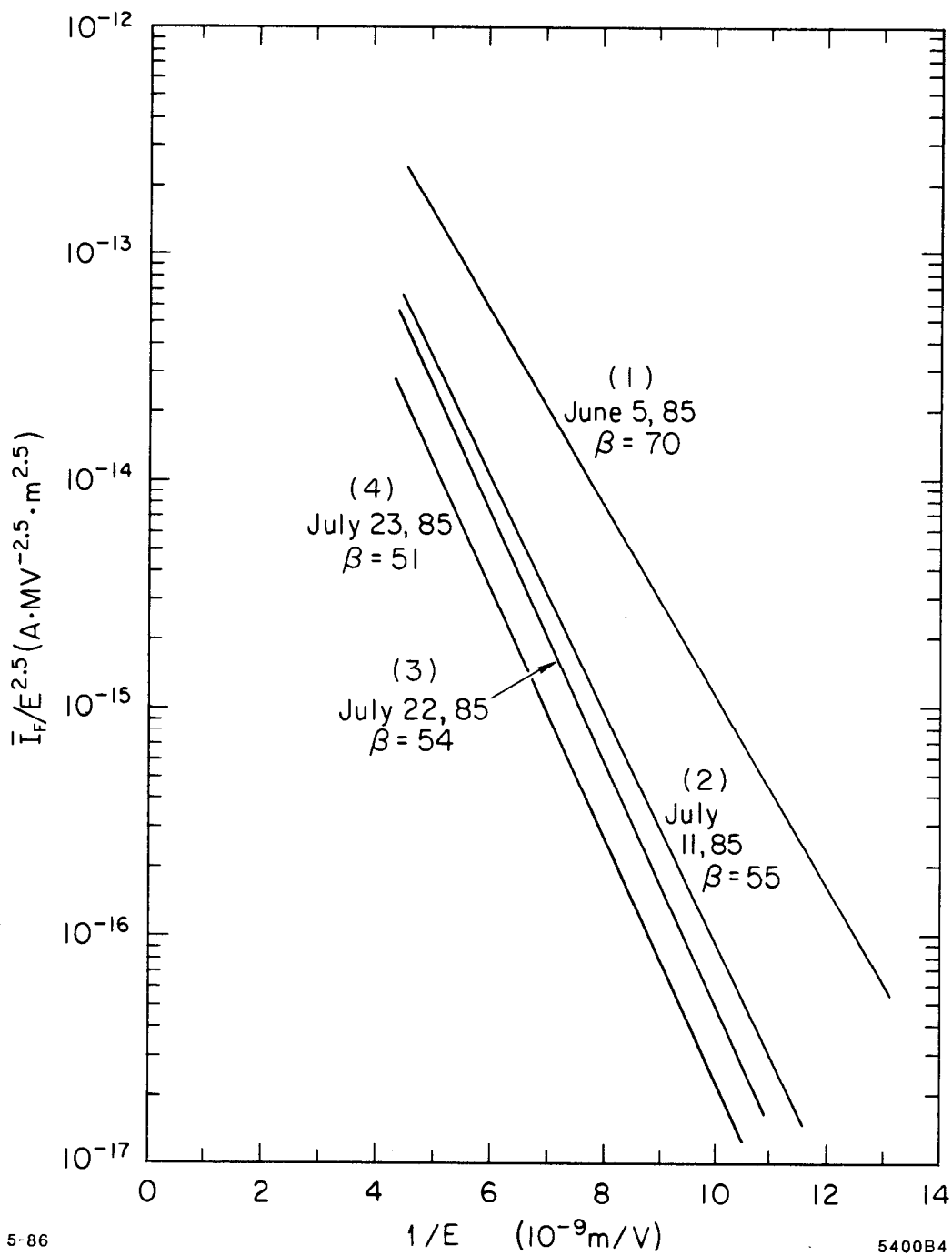


Fig. 5.38. RF Fowler-Nordheim plots for S-band (seven-cavity, $2\pi/3$ -mode) structure as a function of time. Curve (4) was recorded shortly after argon scrubbing and pumpdown.

5.7. CONFRONTATION OF RESULTS WITH EXISTING MODELS

The measurements and observations presented in preceding sections must now be examined in the light of existing models for field emission and breakdown.

As presented in Section 5.4.3, the theories for enhanced field emission are based on two basic models which, separately, probably cannot explain all the observed facts. The first theory states that the enhancement depends on surface geometry, typically sharp peaks, cracks, whiskers or microprotrusions. For the sake of simplicity, we shall call this the “**mountain**” model. In recent years, the pure “mountain” model has fallen into partial disfavor because few optical observations have revealed “peaked” enough mountains to explain the data. This observation is certainly true in our case: if we examine the size of the protrusions and craters on our damaged disks, we can explain geometric β -values (call them β_1) in the range of 5 to 8, but certainly not 40 to 60. Before the damage is done, the β_1 values are probably in the range of 2–4. Furthermore, even though we cannot get stable Fowler-Nordheim plots when we start RF processing, the effective β , call it β_{eff} , is probably greater than 40–60 at the beginning of RF processing since breakdown appears at a lower macroscopic field, say ~ 100 MV/m. Where then does this β_{eff} come from? For this we need help from the second theory. This theory, proposed by Latham,^{42,45,46} assumes surface oxides, adsorbed organic residues, dielectric inclusions on the surface or between crystal boundaries, dust, etc. For succinctness we shall call this the “**snow**” model, in analogy with layers of snow on the mountains.

According to the FIHEE (Field-Induced Hot-Electron Emission) model,⁴⁵ one can invoke Richardson-Dushman thermionic emission at the insulator-vacuum interface and write the emitted current density as:

$$j_F = K T_e^2 \exp(-e\chi/kT_e) \quad \text{A/m}^2 \quad (5.39)$$

where χ is the height of the surface potential barrier (i.e. the electron affinity of the insulator), T_e is an enhanced temperature of electrons, K is a constant

($\sim 1.2 \times 10^{-6} \text{ Am}^{-2}$), k is Boltzmann's constant and the energy of the hot electrons is measured by the kinetic energy they acquire in the dielectric layer of width Δd and of relative dielectric constant ϵ :

$$\frac{3}{2}kT_e = \frac{eE}{\epsilon} \Delta d \quad . \quad (5.40)$$

The average RF current density analogue to Eq. (5.32) is then:

$$\bar{j}_F = 2.36 \times 10^{-7} \chi^{-0.5} \left(\frac{e}{k}\right)^2 \left(\frac{\Delta d E}{\epsilon}\right)^{2.5} \exp \left\{ -\frac{3\chi\epsilon}{2\Delta d E} \right\} \text{ A/m}^2 \quad . \quad (5.41)$$

By comparison, Latham introduced a "dielectric β " which we shall call β_2 :

$$\beta_2 = 4.353 \times 10^9 \phi^{1.5} \frac{\Delta d}{\chi\epsilon} \quad . \quad (5.42)$$

Assuming $\phi = 4.65 \text{ eV}$, $\chi = 4 \text{ eV}$ and Δd measured in nanometers, we see that $\beta_2 = 10.9 \frac{\Delta d}{\epsilon}$. Now, combining the effect of "mountain and snow", we can invoke an effective β which is the product of β_1 and β_2 :

$$\beta_{eff} = \beta_1 \beta_2 = \beta_1 10.9 \frac{\Delta d}{\epsilon} \quad . \quad (5.43)$$

Thus, for example, assuming $\epsilon = 3$ and an initial $\beta_1 = 3$, to get an initial β_{eff} of roughly 200 would require a dielectric layer of $\sim 18 \text{ nm}$. After multiple breakdowns, let us assume that the surface damage seen in Fig. 5.37 explains β_1 's of magnitude 6 and that a multiplicative β_2 of magnitude 10 due to a dielectric layer gives a final $\beta_{eff} = \beta_1 \beta_2 = 60$. Using the same parameters as in Eq. (5.43), we then find that the final Δd dielectric layer on the damaged metal surface is reduced to 2.8 nm.

Although we have no direct measurements of these respective layer thicknesses, they are at least plausible. When we begin an RF processing cycle, the evidence is that the internal cavity surfaces are indeed covered with impurities and that the FE currents at a given field level are comparatively high. As electron and photon bombardment proceeds and gas desorption and pumpdown take place, FE decreases and seems to reach an asymptotic lower level.

Unfortunately, we do not have an evolutionary measurement of β during the RF process. The reason is that until a cavity has been RF processed to the point where it operates at its asymptotic field (either through successive breakdowns or through “RF scrubbing” with argon), a single-valued and accurate Fowler-Nordheim plot over a reasonable range of $1/E$ cannot be obtained. By the time the total range of fields can be scanned without breakdown, the impurities are desorbed to a substantial degree and the surface damage from multiple breakdown events is already irreversible. The measured β is then the final β .

That this scenario is approximately correct can also be concluded from our observation that after our S-band two-cavity structure was exposed to CO, the FE current was at first increased. However, as pointed out earlier, after 15 to 30 minutes of RF processing (*i.e.*, of “snow” removal) it returned to its pre-exposure level, *i.e.*, the few mono-layers were desorbed.

Now let us focus on the breakdown process. In contrast to field emission, which is a relatively steady and reproducible process, breakdown is a catastrophic phenomenon. As with many such phenomena, we seem to be able to list the general conditions which lead to it, but we are not able to predict the exact time when and exact location where it takes place.

In Section 5.5.2, we discussed some vacuum breakdown models. For the RF case, if we consider that the power dissipation is caused by an average field emitted current instead of a DC current and the characteristic times for a breakdown event are much shorter than the pulse length, the earlier discussions of DC breakdown can be extended to the RF case.

To be more specific, let us consider that the local microscopic field ($\beta_{eff}E_s$) at a site reaches 8-10 GV/m. In this range, the FE current density is on the order of 10^{12} - 10^{13} A/m². The heat dissipation per m^3 through ohmic loss from such a current in a medium of resistivity ρ is then $\bar{j}^2\rho$. If we assume to first

order that this heat does not have the time to be conducted away, it will raise the temperature of the volume by $\Delta T(^{\circ}\text{C})$ in a time

$$\Delta t = \frac{4.18 \times 10^6 MC \Delta T}{\bar{j}^2 \rho} \quad (5.44)$$

where M is the density in gram/cm^3 , C is the heat capacity in $\text{cal}/\text{g} \cdot \text{deg}$, and ρ is measured in $\text{ohms} \cdot \text{m}$. As it turns out, the time to reach the melting point of the metal does not depend very much on which metal is considered (in agreement with the results of Ref. 26.) and is roughly equal to:

$$\Delta t = \frac{2 \times 10^9}{\bar{j}^2} \text{ seconds} \quad (5.45)$$

Thus, for $\bar{j} = 10^{13} \text{ A}/\text{m}^2$, $\Delta t \sim 2 \text{ nsec}$. This result is consistent with our observations (Fig. 5.33) and that of other reports that breakdown, on the microsecond scale, is essentially instantaneous. In our case, *i.e.* pulsed RF, all subsequent observations as we reported them above are consistent with the model, *i.e.* we witness:

- a large current jump (by a factor of 20-30) due to the ionization of the plasma and the release of electrons,
- emission of light (the cathode flare or spark reported by others),
- a sudden power reflection from the structure (due to the consumption of a significant fraction of the few joules stored in the cavity and the collapse of the fields),
- a sudden rise in carbon-related molecules in the RGA (the evaporated copper is too heavy to reach the RGA and is locally reabsorbed by the cold walls of the cavity),
- that the cavity disks, upon subsequent examination, are damaged.

5.8. CONCLUSIONS AND REMAINING PROBLEMS

Having convinced ourselves that our scenario of “snow-covered mountains” sometimes subject to “volcanic eruptions” is a rather plausible one, let us now draw our conclusions and list some remaining questions and problems.

1. In our S-band structures, breakdown first appeared at ~ 86 MV/m in the seven-cavity section and at ~ 170 MV/m in the somewhat cleaner two-cavity structure. Both were processed up to over 300 MV/m peak field. We believe that the early breakdown events happened predominantly due to “snow” and that the surface was damaged after explosive electron emission. We did not examine the inside of the cavities until we reached the top field. By that time, there were plenty of “mountains” and “craters” formed.
2. Close to the top field, immediately after a breakdown event, the FE current generally returns exactly to its pre-breakdown level. What does this mean? Why doesn't the modification of the one local mountain with its local snow change the FE current? Probably because by this time, there are many similar sites which produce numerous other secondary emitted electrons and swamp the effect of the local change.
3. We observed throughout our experiments that the FE current was independent of the pressure in the cavity, a fact which is consistent with the above model. The probability of breakdown occurrence was also quite pressure-independent in the 10^{-8} to 10^{-6} Torr range. When the pressure at the pumps approaches 10^{-5} Torr, the frequency of breakdown does increase and the measurements become somewhat unstable. It must be stated that the exact pressure in our cavities subject to breakdown is not known because the pumps (see Fig. 5.6) are about a meter or so away, and local puffs of gas (“clouds” over the mountains) cannot be measured accurately: they can only be inferred. Thus it is possible that at these higher pressures the breakdown threshold is affected by ion formation (à la Kilpatrick!) with extra surface bombardment, sudden space charge neutralization which raises

the local field, or even a more complex phenomenon. Thus to carry our geophysical analogy one step further, it may be that the volcanic eruption of a snow-covered mountain is precipitated by the cloud floating above it.

4. Another question that remains unanswered is the frequency dependence of Eq. (5.3). On the one hand, it more or less agrees with the Kilpatrick criterion of Eq. (5.37) even though the scale is off by a factor of 8. On the other hand, the principal mechanism behind EEE does not seem to require the hydrogen ions which are involved in the derivation of this criterion. Thus, the resemblance between the two formulas may be purely fortuitous, unless the ultimate breakdown “trigger” before EEE takes place is somehow related to the ion energy which scales as $(eE)^2/m_0f^2$. Note however, as we just pointed out, that in our experiments the probability of breakdown events was quite pressure-independent in the 10^{-8} to 10^{-6} Torr range. A second possibility is that the probability of breakdown is related to the energy stored per unit length, which scales as E^2/f^2 . However, this argument also appears to be flawed because the energy required to melt a surface irregularity on the order of $(1-10 \mu\text{m})^3$ is an extremely small fraction of the few joules stored in each cavity. A third possibility is the model proposed by Halbritter⁴⁷ mentioned in Section 5.4.3 of this thesis, which indicates that the “dielectric β (our β_2 above) may be decreasing as a function of frequency. This theory, however, is still speculative and requires further confirmation.
5. Neither our model nor our observations seem to say anything about the breakdown dependence on pulse length. The S-band measurements shown in Table 5.2 and ranging between 1.5 and 2.5 μs pulse length showed only a small (<5%) decrease in breakdown field for the longer (2.5 μs) pulses. What happens at much shorter pulses, say 50 ns, which are contemplated for the next generation of linear colliders? If the breakdown due to EEE can occur in one nanosecond or less, why should some workers in the field

give breakdown field dependences scaling as perhaps t^{-1} or $t^{-1/3}$? We are not sure. More work is needed to elucidate these interesting questions.

6. Finally, we have to ask ourselves if there is some way of suppressing or at least controlling the field emission and the breakdown in an actual extremely high-gradient accelerator. The field emission is detrimental because it can absorb a substantial fraction of the RF energy, cause wakefields and x-ray radiation, and, if captured over a long accelerator length, be hard to separate from the real beam. The breakdown is detrimental for obvious reasons: it interrupts the operation of the machine, it damages the structure, and through the formation of surface defects, it increases or at least creates a high level of asymptotic field emission.

Since surface contamination of one sort or another during the manufacturing process is probably inevitable, RF processing will undoubtedly be needed to clean up the internal surfaces of the accelerator. The question then is: can this be done without damage to the surface, thereby ending up with a β of ~ 10 rather than 60? The answer is that it may be possible to avoid surface damage by starting the RF processing at a low-field level with argon or helium, or treatment with another gas such as atomic oxygen. The reduction of the ultimate microscopic field would not only give us an extra margin of safety, particularly for future structures⁵ with higher peak-to-average fields, but it would also reduce field emission at the operating level, an important feature to reduce detrimental dark currents which can cause transverse wakefields and absorb RF energy.

A series of new experiments are being planned at SLAC with a novel damped wakefield structure and a demountable cavity to pursue the above research.

References

1. G. A. Loew and R. B. Neal, "Accelerating Structures." from Part B of "Linear Accelerators," Edited by P. M. Lapostolle and A. L. Septier, North-Holland Publishing Company, Amsterdam, 1970.
2. J. W. Wang, G. A. Loew, J. Weaver, P. B. Wilson, "Microwave Measurements of Energy Lost to Longitudinal Modes by Single Electron Bunches Traversing Periodic Structures," Presented to the 1981 Linear Accelerator Conf., Santa Fe, New Mexico, Oct. 1981, SLAC-PUB-2830.
3. G. A. Loew, J. W. Wang, "Minimizing the Energy Spread Within a Single Bunch by Shaping Its Charge Distribution," IEEE Trans. on Nucl. Sci., Vol. NS-32, No. 5, Oct. 1985, SLAC-PUB-3598.
4. V. E. Balakin, A. V. Novokhatskii, V. P. Smirnov, "VLEPP: Transverse Beam Dynamics," Proceedings of the 12th Int. Conf. on High Energy Accelerators, Fermilab, 1983.
5. H. Deruyter, H. A. Hoag, A. V. Lisin, G. A. Loew, R. B. Palmer, J. M. Paterson, C. E. Rago and J. W. Wang, "Damped Accelerator Structures for Future Linear e^\pm Colliders," Presented to the Particle Accelerator Conference, Chicago, Illinois, March 20-23, 1989, SLAC-PUB-4865.
6. G. A. Loew and J. W. Wang, "RF Breakdown Studies in Room Temperature Electron Linac Structures," Presented to the XIIIth International Symposium on Discharges and Electrical Insulation in Vacuum, Paris, France, June, 1988, SLAC-PUB-4647.
7. W. D. Kilpatrick, "Criterion for Vacuum Sparking Designed to Include Both RF and DC," Rev. of Sci. Instrum. , Vol. 28, No. 10, 1957.
8. R. F. Koontz, G. A. Loew, R. H. Miller and P. B. Wilson, "Single Bunch Beam Loading on the SLAC Three-Kilometer Accelerator," IEEE Trans. on Nucl. Sci., Vol. NS-24, No. 3, March 1977, SLAC-PUB-1917.

9. J. E. Clendenin, *et al.*, "Beam Parameter Measurements for the SLAC Linear Collider," Proc. of the 1981 Linear Accelerator Conference, Santa Fe, New Mexico, Oct. 19-23, 1981, SLAC-PUB-2828.
10. P. B. Wilson, J. B. Styles and K.L.F. Bane, "Comparison of Measurement and Computed Loss to Parasitic Modes in Cylindrical Cavities with Beam Port," IEEE Trans. on Nucl. Sci., Vol. NS-24, No. 3, June 1977, SLAC-PUB-1908, March 1977.
11. J. N. Weaver, "Measuring, Calculating and Estimating PEP's Parasitic Mode Loss Parameters," SLAC PEP-Note-342 (January 1981, unpublished).
12. M. Sands, Private communication.
13. P. B. Wilson, "Transient Beam Loading in Electron-Positron Storage Rings," SLAC PEP-Note 276 (1978, unpublished).
14. P. B. Wilson, "High Energy Electron Linacs: Applications to Storage Ring RF systems and Linear Colliders," Lecture given in the 1981 Summer School on High Energy Particle Accelerators, Fermilab, July 1981, SLAC-PUB-2884.
15. M. Sands, J. Rees, "A Bench Measurement of the Energy Loss of a Stored Beam to a Cavity," SLAC PEP-Note-95, (August 1974, unpublished).
16. P. B. Wilson, "Prospects For Very High Gradient Linac-Colliders," IEEE Trans. on Nucl. Sci. Vol. NS-28, No. 3, June 1981, SLAC-PUB-2689.
17. G. A. Loew, Private communication.
18. "SLAC Linear Collider, Conceptual Design Report," SLAC-Report-229, June 1980.
19. E. Keil, "Diffraction Radiation of Charged Rings Moving in a Corrugated Cylindrical Pipe," Nucl. Instrum. Methods 100, 1972.
20. "Handbook of Applicable Mathematics," Vol. III. Numerical Methods. John Wiley & Sons (1982).

21. R. Ruth, "Multi-bunch Energy Compensation," SLAC-PUB-4541, Presented at the ICFA/INFN Workshop on Physics of Linear Collider, Capri, Italy, June 1988.
22. J. W. Wang and G. A. Loew, "Measurements of Ultimate Accelerating Gradients in the SLAC Disk-loaded Structure," presented at the 1985 Particle Accelerator Conference, Vancouver, B.C., May 1985, SLAC-PUB-3597, March 1985.
23. J. W. Wang, V. Nguyen-Tuong and G. A. Loew, "RF Breakdown Studies in a SLAC Disk-loaded Structure," Proceedings of the 1986 Linear Accelerator Conference, Stanford, CA, June 1986, SLAC-PUB-3940, April 1986.
24. J. W. Wang and G. A. Loew, "Progress Report on New RF Breakdown Studies in an S-band Structure at SLAC," presented at the 1987 Particle Accelerator Conference, Washington, D.C., March 1987, SLAC-PUB-4247, February 1987.
25. E. Tanabe, J. W. Wang and G. A. Loew, "Voltage Breakdown at X-band and C-band Frequencies," Proceedings of the 1986 Linear Accelerator Conference, Stanford, CA, June 1986.
26. E. Tanabe, "Breakdown in High-Gradient Accelerator Cavities," Proceedings of the 1984 Linear Accelerator Conference, Seeheim/Darmstadt, West Germany, p. 403, May 1984.
27. M. A. Allen, *et al.*, "Relativistic Klystron Research for High Gradient Accelerators," presented at the European Particle Accelerator Conference, Rome, Italy, June 1988, SLAC-PUB-4650, June 1988.
28. G. A. Loew, "Considerations of RF Frequency and Power Generation in Linear Colliders Using 'Conventional' Technology," SLAC-AAS-22, October 1986.

29. G. A. Loew, R. H. Miller, R. A. Early and K. L. Bane, "Computer Calculations of Traveling-Wave Periodic Structure Properties," IEEE Trans. Nucl. Sci., NS-26, p. 3701, 1979, SLAC-PUB-2295.
30. E. Westbrook, "Microwave Impedance Matching of Feed Waveguides to The Disk-loaded Accelerator Structure Operating in The $2\pi/3$ Mode," SLAC-TN-63-103, December 1963.
31. Z. D. Farkas, Private Communication.
32. R. L. Ford, W. R. Nelson, "The EGS Code System: Computer Programs for the Monte Carlo Simulation of Electromagnetic Cascade Showers (Version 3)," SLAC-Report-210, June 1978.
33. Calculations carried out by Dr. Renzo Parodi, INFN, Genoa, Italy, in collaboration with this program.
34. K. Bane, M. Sands, "Wake Fields of Very Short Bunches in An Accelerating Cavity," SLAC-PUB-4441, November 1987.
35. R. H. Fowler and L. Nordheim, Proc. Roy. Soc. A119, 173-81, 1928.
36. R. H. Good and E. W. Müller, In "Handbuch der Physik" Springer Verlag, Berlin, 21, 176-231, 1956.
37. R. V. Latham, "High Voltage Vacuum Insulation: The Physical Basis," Academic Press, 1981.
38. H. E. Tomasche and D. Alpert, "Field Emission from a Multiplicity of Emitters on a Broad-Area Cathode," J. Appl. Phys. 38, 881, 1967.
39. G. A. Farrall, "Numerical Analysis of Field Emission and Thermally Enhanced Emission from Broad-Area Electrode in Vacuum," J. Appl. Phys. 41, 563 1970.

40. F. Rohrbach, "CERN 71-28," October 1971.
41. R. J. Noer, "Electron Field Emission from Broad-Area Electrodes," *Appl. Phys.* 35, A 28 (1982).
42. R. V. Latham, "Prebreakdown Electron Emission Processes," *Proceedings XIIth Int. Symp. on Discharges and Electrical Insulation in Vacuum* (1986), pp. 14-21.
43. R. E. Hurley and P. J. Dooley, "Electroluminescence Produced by High Electric Field at the Surface of Copper Cathode," *J. Phys. D: Appl. Phys.*, Vol. 10, 1977.
44. B. M. Cox, "The Nature of Field Emission Sites," *J. Phys. D: Appl. Phys.*, Vol. 8, 1975.
45. R. V. Latham, "Prebreakdown Electron Emission," *IEEE Trans. Elec. Insul.*, Vol. EI-18 No. 3, June 1983, pp. 194-203.
46. K. H. Bayliss, R. V. Latham, "An Analysis of Field-induced Hot-Electron Emission From Metal-insulator Microstructures on Broad-area High-voltage Electrodes," *Proc. R. Soc. Lond. AA* 403, 285-311, 1986.
47. J. Halbritter, "Dynamical Enhanced Electron Emission and Discharges at Contaminated Surfaces," *Appl. Phys. A* 39, 46-57 1986.
48. H. Schopper, H. Strube and L. Szecsi: "An Investigation of Field Emission in Superconducting RF Cavities by Dose Rate Measurements," *KFK-Extern*, 3/68-6.
49. L. W. Swanson, L. C. Crouser and F. M. Charbonnier, "Energy Exchanges Attending Field Electron Emission," *Phys. Rev.* Vol. 151, No. 1, 327, 1966.
50. G. A. Mesyats, "Explosive Processes on the Cathode in a Vacuum Discharge," *IEEE Trans. Elec. Insul.*, Vol. EI-18 No. 3, June 1983, pp. 218-225.

51. E. A. Litvinov, "Theory of Explosive Electron Emission," IEEE Trans. Elec. Insul., Vol. EI-20 No. 4, August 1985, pp. 683-689.
52. G. N. Fursey, "Field Emission and Vacuum Breakdown," IEEE Trans. Elec. Insul., Vol. EI-20 No. 4, August 1985, pp. 659-670.
53. J. D. Cross, B. Mazurek, K. D. Srivastava, "Photographic Observation of Breakdown Mechanism in Vacuum," IEEE Trans. Elec. Insul., Vol. EI-18 No. 3, June 10 1983, pp. 230-233.